

Identifying and Interpreting Stratification in  
Sedimentary Rocks on Mars: Insight from Rover  
and Orbital Observations and Terrestrial Field  
Analogues

Thesis by  
Lauren A. Edgar

In Partial Fulfillment of the Requirements for the Degree  
of  
Doctor of Philosophy



CALIFORNIA INSTITUTE OF TECHNOLOGY

Pasadena, California

2013

(Defended June 29, 2012)



## ACKNOWLEDGEMENTS

First and foremost, I would like to thank my advisor, John Grotzinger, for his intellectual guidance, mentoring, and encouragement. I am grateful for all of the opportunities and advice that he has provided, as well as the many fun and rewarding experiences that we have shared.

I was very fortunate to get involved with the Mars Exploration Rover (MER) science and engineering teams, without whom this work would not be possible. I am also grateful for funding support from MER, and from NASA Headquarters under the NASA Earth and Space Science Fellowship Program – Grant NNX11AP50H.

I would like to thank the members of my thesis advisory committee – Mike Lamb, Joann Stock and Joe Kirschvink – for their helpful insight and guidance through this process, and for bringing me down to Earth through some wonderful terrestrial field experiences.

I am grateful for the research suggestions and support from the Grotzinger lab group over the years. In particular I would like to acknowledge Joannah Metz, Maggie Osburn, Katie Stack, Kristin Bergmann, and Jennifer Griffes. I am also thankful for all of the support from the GPS division, including Janice Grancich, Marcia Hudson, Dian Buchness, and Terry Gennaro.

The work presented in this thesis has benefited from collaborations with numerous co-authors. I would like to thank Alex Hayes, Dave Rubin, Steve Squyres, Jim Bell, and Ken Herkenhoff for their contributions to chapter 2. Jim Bell and Joel Hurowitz were very

helpful in the analysis of multispectral and compositional data for chapter 3, and I really appreciate the insight from John Southard, Michael Lamb and Ryan Ewing in chapter 4. I am grateful for the opportunity that I had to work with several individuals at Total S.A., and their help in making the fifth chapter of this thesis possible. Thank you to Naamen Keskes, Erwann Houzay, Sebastien Guillon, and the Sismage team in Pau, France.

Finally, I would like to acknowledge the love, support, and guidance from all of my friends and family. In particular, I am grateful for June Wicks, Alex Lockwood, Ryan Petterson, and my family. Thank you for your friendship, mentorship, and constant support.

## ABSTRACT

Sedimentary rocks on Mars provide insight into past aqueous and atmospheric processes, climate regimes, and potential habitability. The stratigraphic architecture of sedimentary rocks on Mars is similar to that of Earth, indicating that the processes that govern deposition and erosion on Mars can be reasonably inferred through reference to analogous terrestrial systems. This dissertation aims to understand Martian surface processes through the use of (1) ground-based observations from the Mars Exploration Rovers, (2) orbital data from the High Resolution Imaging Science Experiment onboard the Mars Reconnaissance Orbiter, and (3) the use of terrestrial field analogs to understand bedforms and sediment transport on Mars. Chapters 1 and 2 trace the history of aqueous activity at Meridiani Planum, through the reconstruction of eolian bedforms at Victoria crater, and the identification of a potential mudstone facies at Santa Maria crater. Chapter 3 uses Terrestrial Laser Scanning to study cross-bedding in pyroclastic surge deposits on Earth in order to understand sediment transport in these events and to establish criteria for their identification on Mars. The final chapter analyzes stratal geometries in the Martian North Polar Layered Deposits using tools for sequence stratigraphic analysis, to better constrain past surface processes and past climate conditions on Mars.

## TABLE OF CONTENTS

Acknowledgements .....	iii
Abstract.....	v
Table of Contents .....	vi
List of Illustrations .....	viii
List of Tables.....	x
Nomenclature .....	xi
1.0 Introduction .....	1
1.1 The Exploration of Sedimentary Rocks on Mars .....	1
1.2 Datasets .....	3
1.2.1 Mars Global Surveyor .....	3
1.2.2 Mars Exploration Rovers.....	3
1.2.3 Mars Reconnaissance Orbiter.....	5
2.0 Stratigraphic Architecture of Bedrock Reference Section, Victoria Crater, Meridiani Planum, Mars .....	6
2.1 Introduction.....	7
2.2 Geologic Setting.....	9
2.3 Methodology .....	12
2.3.1 Instruments.....	12
2.3.2 Data Collection .....	13
2.3.3 Data Processing .....	15
2.3.4 Simulations .....	16
2.4 Duck Bay Sedimentology and Stratigraphy .....	16
2.4.1 Lyell Unit.....	16
2.4.2 Smith Unit.....	19
2.4.3 Steno Unit .....	19
2.4.4 Chemostratigraphy.....	20
2.5 Correlation to Cape Verde .....	21
2.6 Paleo-Depositional Environment.....	23
2.6.1 Deposition and Diagenesis at Duck Bay .....	24
2.7 Interpretation of Eolian Stratigraphic Architecture.....	25
2.8 Conclusions.....	32
3.0 Hypotheses for the Origin of Fine-grained Sedimentary rocks at Santa Maria Crater, Meridiani Planum .....	34
3.1 Introduction.....	35
3.2 Geologic Setting and Methods .....	36
3.3 Multispectral Observations.....	38
3.4 Textural Observations.....	39
3.5 Composition .....	43

3.6 Diagenetic Considerations.....	44
3.7 Interpretation of Nodular Texture.....	46
3.8 Identifying and Interpreting Mudstones on Mars.....	50
3.6 Significance of Duststones and Mudstones on Mars .....	55
4.0 Low Regime Bedforms in Pyroclastic Surge Deposits, Hunt's Hole, New Mexico .....	57
4.1 Introduction.....	58
4.2 Geologic Context.....	60
4.3 Methods.....	64
4.3.1 Data Collection .....	64
4.3.2 Data Processing .....	65
4.4 Pyroclastic Facies.....	66
4.5 Analysis of Cross-stratified Facies .....	73
4.6 Flow Dynamic Reconstruction .....	80
4.7 Comparison with Other Phreatomagmatic Surge Deposits .....	84
4.8 Identification on Mars.....	86
4.9 Conclusions.....	91
5.0 Recognition and Significance of Stratal Geometries and Unconformities in Martian Layered Deposits .....	93
5.1 Introduction.....	94
5.2 Unconformities, Stratal geometries, and the Partitioning of Time in the Stratigraphic Record .....	95
5.3 Methods for Chronostratigraphic Analysis .....	98
5.4 North Polar Layered Deposits .....	102
5.5 Chronostratigraphic Analysis of the NPLD .....	104
5.6 Application to Other Regions on Mars.....	110
5.7 Implications of a Polar Layered Deposit in Galle Crater .....	114
5.8 Summary and Significance .....	116
Bibliography .....	118

## LIST OF ILLUSTRATIONS

<i>Number</i>	<i>Page</i>
2.1 Opportunity traverse to Victoria crater.....	8
2.2 Victoria crater study location.....	11
2.3 Duck Bay ingress path.....	17
2.4 Pancam and MI images of rock units.....	18
2.5 Duck Bay rose diagram.....	20
2.6 Duck Bay stratigraphic column.....	21
2.7 Cape Verde.....	22
2.8 Cabo Corrientes diagenetic band.....	25
2.9 Duck Bay and Cape Verde fence diagram.....	26
2.10 Sinuous crested bedforms.....	27
2.11 Depositional model for the stratal geometry at Cape Verde.....	29
2.12 Modern dunes in Victoria crater.....	31
3.1 Opportunity traverse to Santa Maria crater.....	37
3.2 Anomalous ejecta blocks at Santa Maria crater.....	39
3.3 Eolian stratification in the Burns formation.....	40
3.4 Ruiz Garcia.....	41
3.5 MI mosaic of Ruiz Garcia.....	42
3.6 APXS analyses of the Burns formation.....	45
3.7 Recrystallization in the Burns formation.....	46
3.8 Nodules in coarse-grained sandstone.....	48
3.9 Diagenetic modification of fine-grained carbonates.....	48
3.10 Santa Maria crater wall stratigraphy.....	49
4.1 Field study area in southern New Mexico.....	61
4.2 Representative climbing dune outcrop.....	63
4.3 Grain sampling locations.....	67
4.4 Grain size distribution.....	67
4.5 Hunt's Hole facies.....	69

4.6 Cross-bedding in LiDAR.....	70
4.7 LiDAR intensity versus grain size.....	71
4.8 Superimposed bedforms.....	74
4.9 Angles of stoss and lee side laminae .....	76
4.10 Climbing dune variability .....	78
4.11 Vertical succession in flow-parallel outcrop .....	79
4.12 Schematic block diagram.....	80
4.13 Wavelength versus wave height comparison .....	85
4.14 Potentially misinterpreted bedform geometries.....	87
5.1 Construction of a chronostratigraphic diagram .....	96
5.2 Geotime workflow .....	101
5.3 MOLA topographic map of the NPLD.....	103
5.4 NPLD stratal geometries.....	106
5.5 NPLD Geotime results.....	107
5.6 Geotime results for section parallel to inferred migration direction ..	111
5.7 Comparison of NPLD and Galle crater deposit.....	113
5.8 Galle crater geotime results .....	113

LIST OF TABLES

<i>Number</i>	<i>Page</i>
2.1 Summary of MI observations .....	14
2.2 Summary of Pancam observations .....	14
4.1 Characteristics of cross-bedded deposits .....	89
5.1 NPLD target list .....	106

## NOMENCLATURE

- APXS** Alpha Particle X-ray Spectrometer
- CTX** Context Camera
- DEM** Digital Elevation Model
- HiRISE** High Resolution Imaging Science Experiment
- IDD** Instrument Deployment Device
- LiDAR** Light Detection and Ranging
- MER** Mars Exploration Rovers
- MGS** Mars Global Surveyor
- MI** Microscopic Imager
- MOLA** Mars Orbiter Laser Altimeter
- MRO** Mars Reconnaissance Orbiter
- NPLD** North Polar Layered Deposits
- PANCAM** Panoramic Camera
- RAT** Rock Abrasion Tool
- TLS** Terrestrial Laser Scanning

*Chapter 1*

## INTRODUCTION

**1.1 The Exploration of Sedimentary Rocks on Mars**

The key question driving Mars exploration is to determine whether life ever arose elsewhere in the solar system. Since sedimentary rocks form on the surface of a planet, they contain a record of past environments, surface processes, climate regimes and, hence, potential habitability.

Mars is the only planet in our Solar System other than Earth known to have an extensive sedimentary record, and it has been the target of numerous rover, orbiter and landed missions. The study of stratified material on Mars began with Mariner 9 and Viking images (Sharp 1973; Soderblom et al. 1973; Blasius et al. 1977), and has greatly advanced with increasingly higher resolution data returned by the Mars Global Surveyor, Mars Odyssey, Mars Express, Mars Exploration Rovers, and Mars Reconnaissance Orbiter (Malin and Edgett 2000, 2003; Christensen et al. 2000; Glotch and Christensen 2005; Jaumann et al. 2007; Squyres et al. 2004a; Grotzinger et al. 2005; McEwen et al. 2010).

Data returned from these missions reveal that Mars has a diverse geologic history and that the stratigraphic architecture of sedimentary rocks on Mars is similar to that of Earth. The processes that govern sediment deposition and erosion on Mars can be reasonably inferred through reference to analogous terrestrial systems, although there are several key differences between the Martian and terrestrial sedimentary records (McLennan and Grotzinger 2008; Grotzinger and Milliken in press). Using the Earth as a guide, but

keeping an open mind to new sedimentary rock types, facies, and processes, we can begin a new era of extraterrestrial sedimentology (Grotzinger and Milliken in press).

An essential technique for interpreting sedimentary deposits on Earth and Mars is the analysis of stratal geometries and stratification. Stratification provides information regarding the depositional environment, and may reveal clues regarding paleoflow velocities and paleocurrent directions (Rubin 1987). Large-scale stratal geometries also provide insight as to the depositional environment, as well as a framework for understanding genetically related strata and changes in the stratigraphic record. These methods are useful for recognizing past surface processes involving water, wind, ice and volcanic activity, and may be used to identify potentially habitable environments.

The following chapters describe several studies of sedimentary rocks, based on distinctive characteristics of stratification and stratal geometries. Chapters 2 and 3 trace the history of aqueous activity at Meridiani Planum, using geometric relationships to reconstruct eolian bedforms at Victoria crater, and the lack of stratification in fine-grained rocks at Santa Maria crater as an indication of a new potential mudstone facies. Chapter 4 shows the use of Terrestrial Laser Scanning to study cross-bedding in pyroclastic surge deposits on Earth in order to understand sediment transport in these events and to establish criteria for their identification on Mars. The final chapter introduces a new technique for analyzing stratified rocks on Mars, using chronostratigraphic analysis to constrain past surface processes in the North Polar Layered Deposits.

## 1.2 Datasets

The work described in the following chapters was made possible by data from several spacecraft. Brief descriptions of the most heavily used datasets are provided below.

### 1.2.1 Mars Global Surveyor

The Mars Global Surveyor (MGS) was a global mapping mission operating from 1997 to 2006. Through its five scientific instruments, MGS advanced our understanding of the topography, gravity, magnetic fields, surface composition, thermal properties, and atmosphere of Mars. This thesis uses data from the Mars Orbiter Laser Altimeter (MOLA), which provided a precise global map of the surface height of Mars. MOLA transmitted laser pulses at a rate of 10 Hz, and measured the flight time to determine distance to the surface. MOLA has a vertical resolution of 1 m, a surface spot size of 168 m, and along-track shot spacing of 300 m (Smith et al. 2001). Global topographic maps were produced at resolutions up to 128 pixels per degree, and 512 pixels per degree in the polar regions.

### 1.2.2 Mars Exploration Rovers

The twin Mars Exploration Rovers (MER), *Spirit* and *Opportunity*, arrived at Mars in 2004. *Spirit* investigated Gusev crater until 2010, and *Opportunity* is continuing its exploration of Meridiani Planum. This thesis uses data primarily from *Opportunity*. Each rover contains a suite of scientific instruments including Panoramic Cameras (Pancam), Microscopic Imager (MI), Rock Abrasion Tool (RAT), Alpha Particle X-ray Spectrometer (APXS), Mossbauer Spectrometer (MB), and miniature Thermal Emission Spectrometer (mini-TES). Data from Pancam, MI, RAT and APXS are described in chapters 2 and 3.

Pancam is a multispectral imaging system, consisting of two cameras located on the rover's mast, 1.5 m above the ground. Each camera contains an eight-position filter wheel, allowing multispectral observations in the 400 to 1100 nm wavelength range (Bell et al. 2003). Stereoscopic measurements can be made using parallax between the two camera eyes, spaced 30 cm apart. Pancam has a focal length of 43 mm and a field of view of  $1024 \times 1024$  pixels ( $16^\circ \times 16^\circ$ ). Pancam is also capable of panoramic measurements, with the ability to image  $360^\circ$  in azimuth and  $\pm 90^\circ$  in elevation (Bell et al. 2003). Pancam data are used in this thesis to study the lithology, structure, distribution and spectral qualities of rocks and outcrops.

The MI is a high-resolution imaging system mounted on the rover's arm, also known as the Instrument Deployment Device (IDD). The MI has a field of view of  $1024 \times 1024$  pixels, which corresponds to a field of view of 31 mm x 31 mm at a working distance of 63 mm (Herkenhoff et al. 2003). To compensate for the variable topography of rock targets and limited depth of field, MI images are usually taken as a stack of images. The IDD moves along a path normal to the surface, and acquires images every few millimeters. In this way, the MI acts as both a microscope and a camera, producing images with a resolution of  $30 \mu\text{m}/\text{pixel}$  (Herkenhoff et al. 2003).

The RAT provides a way to expose fresh rock surfaces for chemical and textural analyses. The RAT is located on the IDD, and uses a diamond-tipped grinding wheel to remove a cylindrical area 4.5 cm in diameter and 0.5 cm deep (Gorevan et al. 2003). The RAT is often used in combination with the MI and APXS, to enhance petrologic textures and provide fresh surfaces for chemical analysis.

The APXS is also located on the IDD, and determines the chemical composition of rocks and soils by x-ray spectroscopy. The APXS exposes materials to energetic alpha particles and x-rays from radioactive curium-244 sources, and then measures the spectra of backscattered alpha particles and emitted x-rays (Gellert et al. 2006). APXS data are used in chapter 3 to understand the composition of a new facies at Meridiani Planum.

### *1.2.3 Mars Reconnaissance Orbiter*

The Mars Reconnaissance Orbiter (MRO) entered Mars orbit in 2006, and consists of several high-resolution instruments. The work described in the following chapters relies on data from the High Resolution Imaging Science Experiment (HiRISE) and Context Imager (CTX) onboard MRO.

HiRISE was designed to image the Mars surface at higher resolutions than previously possible. HiRISE is capable of acquiring images at a resolution of up to  $\sim 25$  cm/pixel (McEwen et al. 2007), resolving features down to  $\sim 1$  m in thickness. HiRISE images are approximately 6 km wide, and at least 10 km long. HiRISE is capable of making stereo topographic measurements, with vertical precision of  $\sim 25$  cm over  $\sim 1$  m<sup>2</sup> areas (McEwen et al. 2007). Context for HiRISE images is provided by CTX. CTX images have a resolution of 6 m/pixel and a swath width of 30 km (Malin et al. 2007). HiRISE and CTX images are used in chapters 2 and 3 to provide base maps and context for rover traverses, and in chapter 5 for identifying layered deposits with stratal geometries.

*Chapter 2*STRATIGRAPHIC ARCHITECTURE OF BEDROCK REFERENCE SECTION,  
VICTORIA CRATER, MERIDIANI PLANUM, MARS

Originally published in:

Edgar, L. A., J. P. Grotzinger, A. G. Hayes, D. M. Rubin, S. W. Squyres, J. F. Bell III, and K. E. Herkenhoff (2012), Stratigraphic Architecture of Bedrock Reference Section, Victoria Crater, Meridiani Planum, Mars, *Sedimentary Geology of Mars, SEPM Special Publication, 102*, 195-209.

**Abstract**

The Mars Exploration Rover *Opportunity* has investigated bedrock outcrops exposed in several craters at Meridiani Planum, Mars, in an effort to better understand the role of surface processes in its geologic history. *Opportunity* has recently completed its observations of Victoria crater, which is 750 m in diameter and exposes cliffs up to ~15 m high. The plains surrounding Victoria crater are ~10 m higher in elevation than those surrounding previously-explored Endurance crater, suggesting that Victoria crater exposes a stratigraphically higher section than Endurance crater; however Victoria strata overlap in elevation with the rocks exposed at Erebus crater. Victoria crater has a well-developed geomorphic pattern of promontories and embayments that define the crater wall, and reveal thick bedsets (3 to 7 m) of large-scale cross-bedding, interpreted as fossil eolian dunes. *Opportunity* was able to drive into the crater at Duck Bay, located on the western margin of Victoria crater. Data from the Microscopic Imager and Panoramic Camera reveal details about the structures, textures, and depositional and diagenetic events that influenced the Victoria bedrock. A lithostratigraphic subdivision of bedrock units was enabled by the

presence of a light-toned band that lines much of the upper rim of the crater. In ascending order three stratigraphic units are named Lyell, Smith and Steno; Smith is the light-toned band. In the Reference Section exposed along the ingress path at Duck Bay, Smith is interpreted to represent a zone of diagenetic recrystallization, however, its upper contact also coincides with a primary erosional surface. Elsewhere in the crater the diagenetic band cross-cuts the physical stratigraphy. Correlation with strata present at nearby promontory Cape Verde suggests that there is an erosional surface at the base of the cliff face that corresponds to the erosional contact below Steno. The erosional contact at the base of Cape Verde lies at a lower elevation, but within the same plane as the contact below Steno, which suggests that the material above the erosional contact was built on significant depositional paleotopography. The eolian dune forms exposed in Duck Bay and Cape Verde, combined with the geometry of the erosional surface, suggests that these outcrops may be part of a larger-scale dune architecture. This insight is possible only due to the larger-scale exposures at Victoria crater, which significantly exceed the more limited exposures at Erebus, Endurance, and Eagle craters.

## 2.1 Introduction

Sedimentary rocks on Mars provide insight into past aqueous and atmospheric processes, climate regimes and potential habitability. The Mars Exploration Rover *Opportunity* has investigated several impact craters in Meridiani Planum, Mars, (Figure 2.1) studying the exposed sedimentary rocks of the Burns formation<sup>1</sup> in an effort to better understand the role of aqueous activity in its geologic history. In doing so, *Opportunity*

---

<sup>1</sup> Note that the location and formation names used in this study are informal, and have not been approved by the International Astronomical Union.

discovered in situ evidence for an aqueous depositional environment at Eagle, Endurance and Erebus craters (Squyres et al. 2004b; Grotzinger et al. 2005; Squyres et al. 2006a; Grotzinger et al. 2006; Metz et al. 2009). Furthermore, these results also suggest that the stratigraphic architecture of sedimentary rocks on Mars is similar (though not identical) to Earth, suggesting that the processes that govern facies deposition and alteration on Mars can be reasonably inferred through reference to analogous terrestrial depositional systems (Grotzinger et al. 2005).

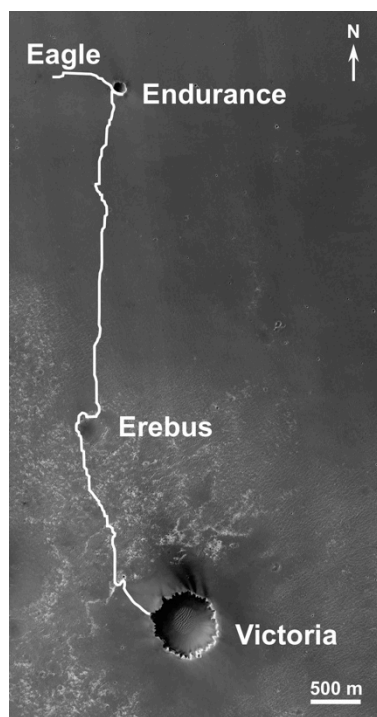


**Figure 2.1.** *Opportunity* traverse map as of sol 952 plotted on HiRISE image. Victoria crater is approximately 6 km southeast of the original *Opportunity* landing site in Eagle crater. Sunlight illuminates scene from upper left. Image credit: NASA/JPL/University of Arizona.

As the mission progressed *Opportunity* explored increasingly larger outcrops over a greater spatial scope, and it became clear that both depositional and diagenetic processes acted regionally in extent (Squyres et al. 2009). Here, diagenesis refers to any low-temperature, low-pressure alteration after deposition, which may include weathering. One important interpretation is that most primary sedimentary bedforms – a key element in the

sedimentology of the Burns formation – are not only regional in extent (found in many bedrock outcrops explored by the rover), they are also of very large magnitude. This is important because it facilitates a greater understanding of the processes controlling deposition as well as the scale of the depositional environment. The outcrop exposed at *Opportunity's* landing site in Eagle crater was only 35 cm thick (Squyres et al. 2004a). At Erebus crater, exposed outcrops were up to 5 m thick (Grotzinger et al. 2006; Metz et al. 2009) and, at Endurance crater, the rover analyzed more than 7 m of stratigraphy (Grotzinger et al. 2005). These latter localities provided evidence for meter-scale cross-stratification. In contrast, outcrops at Victoria crater provide exposures of on the order of 15 meters of true stratigraphic thickness, which permits analysis of larger scales of cross-stratification, and thus larger-scale primary bedforms can now be reconstructed.

Victoria crater lies 6 km southeast from the original *Opportunity* landing site in Eagle crater. At ~750 m in diameter (Grant et al. 2008), it is the largest crater yet explored by *Opportunity*. Victoria crater offers the opportunity to test the existing models for bedrock formation and provides new insight into larger-scale sedimentary bedforms. This study [examines the stratigraphy and eolian architecture along the ingress path at Duck Bay], using data from the Microscopic Imager and Panoramic Camera to elucidate the structures, textures, and depositional and diagenetic events that formed and modified the Victoria bedrock. Several depositional and diagenetic hypotheses are explored, and a Reference Section exposed along the ingress path at Duck Bay is interpreted in the context of the regional geologic history.

## **2.2 Geologic Setting**

Rocks exposed in the region of the *Opportunity* landing site reveal a complex sedimentary history, involving eolian sediment transport and deposition, followed by episodic inundation by shallow surface water, evaporation, exposure and desiccation (Squyres et al. 2004b; Grotzinger et al. 2005; Grotzinger et al. 2006; Metz et al. 2009). The bedrock exposed at Eagle crater, combined with that in Endurance crater, reveals a stratigraphic thickness of approximately 7 m, known as the Burns formation. The Burns formation refers to a sequence of well-sorted, moderately indurated sandstones, interpreted

to be deposited by eolian and locally subaqueous processes (Grotzinger et al. 2005; McLennan and Grotzinger, 2008). Represented by dune, sand sheet, and interdune facies, this formation records a progressive increase in the influence of groundwater and surface water during deposition (Grotzinger et al. 2005). This wetting-upward trend contrasts with the overall drying-upward trend as seen in Erebus crater, at a slightly higher stratigraphic level (Metz et al. 2009). The series of outcrops explored by *Opportunity* at Meridiani Planum may comprise a full climatic cycle, from dry to wet to dry conditions, as one moves stratigraphically upward from the strata at Eagle crater through the strata at Erebus crater (Metz et al. 2009). After completing its exploration of the outcrops at Erebus crater, *Opportunity* set out to explore Victoria crater.

Victoria crater is a degraded simple crater at Meridiani Planum (1.9483°S, 354.4742°E). Orbital images show that stratified rocks beneath the Meridiani plains lie disconformably on Middle to Late Noachian cratered terrains, indicating that the Meridiani plains might be as much as several billion years old (Arvidson et al. 2003). Topographic measurements made by the Mars Orbiter Laser Altimeter (MOLA) indicate that the plains surrounding Victoria crater are ~10 m higher in elevation than those surrounding previously explored Endurance crater, suggesting that Victoria crater exposes a stratigraphically higher section (assuming flat dip of strata). The outcrop exposed at Victoria crater may lie at the same elevation as the uppermost unit in Erebus crater, allowing for possible stratigraphic correlation between these two locations. Victoria crater has a scalloped rim produced by erosion and downhill movement of crater wall material. Most of the erosion is attributed to eolian processes, which are actively widening and filling the crater, and elongating the crater across a WNW-ESE axis (Grant et al. 2008). The scalloped rim consists of a series of alcoves and promontories around the crater, exposing more than 10 m of well-bedded sedimentary rocks.

Prior to ingress at Duck Bay, *Opportunity* spent several months traversing the rim of the crater. Observations of outcrops at several promontories revealed thickly-bedded units containing large-scale cross-stratification with bedsets of at least several meters in thickness (Squyres et al. 2009). Analysis of cross-bedding geometry suggests a paleo-wind direction oriented in a north-south direction (Hayes et al. 2011). A distinct light-toned

band lines much of the upper rim of the crater. This band served as the basis for defining stratigraphic units (Squyres et al. 2009), named after prominent geologists and stratigraphers: Lyell, Smith, and Steno, in ascending order. Smith is the light-toned band, overlain by the Steno unit, and underlain by the Lyell unit. Steno's upper contact is the base of the breccia deposit generated during Victoria crater formation; Lyell's lower contact is not exposed, buried beneath the modern sands that fill the floor of the crater.

Duck Bay is located on the western margin of Victoria crater (between promontories Cape Verde and Cabo Frio) with a slope shallow enough ( $\sim 15$  to  $25^\circ$ ) for *Opportunity* to ingress (Figure 2.2). Detailed measurements of the three stratigraphic units were taken as *Opportunity* descended into the crater.

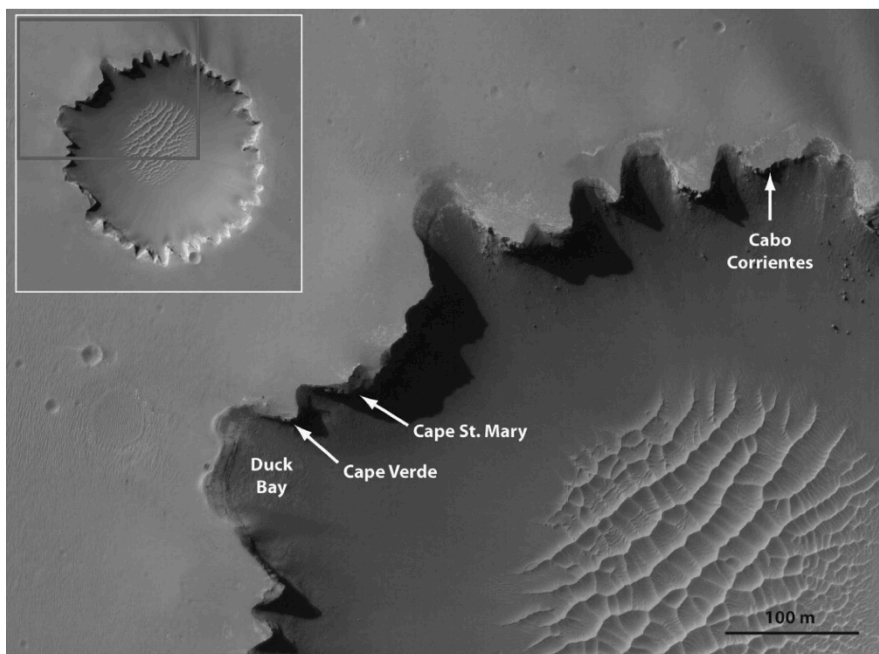


**Figure 2.2.** Duck Bay and nearby promontories Cape Verde and Cape St. Mary, seen in HiRISE image (TRA\_000873\_1780). Inset shows the crater's scalloped rim and the location of Duck Bay on the western margin of Victoria crater. Red box shows the approximate location of larger image. Image credit: NASA/JPL/University of Arizona.

## 2.3 Methodology

### 2.3.1 Instruments

The stratigraphy and bedrock sedimentary structures at Duck Bay were observed by the Panoramic Camera (Pancam) and Microscopic Imager (MI). Pancam is a multispectral imaging system, which consists of two digital cameras mounted on the rover's mast (1.5 m above the ground). Pancam is capable of both stereoscopic measurements (using parallax between the two camera "eyes", spaced 30 cm apart) and panoramic measurements (with the ability to image 360° in azimuth and +/- 90° in elevation). Pancam has a focal length of 43 mm and a field of view of 1024 x 1024 pixels (16° x 16°). Each of the two camera "eyes" includes a small eight-position filter wheel, allowing for multispectral mineralogical studies in the 400 to 1100 nm wavelength range (Bell et al. 2003).

The Microscopic Imager (MI) is a high-resolution imaging system mounted on the rover's "arm", or Instrument Deployment Device (IDD). The MI acts as both a microscope and a camera. With a camera body identical to those of Pancam, it also has a field of view of 1024 x 1024 pixels (Herkenhoff et al. 2003). The MI has a focal length of 20 mm, a +/- 3 mm depth of field, and a field of view of 31 mm x 31 mm at a working distance of 63 mm (measured from the front of the lens to the object). MI produces images with a resolution of 30 µm/pixel (Herkenhoff et al. 2003). Due to highly variable topography, MI images are usually taken as a stack of images, with the IDD moving along a path normal to the surface, pausing every few millimeters to acquire an image (Herkenhoff et al. 2003).

The rover also has the capability to grind away dust and surface alteration to expose fresh rock surfaces for chemical and textural analyses. This is accomplished by the Rock Abrasion Tool (RAT). The RAT is positioned against a rock by the rover's arm, and uses a diamond-tipped grinding wheel to remove a cylindrical area 4.5 cm in diameter and 0.5 cm deep (Gorevan et al. 2003). The RAT was designed to enhance petrologic textures of the fresh rock surfaces, so that they could be viewed effectively using the MI (Gorevan et al. 2003). However, overuse issues<sup>2</sup> (which resulted in approximately 60% of the RAT holes

---

<sup>2</sup> Encoders are attached to each of the three RAT motors, and provide precise position information to monitor the penetration process. Another wheel holds a set of spinning brushes to wipe away dust and grit, so that the abraded material is moved outward to form a dust skirt around the RAT hole. However, as the mission progressed many times beyond its planned 90-sol lifetime, problems associated with overuse have developed.

covered in RAT grindings) significantly degraded the quality of the MI images taken along the ingress path Reference Section. The presence of RAT grindings in the holes obscures some features, so caution must be used when evaluating MI images of RAT-ed targets.

### 2.3.2 Data Collection

*Opportunity* began its ingress into Victoria crater on Sol 1293. After driving 11 m downslope into the crater at Duck Bay, making detailed stratigraphic measurements of the exposed outcrop, the rover drove laterally ~20 m to investigate several scientific targets at nearby promontory Cape Verde. At its closest approach to Cape Verde, *Opportunity* maintained a ~10 m stand-off distance. While detailed chemical and textural analyses could not be acquired at this distance, super-resolution imaging allowed substantial observations of the stratification geometry and textures exposed at the cliff face. On Sol 1607, *Opportunity* began its egress, following nearly the same route as ingress, and eventually exiting the crater on Sol 1634.

*Opportunity* acquired many Pancam and MI observations over the course of nearly 150 sols on its 11 m traverse downslope. Three stratigraphic units were distinguished based on sedimentary structures, diagenetic textures and color as revealed in Pancam images. Pancam observations were made almost every sol. The Microscopic Imager provided additional information on small-scale textures and diagenetic features. The RAT was used to expose fresh surfaces in some of the IDD targets by grinding away the outermost several millimeters of rock. However, after Sol 1348, the motor encoder failure resulted in partial covering of RAT holes, which obscured some of the features of interest, so our quantitative survey of diagenetic textures used only un-RATed images. Tables 1

---

On Sol 1045, the RAT grind motor encoder failed. The MER science and engineering team developed a way to run the RAT without this encoder feedback, but on Sol 1334, the RAT revolve motor encoder failed. This meant that the RAT tool would run without precise monitoring (without knowing its exact position). On Sol 1348, the team first noticed an issue with the brush spot. Rather than clearing the grindings out of the RAT hole, only a small portion of the hole was cleared, and much of the hole contained RAT grindings. This was attributed to running the brush in the opposite direction, which resulted in a reconfiguration of the brush bristles – rather than being in line with the grinding bit, the bristles were twisted and some aligned with the z-axis, serving to erode material more than clear material out of the hole.

and 2 summarize the key MI and Pancam observations of the rock units and the sols on which they were acquired.

**Table 2.1.** Summary of MI observations.

Unit	Target name	Sols acquired	Stack	RATed
<b>Steno</b>	Steno	1311	2×2×5	none
	Steno	1313	1×1×5	brushed
	Steno	1316	2×2×5	RATed
	Steno	1320	1×1×10	RATed
<b>Smith</b>	Smith_Hall_1	1322	1×1×18	none
	Smith	1332	2×2×5	none
	Smith	1348	2×2×5	brushed
	Smith2*	1359	2×2×5	none
	Smith2 take2	1366	3×1×5	none
	Smith2	1373	2×2×3	RATed
	Smith_Lyell_Smith_side	1409	4×1×5	none
	Smith_Lyell_Smith_side	1414	1×1×5	none
	<b>Lyell</b>	Lyell_1	1384	2×2×14
Lyell_1		1395	2×2×14	RATed
Smith_Lyell_Lyell_side		1411	4×1×5	none
Lyell_B		1421	2×2×5	none
Lyell_Buckland		1430	2×2×5	RATed
Lyell_Buckland		1435	1×1×1	RATed
Lyell_Buckland		1436	1×1×4	RATed
Lyell_Exeter		1443	2×2×14	none

- Joint 1 stall, observation was not completed

**Table 2.2.** Summary of Pancam observations.

Unit	Location	Sols on which most useful images were acquired	Sols on which additional images were acquired
Steno	Duck Bay	1319, 1335, 1338, 1353, 1363, 1385	1302, 1305, 1315, 1316, 1318, 1320, 1321, 1333, 1334, 1339, 1377
Smith	Duck Bay	1332, 1335, 1337, 1349, 1350, 1351, 1353, 1366, 1374, 1385, 1426	1327, 1333, 1338, 1344, 1348, 1371, 1377, 1390
Lyell	Duck Bay	1385, 1423, 1426, 1432, 1433, 1438, 1465	1398, 1419, 1425, 1428, 1511, 1512
N/A	Cape Verde	952, 970-991, 1006, 1329, 1342, 1356, 1487, 1574-1576, 1579-1580, 1581	1329, 1342, 1346, 1349, 1358, 1457, 1472, 1473, 1487, 1570, 1572, 1599, 1611

### *2.3.3 Data Processing*

Structural attitudes were obtained by using Pancam stereo data. Range and topographic data can be derived from Pancam stereo image pairs, producing range maps out to 100 m or more from the rover (Squyres et al. 2003; Lewis et al. 2008). Occasionally, stereo images from the Navigation Camera (Navcam) also were used to produce range maps. Following the methods described by Lewis et al. (2008), linear segments along bedding planes were traced manually, and the corresponding topographic data was extracted. The natural curvature of the crater in the horizontal direction provided constraints on the three-dimensional geometry. A best-fit plane was calculated for each segment, and mathematical criteria ensured that the layers were well fit by a plane. Following Lewis et al. (2008), we determined principle component eigenvalues to describe the variance in three orthogonal directions (the first and second components describe the plane, and the third component lies out of the plane). The variance in the first principal component was limited to less than 99%, which excludes measurements for which the topography is too linear to determine the second dimension. Additionally, we excluded data for which the ratio of the variance described by the second principal component to that of the third was greater than 15, to ensure that the planar fit was significantly larger than the out-of-plane error. Strike and dip values were then calculated from the best-fit plane. The stratigraphic thicknesses reported below are true thickness, corrected for a few degrees of westward dip, obtained using the methods described above.

Super-resolution images exposed fine details in targets that the rover was unable to reach. Super-resolution is a method of combining information from a series of slightly offset images to produce a single image of the scene at higher resolution (Bell et al. 2006). The camera acquires 15 to 20 images in rapid succession at slightly offset pointings, and coregistration is performed. The images are first forward-mapped into high-resolution scratch space, and then a back propagation algorithm is repeatedly applied to the scratch space, which iteratively improves the high resolution image. Additional details are described in Bell et al. (2006).

### 2.3.4 Simulations

Several bedform simulations were run and cross-bedding geometries were compared to those observed in outcrop to test potential bedform morphologies and behaviors. We used a code that mathematically simulates bedforms and cross-bedding, developed by Rubin and Carter (2005). The code approximates bedform surfaces as sine curves. Bedform migration is created by displacement of the sine curves, height is produced by changing the amplitude, and superimposed bedforms can be modeled as combined sets of sine curves. The resulting block diagrams can be compared to cross-bedding observed in rock outcrops in a variety of geometries.

## 2.4 Duck Bay Sedimentology and Stratigraphy

*Opportunity's* ingress path in Duck Bay intersects three stratigraphic units, named Lyell, Smith and Steno, in ascending stratigraphic order (Figure 2.3). These units, as observed along the rover ingress path, define the “Reference Section” for Victoria crater. The definitions and descriptions presented here form a set of observations that can be used for the purpose of comparison to other locations in the crater, and for inter-regional correlations between craters. Changes in stratigraphic attributes relative to a defined Reference Section form the traditional basis for understanding lateral and temporal variations in depositional environment.

### 2.4.1 Lyell Unit

The lowermost unit, designated as “Lyell,” consists of ~1.8 m of sulfate-rich sandstone (Squyres et al. 2009). Lyell is characterized by its darker tone, with well-defined pinstripe laminations. The average bed thickness is ~2 mm. It is a well-sorted, fine-grained sandstone, with meter-scale cross-bedding (Figure 2.4e). Strike and dip measurements, calculated from Pancam stereo data, indicate that Lyell dips approximately 2° to the west – away from the center of the crater. Measurements of cross-strata indicate dip directions to the SW (Figure 2.5).

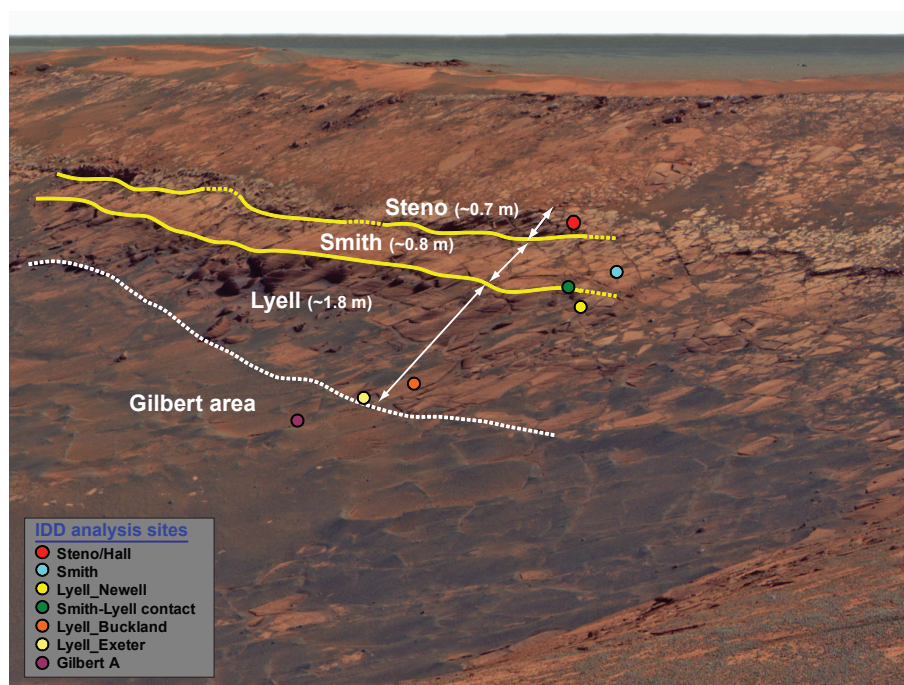


**Figure 2.3.** Ingress path as viewed from Cape Verde promontory (Cape Verde panorama, L257 false color mosaic, acquired during Sols 970-991). Three distinct units are visible in Duck Bay, named Lyell, Smith and Steno, in ascending order. The Gilbert area corresponds with brecciated bedrock below the intact unit Lyell. Stratigraphic thicknesses (reported in parentheses) were derived from Pancam stereo images. Colored circles correspond to locations of detailed analyses by the Microscopic Imager (MI) as well as other tools on the Instrument Deployment Device (IDD).

The MI provided additional information on small-scale textures and diagenetic features, including abundant hematite-rich spherules and vugs suggestive of crystal molds (Figure 2.4f). Volumetric densities of spherules were estimated following McLennan et al. (2005), using the relation  $V = (\pi m l^2 / 6A)$  where  $m$  is the number of spherules on a planar rock surface with area  $A$ , and  $l$  is the mean spherule diameter. Spherules in Lyell range from 0.5 mm in diameter up to 1.5 mm, with an average diameter of 0.90 mm (SD = 0.27, 378 spherules). Lyell has more embedded spherules than Smith or Steno, with a volumetric density of 1.04% (SD = 0.46,  $n = 16$  frames) (Table 3). Lyell also contains abundant vugs, with tabular-prismatic shape, and random orientations. The vugs in Lyell have a typical width of ~0.25 mm and length of 1 to 2 mm. While the vugs show similar geometry and similar proportions to those seen in Eagle crater (Squyres et al. 2004b) they

are an order of magnitude smaller. The vugs may contribute to the darker tone of this unit, helping to trap dark, probably basaltic sand grains (Squyres et al. 2009).

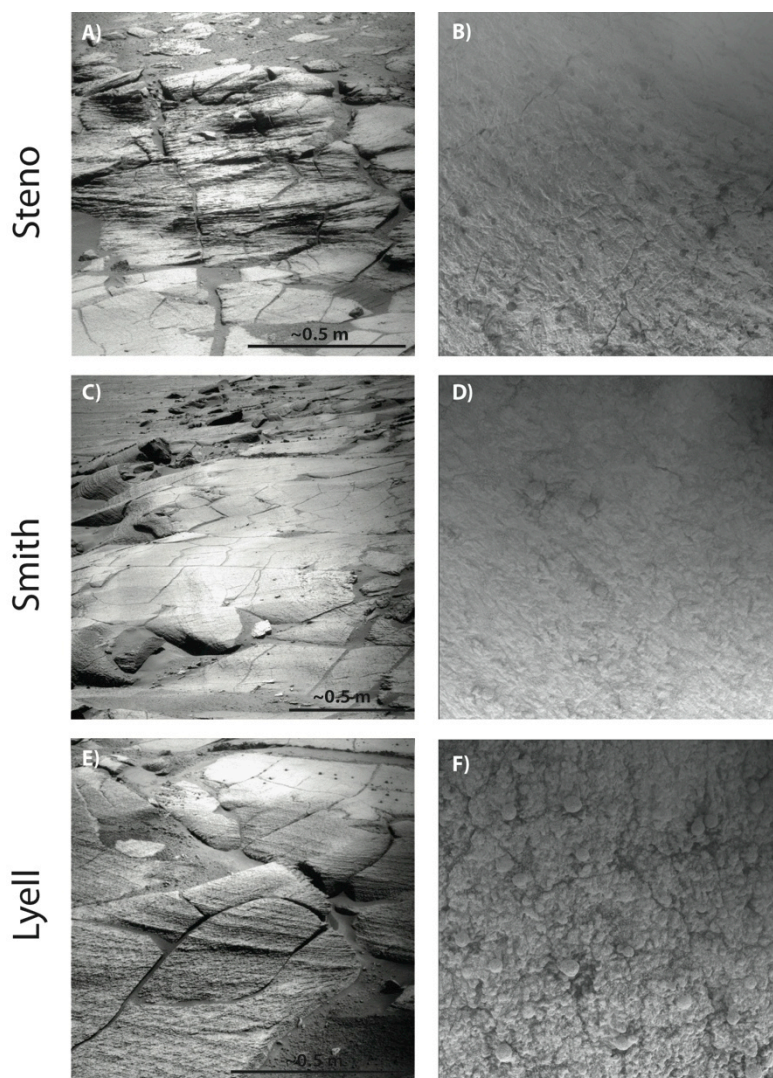


**Figure 2.4.** Pancam (left) and MI (right) images of Lyell, Smith and Steno, documenting the large and small-scale characteristics of the three different units in the ingress path. For scale, MI images are 31 mm on a side. MI images were taken with target fully shadowed. Note that the dark upper right corner of each MI image is the result of dust contamination of the MI optics. A) In the ingress path Steno appears as a more resistant step in topography. B) Steno consists of fine-to-medium grained sandstone with abundant hematite spherules. C) and D) Smith is characterized by its lighter tone and smoother texture at both scales. E) Lyell is characterized by its darker tone (Smith is visible in the upper right portion of the image for comparison) and well-defined pinstripe laminations. F) MI images of Lyell reveal numerous hematite spherules and vugs. Spherules in Lyell are larger and more abundant than those in Steno or Smith.

### 2.4.2 *Smith Unit*

The light-toned Smith unit directly overlies the Lyell unit. The contact between Smith and Lyell is gradational, and the darker tone and well-defined stratification of Lyell gradually fade upward. Smith is characterized by its smoother texture and lighter-tone, which contrasts with its bounding units (Figure 2.4c). The Smith unit at first appears massive, but images taken at low solar incidence angles reveal fine lamination, with lamina thicknesses similar to those in Lyell, on the order of ~1 to 2 mm. Smith dips approximately 2° to the west, and has a thickness of ~0.8 m (consistent with other exposures around the crater (Hayes et al. 2011)).

Smith has fewer spherules than Lyell (Figure 2.4d), with a volumetric density of 0.35% (SD = 0.15%,  $n = 14$  frames). Spherules in Smith have an average diameter of 0.73 mm (SD = 0.50 mm; 162 spherules). The lighter tone and poor expression of lamination of Smith suggests that Smith is recrystallized.

### 2.4.3 *Steno Unit*

Along the ingress path, a clear erosional contact distinguishes Smith from the overlying Steno unit. Inclined stratification in Smith is truncated by the lower bounding surface of Steno. Strike and dip measurements suggest that this truncation surface between Steno and Smith has a dip of ~10° to the southeast. The beds above the erosional contact conform to the surface and dip predominantly to the southeast (Figure 2.5). Measured as a true stratigraphic thickness, Steno consists of ~0.7 m of sandstone. This measurement represents a minimum thickness due to erosion at the top of the unit, which coincides with the Amazonian weathering surface of Meridiani; the unit is overlain by impact breccia.

The Steno unit is composed of fine-to-medium-grained sandstone, with well-defined laminae, on the order of ~2 mm in thickness. Centimeter-to-meter scale cross-bedding is visible in places. In the ingress path, Steno shows a varied appearance when weathered – appearing as a more resistant step in topography (Figure 2.4a). Often it has a rougher surface texture and has a darker tone but sometimes it displays a smoother texture and lighter tone.

The spherules in Steno are relatively uniform in size and shape, with a mean diameter of 0.72 mm (SD = 0.19 mm; 80 spherules). Steno has more spherules than Smith but fewer than Lyell, with a volumetric density of 0.46% (SD = 0.1%;  $n = 5$  frames). Steno also contains crystal-form vugs similar to those in Lyell, but less abundant.

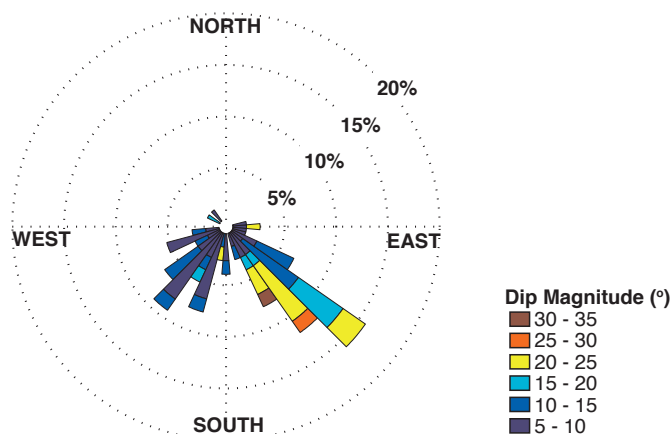


**Figure 2.5.** Rose diagram of bedding dips at Duck Bay, following methods of Hayes et al. (2011). Colors correspond to dip magnitudes. Dip directions to the southwest correspond to measurements of cross-bedding in Lyell, while dip directions to the southeast correspond to measurements of cross-bedding in Steno. Bedding was not measured in Smith due to the poor expression of bedding.

#### 2.4.4 Chemostratigraphy

In addition to observing the physical stratigraphy and diagenetic textures of the different rock units in Duck Bay, *Opportunity* made measurements of chemical and mineralogic compositions, which we will briefly summarize here. Locations of the chemical measurements are represented by colored circles in Figure 2.3, corresponding to labeled points in the stratigraphic column (Figure 2.6). Overall, the rock compositions measured in Duck Bay fall within the range of rocks observed at previous craters studied by *Opportunity*, and suggest that the rock units are composed of sulfates and silicates in slightly varying abundances (Mittlefehldt et al. 2008). Notable compositional differences include more S in Steno than previously observed at Meridiani (Squyres et al. 2009), and more Zn in Smith (24% higher) than any other rock yet observed (Mittlefehldt et al. 2008).

Smith and Lyell both show an increase in Cl content compared to Steno – Lyell reveals more than a factor of two increase in Cl compared to Steno (Mittlefehldt et al. 2008). The chemostratigraphic trends in Duck Bay are similar to those measured at Endurance crater – both sections reveal a decrease in S, Fe, and Mg down-section, and corresponding Al and Si enrichment (Squyres et al. 2009). The chemostratigraphic similarities between Endurance and Victoria may reflect the recurrence of depositional and diagenetic processes through time (Squyres et al. 2009), or it may reflect downward-penetrating diagenesis related to surface exposure (Amundson et al. 2008).

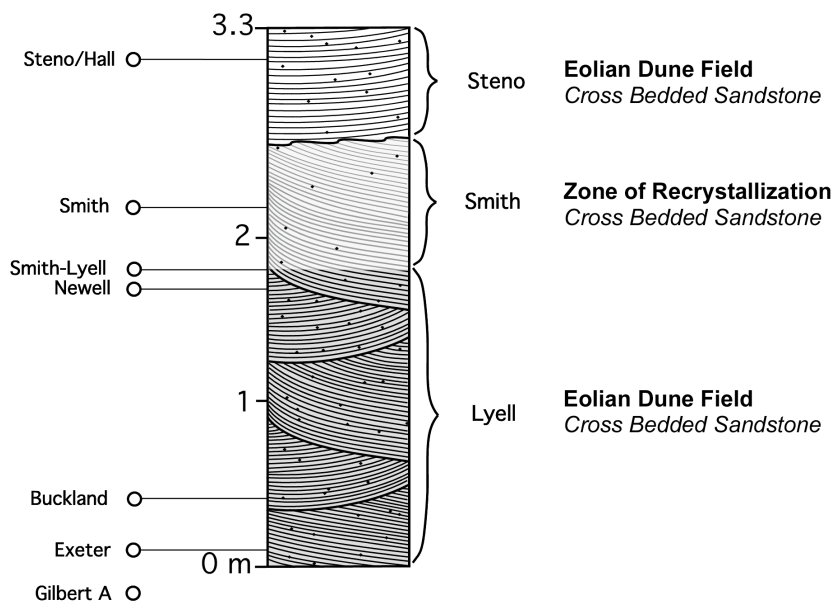


**Figure 2.6.** Duck Bay stratigraphic column. Thicknesses are corrected for 2° dip to the west. Left-hand-side shows locations of IDD targets (Gilbert A was sampled from a brecciated block below the intact unit Lyell). Smith is interpreted as a diagenetic band superimposed on cross-bedded sandstone. In the ingress path Smith is also bounded by an erosional contact with Steno.

## 2.5 Correlation to Cape Verde

The three stratigraphic units are visible around much of Duck Bay, but they cannot be directly correlated with the nearest promontory, Cape Verde (Figure 2.7). A large area of brecciated bedrock separates the ingress path stratigraphy from that at the

promontory, prohibiting the direct tracing of beds. Although the rover was unable to reach the cliff face at Cape Verde, detailed observations of several science targets were made through super-resolution imaging at the rover's closest approach (~10 m stand-off distance). The strata exposed at Cape Verde contain a light-toned band similar in thickness to that of Smith. Here it overprints well-laminated sandstone with low-angle cross-bedding. Strata near the base of the cliff face have planar lamination to low angle cross-stratification, with dips that steepen upward in the upper half of the cliff face. Super-resolution imaging also reveals small climbing ripples super-imposed on the larger dune cross-stratification (Figure 2.7c).

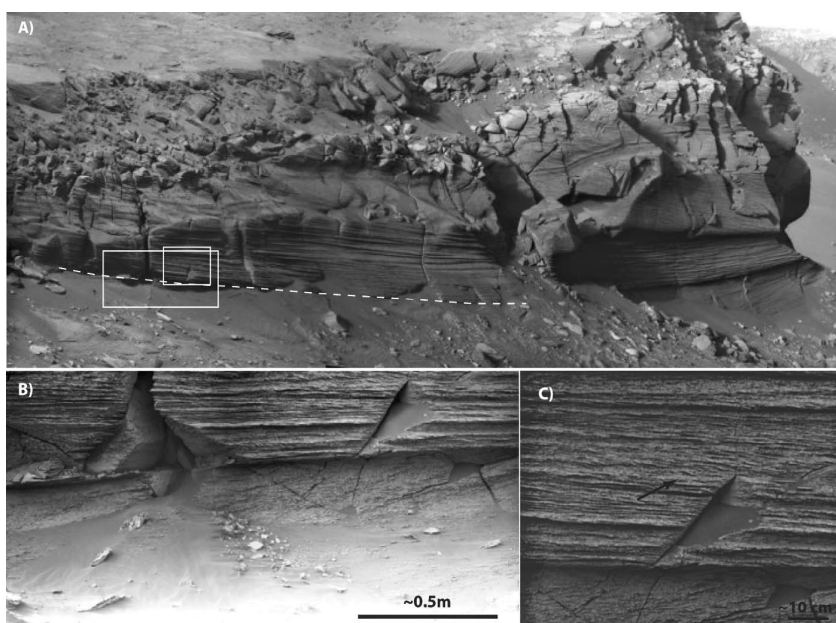


**Figure 2.7.** Cape Verde erosional surface. A) White dashed line shows location of erosional surface at the base of Cape Verde, dipping approximately  $10^\circ$  to the southeast (to the right in the above image) (Cape Verde super-resolution mosaic acquired during Sols 1342-1356). White boxes show locations of B and C. B) Super-resolution image of erosional surface. Below the erosional surface, bedrock is exposed in the slope, with angled beds truncated by low-angle cross-stratification in the cliff face (Cape Verde super-resolution mosaic acquired during sols 1574-1576). C) Cross-strata represent ripples climbing toward the upper right portion of the image (arrow) (Cape Verde mosaic acquired during Sols 1579-1580).

The base of the cliff face contains a truncation surface (Figure 2.7). *Opportunity* was unable to do a detailed analysis on the bedrock underlying this truncation surface, although a few exposures of bedrock suggest that the strata are inclined relative to those that overlie the surface (Figure 2.7b). The truncation surface has a dip of  $\sim 10^\circ$  to the southeast (Hayes et al. 2011); given that the erosional contact at the base of Steno also has a  $\sim 10^\circ$  dip, it seems likely that these surfaces are related, and likely represent scour by the same migrating bedform). This is further supported by the observation that the two exposures of the truncation surface lie in the same plane.

## 2.6 Paleo-Depositional Environment

The primary sedimentary structures and diagenetic textures preserved in the ingress Reference Section at Victoria Crater define two facies. These include cross-bedded sandstone and planar-laminated to low angle cross-stratified sandstone. These facies require transport of sand under turbulent flows to generate bedforms ranging in scale from centimeters to meters. The dunes that deposited the cross-strata observed at Duck Bay and Cape Verde were probably an order of magnitude greater than 1 m, likely on the order of 10s of meters, as suggested by Rubin and Hunter (1982), as calculated from the preservation ratio [(mean thickness of preserved sets)/(mean topographical height)] for dunes (0.12) proposed by Paola and Borgman (1991), or inferred from the ratio of preserved set thickness to complete dune height Mountney et al. (1999) observed for eolian dunes and cross-strata buried by lava. The abundance of planar, low-angle cross-stratification, meter-scale cross-stratification, and pinstripe laminae (diagnostic of deposition by wind ripples (Hunter, 1977)), are most consistent with an eolian depositional environment. These observations and their inferred depositional environment are similar to what has been proposed previously for other locations studied by *Opportunity*.

However, in the interpretation of cross-stratified facies in Meridiani Planum, it is necessary to consider two alternative depositional models. Knauth et al. (2005) propose that the Meridiani strata represent an impact-induced base surge, and McCollom and Hynek (2005) propose that the strata were deposited during a volcanic base surge. These depositional models can be discounted on several grounds: 1) lack of evidence for

contemporaneous sources of volcanism or impacts of sufficient size to produce base surge deposits (Squyres et al. 2006a; McLennan and Grotzinger, 2008); 2) spherules are dispersed relative to bedding (McLennan et al. 2005) rather than concentrated along bedding planes as would be expected if they were accretionary lapilli or iron condensation spherules, and 3) the scale of the cross-bedding exposed in Victoria crater (reconstructing to bedforms on the order of meters to tens of meters) has not been observed in any known base surge deposits. Therefore, the most probable explanation for the origin of cross-stratified facies at Victoria crater is that they were produced in an eolian depositional environment.

### *2.6.1 Deposition and Diagenesis at Duck Bay*

Lyell and Smith, as defined in the Reference Section at Duck Bay, were likely deposited as part of the same eolian dune package, as evidenced by the gradational contact between them. Steno is a distinct stratigraphic unit marked by an erosional contact, which separates it from the light-toned unit Smith. While Smith is bounded by the erosional contact below Steno, its presence above the erosional contact at Cape Verde suggests that Smith cross-cuts the primary bedding. This relationship is consistent with observations made at other exposures around the crater (Hayes et al. 2011). Small-scale diagenetic features suggest that Smith is recrystallized. Lyell shows the highest density of vugs and spherules, followed by Steno, and Smith shows the lowest density. The lighter tone, smooth appearance and lack of vugs are the result of recrystallization. It is clear that Smith owes its unique identity to diagenesis, but the key question is when that diagenesis occurred.

The observation that the diagenetic band has a low dip and is found near the rim of the crater raises hypotheses that it may be due to processes related to the Meridiani plains (intersection with the ground water table?), or it may be due to processes related to the crater impact (impact-induced melting of ice?). The fact that the diagenetic band is brecciated, and in some outcrops reworked upward into the impact breccia (Figure 2.8) indicates that the diagenetic band was not formed during or after the crater impact. The diagenetic band must postdate deposition of the eolian strata, but predate the crater impact.

We also observe a low density of spherules in the diagenetic band. This may be explained by recrystallization prior to the precipitation of spherules. Early recrystallization of Smith may have eliminated pore space so subsequent ground water infiltration would not precipitate as many spherules in Smith as there are in Steno and Lyell.

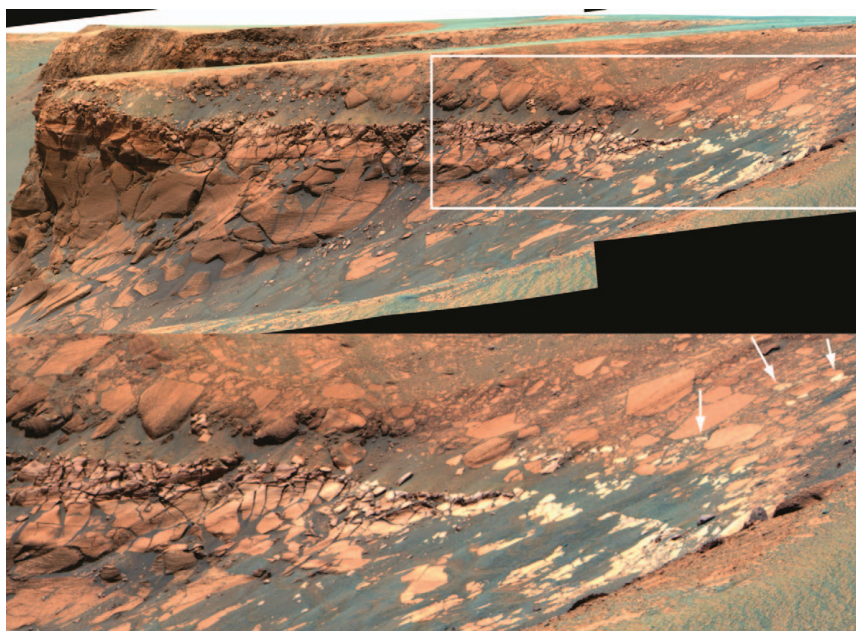


**Figure 2.8.** Cabo Corrientes false color mosaic acquired on Sol 1108. The false color stretch brings out subtle color differences in the outcrop, highlighting small blocks of the diagenetic band that are reworked into the impact breccia (white arrows point to several blocks). The diagenetic band (“Smith” as described in the ingress section) is interpreted to have formed after deposition but before the crater impact.

## 2.7 Interpretation of Eolian Stratigraphic Architecture

The recognition of cross-bedding geometry and bounding surfaces in ancient eolian deposits can be used to reconstruct wind direction, the nature of dune migration, and ultimately the sequence of events that produced the deposit. In turn, this may enable some understanding of changes in climate, sand supply, and possible subsidence. However, we are working with much more limited data than most terrestrial studies of this nature, constrained by the few bedrock outcrops observed by the rover, and by limited stereo coverage. Given the available data, we will consider a list of possibilities for the origin of the stratification exposed at Duck Bay and Cape Verde.

We begin by considering the truncation surface between Steno and Smith in the ingress path. As discussed above, we infer that the erosional contact at the base of Steno correlates with the erosional surface at the base of the Cape Verde cliff face. Although these surfaces lie at different elevations, they have a similar dip of approximately  $10^\circ$  into the crater, and projection of this dip shows the potential continuity of the surface between elevations. The surface spans an area of least  $300 \text{ m}^2$  (limited by the few outcrops observed by the rover) and may represent an architectural element larger than the scale of the dune cross-bedding. In this case the erosional surface may be interpreted as a bounding surface produced by migration of dunes on a larger bedform (*cf.*, Fryberger 1993). The compound bedform (smaller dunes migrating over a larger dune) may be termed a draa. Figure 2.9 provides a reconstruction of the stratigraphy between the reference section along the ingress path, and at Cape Verde. Note the crosscutting relationship of the diagenetic unit Smith, and the position of the truncation surface.

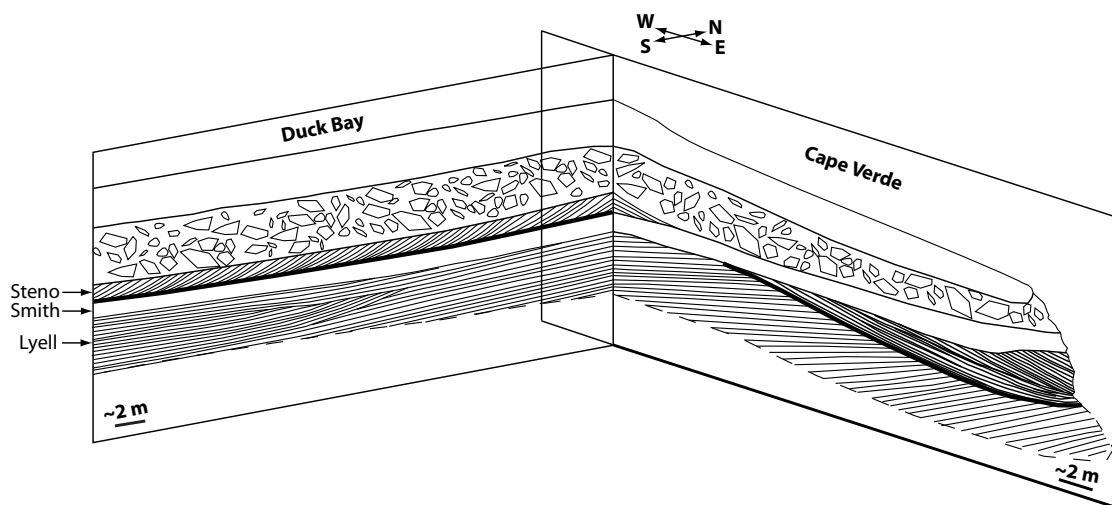


**Figure 2.9.** Schematic fence diagram depicting the three-dimensional geometry of the stratigraphy exposed at Duck Bay and Cape Verde. The diagenetic band Smith (white) crosscuts the erosional surface (heavy black lines). The erosional contact between Steno and Smith in the ingress path lies in the same plane as the erosional surface at the base of the Cape Verde cliff face. Note: the region at the intersection of these planes is inferred due to a lack of intact bedrock connecting Duck Bay and Cape Verde.

Further consideration of cross-bedding geometry produces additional insight. Strata below the erosional surface, both at Duck Bay and at Cape Verde, dip to the southwest, while the strata above the surface dip to the southeast. This leads to two possible interpretations. The different dip directions may be interpreted as remnants of three-dimensional sinuous crested dunes migrating southward. In this scenario, the strata dipping to the southwest would represent deposition on the west-dipping surface of the east side of a southward-migrating topographic depression. The strata dipping to the southeast would represent deposition on the east-dipping surface of the west side of a southward-migrating topographic depression (Figure 2.10). Trough cross-bedding produced by three-dimensional sinuous crested dunes is observed at nearby promontory Cape St. Mary, though the scale of the bedsets is much smaller (Hayes et al. 2011).

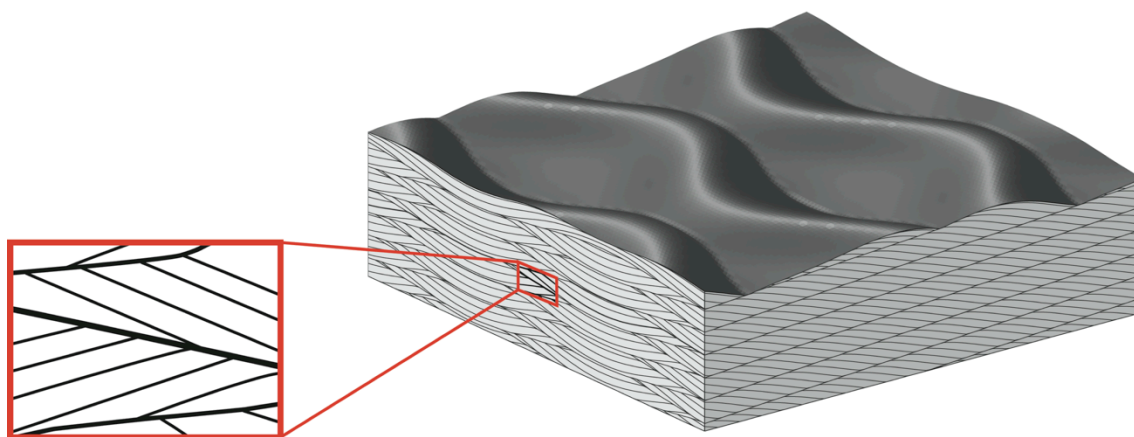


**Figure 2.10.** 3D sinuous crested bedforms, modified from Rubin (1987). The red box highlights a section perpendicular to the flow direction, showing a bounding surface (bold line) with strata above and below the bounding surface dipping in opposite directions. In the case of Cape Verde, the strata below the bounding surface may have been deposited on the east side of a southward migrating depression (strata below the bold line) whereas the strata above the erosional surface may have been deposited on the west side of a southward migrating depression (strata above the bold line).

Alternatively, the different dip directions could be indicative of different dune-migration directions, from which paleo-wind directions maybe inferred. This interpretation is consistent with observations of terrestrial draas, which may contain reactivation surfaces representing the migration of dunes across a draa in different directions (McKee, 1966).

Work by Hayes et al. (2011) indicate that a pattern of reversing transport direction is observed at other locations around Victoria crater, and also with juxtaposition of cross-bed sets across larger-scale surfaces.

Figure 2.11 illustrates this shift in wind directions, and the resulting cross-stratification. Using the model of Rubin and Carter (2005), we produce a large transverse bedform migrating from N to S, with superimposed bedforms that reverse migration direction. To model a reversal in wind direction, we allow the superimposed bedforms to reverse migration direction and asymmetry. While the superimposed bedforms reverse migration direction, their heights are decreased and then increased. The superimposed bedforms initially migrate from E to W, then reverse direction and migrate from W to E. The resulting stratification shows a subset of crossbeds at the base that dip to the SW, and an overlying subset of crossbeds that dip to the SE (this is illustrated most clearly at the front corner of the block). The bounding surface that separates the two subsets dips to the S (note: in actuality, the bounding surface at Duck Bay and Cape Verde dips to more to the SE). A snapshot of the preserved cross-stratification may reveal a bounding surface with cross-strata above and below the surface dipping in different directions, indicating a potential reversal in wind direction. This is analogous to the stratal geometry observed at the base of Cape Verde.

Given the available data, we are unable to distinguish between these two hypotheses. However, in both scenarios, the inferred net transport direction is roughly N to S, which is consistent with the inferred paleowind directions measured at other locations around the crater (Hayes et al. 2011). In the case of a large bedform with superimposed bedforms that reverse migration direction, the orientation of the erosional surface (rather than the cross-strata above the surface) may serve as a better indicator of the local orientation of the bedform surface when it was formed. Rubin and Hunter (1983) have shown that in compound cross-stratification, the orientation of a bounding surface scoured by superimposed bedforms serves as a more accurate indicator of draa orientation than the dip orientation of cross-strata (note that this result holds for situations where the surface slope of the main bedform is relatively steep;  $10^\circ$  is likely steep enough for this to be a better approximation than the cross-beds deposited by the superimposed bedforms). Cross-

stratification – especially trough cross-stratification – can display a wide range of dip directions (up to 180°) even in a unidirectional wind; if only a small sample of these dip directions are measured – as is the case for Victoria crater – then the results might not be representative of the actual range of dips. In contrast, the dip direction of bounding surfaces scoured by superimposed bedforms is oriented roughly perpendicular to the dune brink, and therefore serves as a more accurate indicator of the primary dune migration direction.

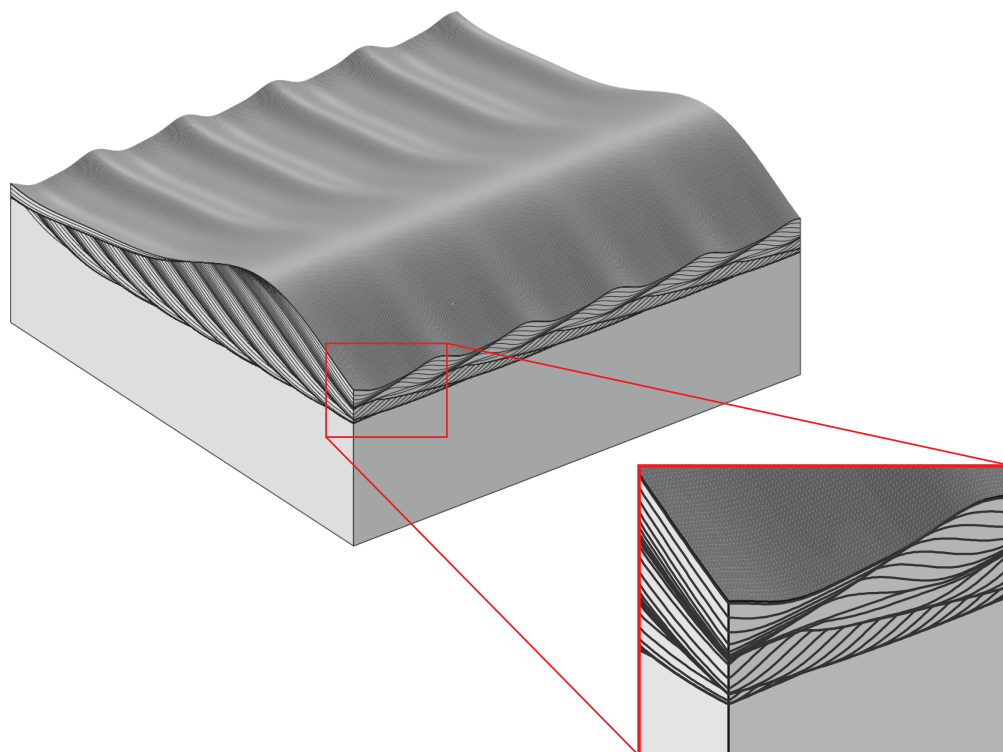


**Figure 2.11.** Depositional model for the stratal geometry at the base of Cape Verde, using code modified from Rubin and Carter (2005). Model illustrates the stratification produced by a large transverse bedform migrating from N to S, with superimposed bedforms that initially migrate from E to W, then reverse direction and migrate from W to E. The resulting stratification shows a subset of crossbeds at the base that dip to the SW, an overlying subset of crossbeds that dip to the SE, and a bounding surface separating the two subsets that dips to the S. A snapshot of the preserved cross-stratification may reveal a bounding surface with cross-strata above and below the surface dipping in different directions, indicating a potential change in wind direction, analogous to the stratal geometry observed at the base of Cape Verde.

The Algodones dune field in southern California provides an excellent terrestrial example of a draa oriented roughly perpendicular—but not perfectly perpendicular—to the long-term resultant transport direction, with superimposed features driven by the secondary airflow (Havholm and Kocurek, 1988). Havholm and Kocurek (1988) found that on the lee slope of a draa, surface airflow and the migration of superimposed bedforms is typically oblique or parallel to the draa brinkline, highlighting the importance of these bounding surfaces in reconstructing paleowind directions in the rock record. At Victoria crater, the erosional surface dips  $10^\circ$  to the southeast. If this surface is a bounding surface scoured by a superimposed bedform, then the bounding surface may reflect the true orientation of the draa brinkline, migrating from northwest to southeast.

The erosional surface at Duck Bay and Cape Verde is also important in that it exposes a larger scale bedform than previously seen in Meridiani Planum. If it represents the migration of dunes across a draa, then three orders of bedforms are observed at Duck Bay and Cape Verde: ripples, dunes, and draas. Draa deposits appear to be a common feature in the terrestrial rock record. Draas are typical of modern ergs (sand seas), often occurring in the centers of well-developed ergs where sand cover is thickest (Wilson, 1971; Havholm and Kocurek, 1988). These conditions favor preservation, so draa deposits would be expected to be widespread in the rock record of eolian deposits on Earth (Havholm and Kocurek 1988) and in similarly arid environments on Mars. The three orders of bedforms observed at Cape Verde suggest that ancient dune field glimpsed by *Opportunity* may have been a large sand sea (erg) (although the size of the reconstructed bedforms is somewhat smaller than terrestrial bedforms thought to have been deposited in eolian environments, such as the Navajo Sandstone (Rubin and Hunter, 1982)).

The dunes in the center of Victoria crater provide a modern example of a dune field with multiple orders of bedforms, analogous to the ancient dune field preserved in outcrop. Pancam images reveal intersecting dunes in the center of the crater, with smaller superimposed dunes riding on the backs of the larger dunes (Figure 2.12). The crater provides a confined basin for deposition, and complex wind patterns shape the sediment into star dunes. Modified secondary airflow builds smaller dunes on the backs of the larger dunes. Using a Digital Elevation Model (DEM) produced from stereo images from the

orbiting High Resolution Imaging Science Experiment (HiRISE), we obtained estimates of dune heights ranging from 2 to 5 m. While these are somewhat smaller than the estimated height of the ancient dunes preserved in the Victoria bedrock, this modern example suggests that processes that governed ancient deposition are still acting on the modern Martian surface.

One feature that is notably absent from the bedrock outcrops at Victoria crater is evidence for brief periods of aqueous deposition, as observed at Eagle, Endurance and Erebus craters (Grotzinger et al. 2005; Metz et al. 2009). Metz et al. (2009) suggest that as the rover has moved stratigraphically higher through Eagle, Endurance and Erebus craters, that it has observed a full climatic cycle, from dry to wet to dry. The bedrock outcrops at Victoria crater represent a stratigraphically higher section than that observed at Eagle and Endurance craters, and may represent even drier climatic conditions and

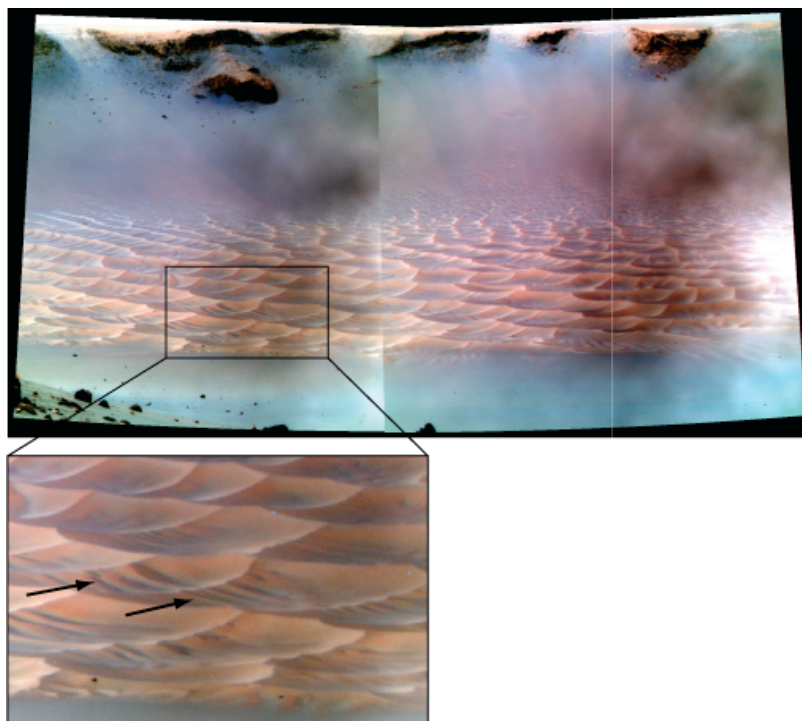


**Figure 2.12.** Modern dunes in the center of Victoria crater (Pancam false color image acquired on Sol 1437). Maximum dune heights range from 2 to 5 m, as determined from a HiRISE DEM. Close-up image shows small superimposed dunes (black arrows) migrating across larger star dunes. While these superimposed dunes may be analogous to the ancient bedforms inferred at Duck Bay and Cape Verde, they are an order of magnitude smaller.

increased sediment flux. This allogenetic hypothesis suggests that the conditions at a given point changed through time as a result of a changing climate. Alternatively, the lack of evidence for aqueous deposition may indicate lateral variations in time-equivalent facies. Victoria crater may expose strata from the center of a well-developed sand sea, whereas strata in Eagle and Endurance craters may represent a depression (or depressions) within the sand sea and be more prone to the emergence of ground water. In this autogenetic scenario, the degree of wetness of the depositional environment would depend more on local elevation relative to the water table, with changes in wetness controlled by thickness of dry sand. The outcrop exposed in the Reference Section at Duck Bay appears to lie at a similar elevation as the uppermost unit exposed in Erebus crater. The upper unit of the Yavapai formation is interpreted to represent sandsheet/dune field facies (Metz et al. 2009). It is possible that the upper unit at Erebus represents the same period of deposition observed in the ingress path at Duck Bay, but the larger scale of the outcrops at Victoria crater exposes the stratal geometries consistent with construction of larger-scale eolian bedforms.

## **2.8 Conclusions**

The strata exposed at Duck Bay and Cape Verde indicate deposition in an eolian dune environment, with further modifications through diagenesis. Images from the Panoramic Camera and Microscopic Imager reveal three distinct stratigraphic units in the Reference Section traced by the rover ingress path: Lyell, Smith and Steno, in ascending order. In the Reference Section, Smith is interpreted as a secondary, diagenetic unit, which also is bounded by a primary, erosional contact, but elsewhere in the crater the diagenetic band crosscuts the primary stratigraphic surfaces. Evidence of the diagenetic unit reworked in the impact breccia indicates that Smith formed prior to the crater impact. Correlation with nearby promontory Cape Verde reveals that there is an erosional surface at the base of the cliff face that likely corresponds to the erosional contact below Steno. This surface is

interpreted to represent the migration of dunes across a draa, and its orientation suggests that the draa was migrating from northwest to southeast at the time that the surface was formed. The stratal geometry above and below the erosional surface suggests dune migration in opposing directions, or by southward migrating three-dimensional bedforms. Additionally, the presence of three orders of bedforms and a complex wind regime suggest that the strata may have been part of a large sand sea, with no evidence for aqueous deposition as observed at Eagle and Endurance craters. Victoria crater not only reveals the regional extent of processes seen elsewhere in Meridiani Planum, but the greater size of its outcrop exposures reveals the building of ever larger eolian bedforms.

*Chapter 3*HYPOTHESES FOR THE ORIGIN OF FINE-GRAINED SEDIMENTARY ROCKS  
AT SANTA MARIA CRATER, MERIDIANI PLANUM

Submitted:

Edgar, L. A., J. P. Grotzinger, J. F. Bell III, and J. A. Hurowitz (in review), Hypotheses for the origin of fine-grained sedimentary rocks at Santa Maria Crater, Meridiani Planum, *Icarus*.

**Abstract**

En route to Endeavour crater, the Mars Exploration Rover *Opportunity* embarked on a short but significant campaign at Santa Maria crater during Sols 2450 to 2551. Santa Maria crater is a relatively young impact crater, approximately 100 m in diameter and 11 to 17 m deep. *Opportunity* performed detailed analyses on several ejecta blocks and completed an extensive imaging campaign around the crater. Many of the ejecta blocks are composed of sandstone with abundant wind ripple laminations suggestive of eolian deposition. However, other ejecta blocks are massive, fine-grained, and exhibit a nodular texture. These rocks are interpreted to be the first rocks of a grain size smaller than the Microscopic Imager can resolve, and may represent the first mudstones observed by the rover. Several depositional environments are considered for the origin of the fine-grained rocks, and the observations are best fit by a transient evaporitic lake. If the inferred mudstones were deposited in a lacustrine setting, then surface water may have been present in a broader range of surface environments than previously documented at Meridiani Planum.

### 3.1 Introduction

For the past eight and a half years, the Mars rover *Opportunity* has been exploring sedimentary rocks exposed in impact craters at Meridiani Planum (*e.g.*, Squyres et al., 2006b, 2009; Arvidson et al., 2011). Key scientific investigations were carried out at Eagle, Endurance, Erebus, Victoria and Santa Maria craters (Figure 3.1). Of particular interest is the examination of rocks formed in aqueous environments, because of their implications for the potential habitability of ancient Martian surface environments. Substantial evidence for aqueous activity was discovered at Eagle, Endurance, and Erebus craters (Squyres et al., 2004b; Clark et al., 2005; Grotzinger et al., 2005; McLennan et al., 2005; Grotzinger et al., 2006; Metz et al., 2009). The sedimentary rocks exposed at these craters—collectively named the Burns formation—are interpreted to record a dry to wet eolian depositional system (Grotzinger et al., 2005, 2006; Metz et al. 2009). Bedrock outcrops at Victoria crater, however, reveal eolian environments with no evidence for water-lain sediments (Edgar et al., 2012). At each of these craters, sediments are interpreted to have been derived from reworked playa mudstones, with pore-water fluids that were ultimately sourced from acid-sulfate weathering of basalt (McLennan et al., 2005; McLennan and Grotzinger, 2008). At each of these sites, regardless of primary depositional facies, there is evidence for diagenesis involving the formation of hematite concretions, precipitation of crystals now represented by pseudomorphs, and recrystallization. Each new outcrop exposure allows the testing and refinement of models for sediment production, transport, deposition and erosion. Significantly, only fine-to-medium-grained sandstones have been observed in the course of detailed examination of these outcrops. To date, no more finely grained rocks have been reported; such rocks could

provide substantial additional support for the hypothesis of a lacustrine depositional environment, which is inferred to have been the source for at least some of the Burns formation.

After leaving Victoria crater, *Opportunity* set out on a three-year trek to reach Endeavour crater, but the rover made several stops along the way. One of those stops was at Santa Maria crater, which is located ~ 7 km southeast of Victoria crater and exposes a lower stratigraphic level than had been previously. Observations of ejecta blocks at Santa Maria crater reveal primarily eolian stratification, in addition to a new facies that is characterized by massive, and sometimes nodular, fine-grained sedimentary rocks that we interpret here as potential mudstones or duststones.

### **3.2 Geologic Setting and Methods**

Santa Maria is a relatively young impact crater located at 2.172° S, 5.445° W. It is approximately 100 m in diameter and 11 to 17 m deep (Watters et al. 2011). Topographic measurements made by the Mars Orbiter Laser Altimeter indicate that the plains surrounding Santa Maria crater are approximately 100 m lower in elevation than those surrounding Victoria crater. If bedding is horizontal, as is reconstructed for Victoria crater (e.g., Hayes et al., 2011), bedrock at Santa Maria crater should represent a substantially lower stratigraphic section than anything examined to date. *Opportunity* explored the crater during Sols 2450 to 2551, and performed an extensive imaging campaign as it drove around the crater from the western rim to the southeastern rim. The stratigraphy exposed in crater walls is not intact and the rover did not drive down into the crater, but *Opportunity* was able to perform detailed analyses of several ejecta blocks.

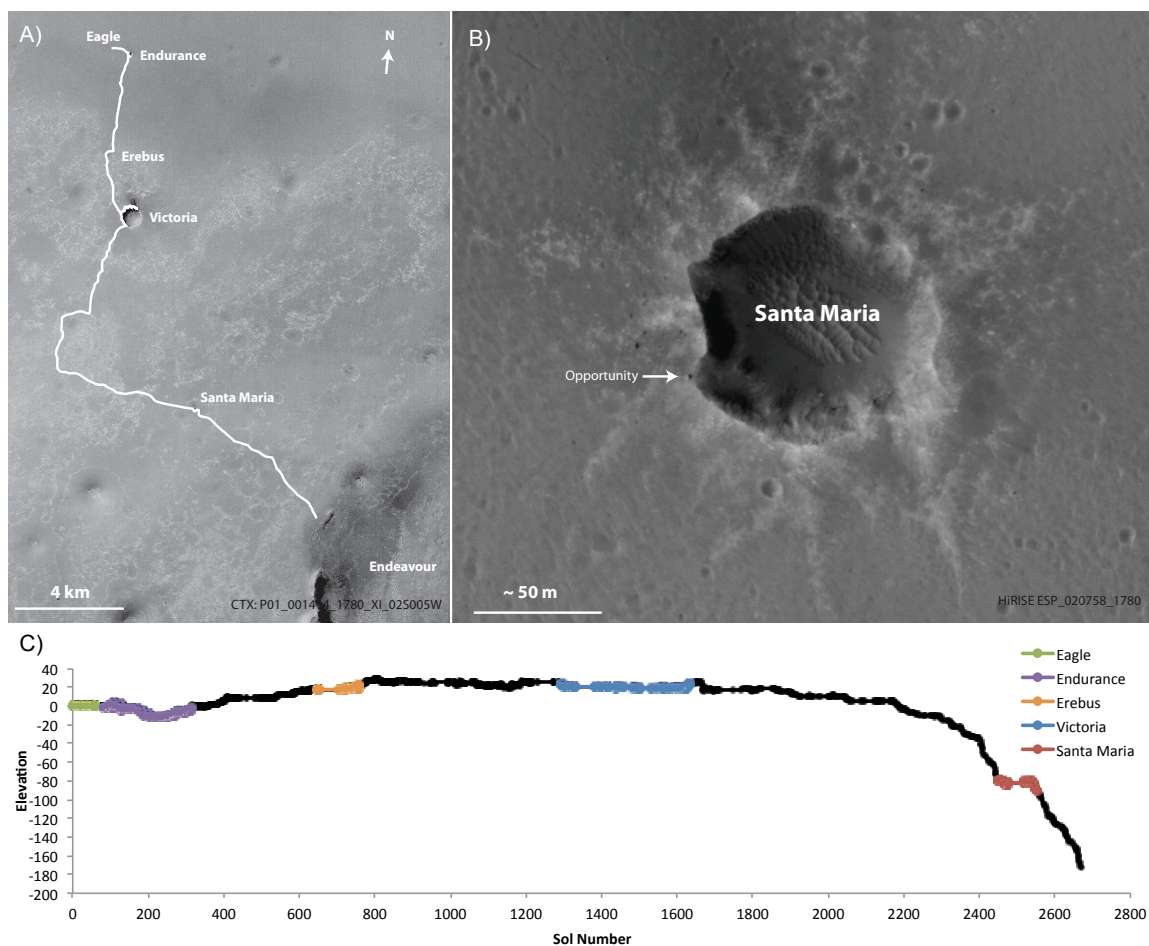


**Figure 3.1:** A) Rover traverse map as of Sol 2670 plotted on Context Imager (CTX) image P01\_001414\_1780\_XI\_02S005W. Santa Maria crater is located about 7 km southeast of Victoria crater. B) Santa Maria crater in HiRISE image ESP\_020758\_1780. The rover approached the crater on the western rim, and drove around the rim to the south, where it observed target Ruiz Garcia. C) Opportunity traverse elevation, extracted from HiRISE DTM. Significant campaigns at Eagle, Endurance, Erebus, Victoria and Santa Maria craters are plotted in color. The plains surrounding Santa Maria crater are approximately 100 m lower in elevation than those surrounding Victoria crater.

The *Opportunity* rover's Panoramic Camera (Pancam) and Microscopic Imager (MI) were used to distinguish sedimentary structures and textures. Pancam is a multispectral imaging system mounted on the rover's mast, 1.5 m above the ground. It consists of two cameras, each containing an eight-position filter wheel, allowing multispectral observations in the 400 to 1100 nm wavelength range (Bell et al. 2003). The MI acts as a "hand lens" camera and is mounted on the rover's "arm", known as the Instrument Deployment Device (IDD). To compensate for the variable topography of rock targets and limited depth-of-field, MI images are usually taken as a stack of images. The IDD moves along a path normal to the surface, and acquires images every few millimeters. MI images have a resolution of 30  $\mu\text{m}/\text{pixel}$  (Herkenhoff et al. 2003). The Alpha Particle X-Ray Spectrometer, also located on the rover's arm, provides bulk elemental characterization (APXS; Gellert et al., 2006).

### **3.3 Multispectral Observations**

Pancam multispectral images obtained during the Santa Maria campaign reveal several Santa Maria ejecta blocks with spectral behavior different from that observed in typical Meridiani outcrop, soils, or ejecta blocks at other craters. Specifically, ejecta blocks named Juan de la Cosa (Sol 2451), Sancho Ruiz (Sol 2452), Maestre Alonso (Sol 2452), Terreros (Sol 2479), Ruiz Garcia (Sol 2479), Mabuya (Sol 2523), and several other unnamed blocks imaged along the rim of Santa Maria exhibit higher reflectivities—from a few percent up to 25%—in the shortest wavelength Pancam filters (432, 482, and 535 nm). Several examples are shown in Figure 3.2. These anomalously "blue" materials represent a

relatively unusual Pancam spectral end-member among Meridiani materials (e.g., Squyres et al., 2006b, 2009; Farrand et al., 2007; Arvidson et al., 2011). Higher reflectivity in the blue compared to typical Meridiani materials is consistent with a lower ferric iron content and/or finer grain sizes within these materials (Gaffey et al., 1993; Bell et al., 1993)). None of these surfaces exhibit evidence of hydration based on long-wavelength Pancam data (Rice et al., 2010).

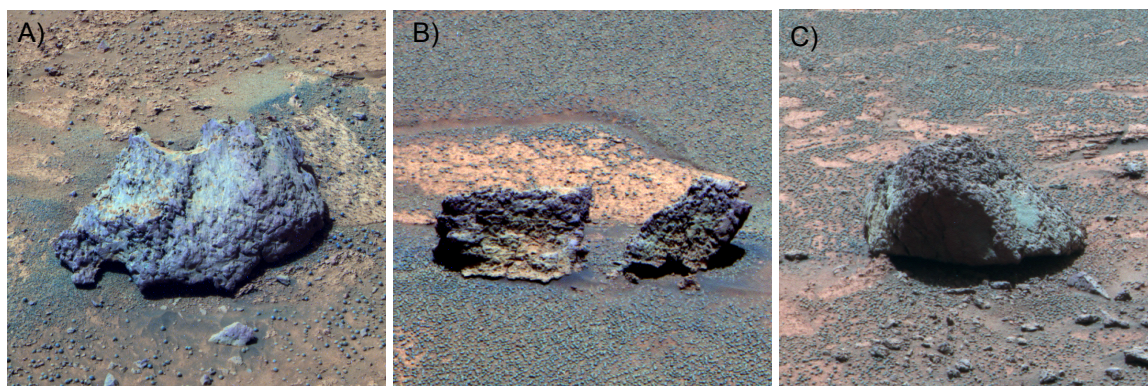


**Figure 3.2:** False color Pancam images of anomalously blue ejecta blocks at Santa Maria crater. A) Target Terreros, acquired on Sol 2479, using filters L257 (753, 535, 432 nm). B) Target Sancho Ruiz, acquired on Sol 2452, using filters L257 (753, 535, 432 nm). C) Target Maestre Alonso, acquired on Sol 2452, using filters L256 (753, 535, 482 nm).

### 3.4 Textural Observations

High-resolution (several mm/pixel) Pancam images of ejecta blocks acquired during the Santa Maria campaign also reveal sandstones with abundant mm-scale, parallel-sided lamination (Figure 3.3). These fine laminae, known as pinstripe lamination, may represent wind ripple stratification, or amalgamated grain flows, indicative of eolian deposition (Hunter 1977, Rubin and Hunter 1982, Fryberger and Schenk 1988). Blocks

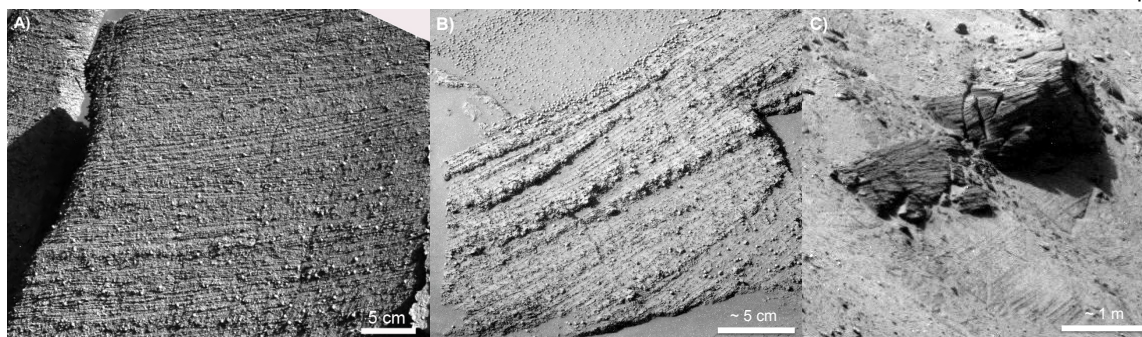


**Figure 3.3:** A) Typical eolian stratification of the Burns formation, seen here at the Tipuna outcrop, Endurance crater (Grotzinger et al. 2005). This image was acquired using Pancam's 432 nm filter on Sol 307. B) Sandstone ejecta block at Santa Maria Crater, with planar to low-angle cross-stratification and pinstripe lamination, indicative of eolian deposition. Note the similarities in scale and style of stratification compared to the Tipuna block in (A). This image also reveals abundant spherules, found within the block and as a lag deposit covering the surrounding loose sediment. This image was obtained using Pancam's 432 nm filter on Sol 2539. C) Pancam image of likely intact stratigraphy within Santa Maria crater. The image reveals multiple sets of cross-beds, consistent with an eolian depositional environment, and similar to rocks of the Burns formation (Grotzinger et al. 2005). The image was obtained using Pancam's 432 nm filter on Sol 2544.

also contain abundant spherules that are similar to those seen elsewhere in Meridiani and interpreted to be diagenetic concretions (*e.g.*, Squyres et al., 2004b). In general, rocks near Santa Maria are similar to the strata of the Burns formation studied elsewhere at Meridiani (*cf.*, Grotzinger et al. 2005).

However, the anomalously "blue" ejecta blocks exhibit a very different textural component that consists of massive, fine-grained, mottled, and/or nodular morphologies. One of the rocks with an unusual texture, named Ruiz Garcia (Figure 3.4), was selected for a more extensive IDD campaign of MI imaging and APXS characterization. MI images show that this rock appears more well-cemented, and lacks the pore spaces, vugs, and crystal molds that are typical of the Burns formation (*cf.*, McLennan et al., 2005). Ruiz Garcia contains abundant nodules that are well rounded and display morphologies that

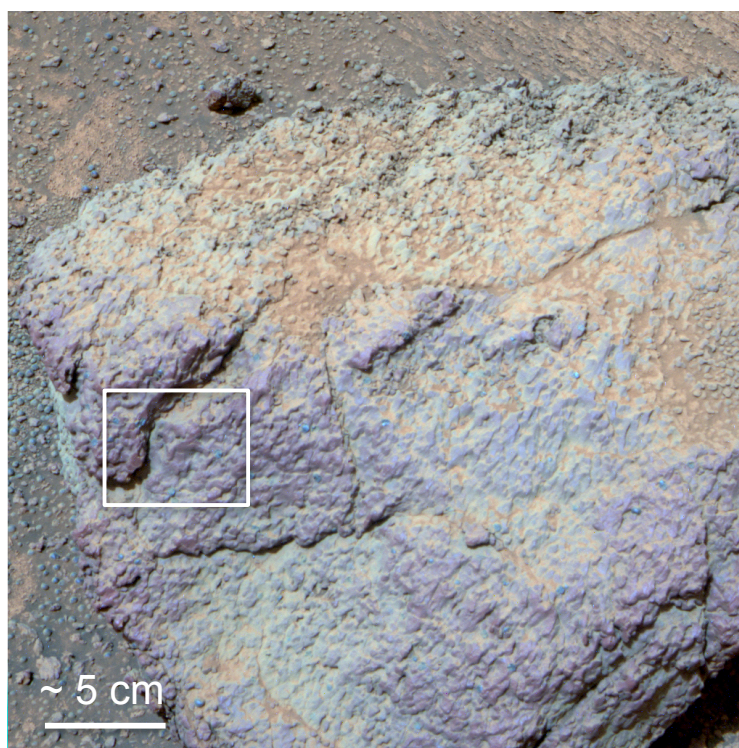


**Figure 3.4:** Target Ruiz Garcia. False color Pancam image using filters L257 (753, 535, 432 nm) acquired on Sol 2521. Ruiz Garcia is massive and has a nodular appearance. White box shows approximate location of MI mosaic in Figure 3.5.

generally range from ellipsoidal to more irregular shapes that show interlocking geometry (Figure 3.5). Figure 3.5a shows several concretions (gray tone) scattered amongst the more uniform nodular texture (reddish tone). Nodules in the fine-grained facies are typically 3 to 7 mm as measured along their long axis. Ruiz Garcia is pervasively overprinted by a nodular texture, and the nodules do not appear to have any preferred orientations.

MI images of Ruiz Garcia (Figure 3.5) reveal that the rocks have grain sizes smaller than those that can be resolved by the MI. The minimum grain size that can be resolved should be greater than the pixel dimensions (30  $\mu\text{m}$ ), and several pixels are required to resolve a grain, and so we accept the minimum resolution to be  $\sim 100 \mu\text{m}$  (Herkenhoff et

al., 2003). Since, by definition, muds are less than  $62.5\ \mu\text{m}$ , including sediments of chemical origin (Blatt, Middleton and Murray, 1980) mud sized grains cannot be resolved in MI images. Therefore, we infer that the rock is simply very fine-grained, and could potentially represent something fine enough to be considered a mudstone. These rocks are interpreted as the first sedimentary rocks observed by the rover at Meridiani Planum with grain sizes smaller than that of fine-grained sand. *Opportunity* did not make MI measurements on any other blocks of unusual spectral character, but Pancam images indicate that other anomalously blue Santa Maria ejecta block surfaces are also massive and likely very fine grained (Figure 3.2).

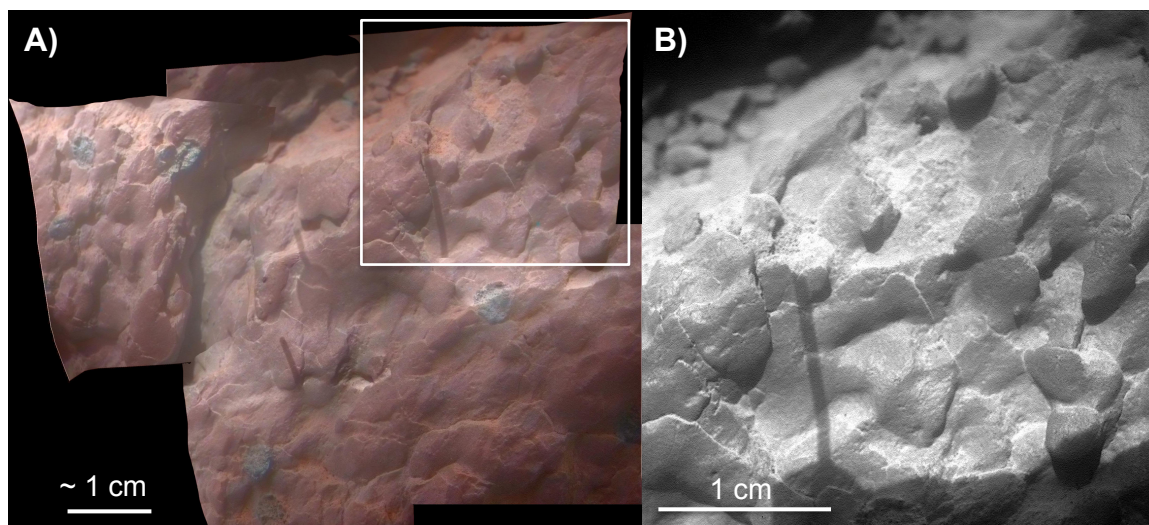


**Figure 3.5:** A) MI mosaic acquired on Sol 2527, colored with Pancam from Sol 2521, using filters L277 (753, 432, 432 nm). Individual grains cannot be resolved in MI images. Blue circular areas are hematite concretions, similar to those found elsewhere in Meridiani Planum. White box shows approximate location of MI frame shown in B). B) MI best focus frame acquired on Sol 2527. Note the nodular texture, very fine grain size, and lack of stratification.

### 3.5 Composition

APXS data provides additional insight and can be used to relate the Santa Maria facies to other outcrops at Meridiani Planum. The Burns formation is interpreted to represent a two-component mixture of a sulfate- and hematite-rich brine and a siliciclastic component with a composition consistent with acid-leached basalt (McLennan et al., 2005; Squyres et al., 2006b). At Endurance and Victoria Craters, these two components have been shown to have a depth dependent relationship, with stratigraphically lower samples enriched in the siliciclastic component, and stratigraphically higher samples enriched in materials precipitated from a sulfate- and hematite-rich brine (Squyres et al. 2006b; 2009). APXS compositional data indicate that the Santa Maria blocks are relatively enriched in the siliciclastic component (Figure 3.6), consistent with the low stratigraphic level of Santa Maria crater relative to Victoria and Endurance Craters (Squyres et al., 2009).

Some caution must be applied when relating the composition of the Ruiz Garcia analysis, which was collected on a rock that was not abraded by the Rock Abrasion Tool (RAT), to analyses collected on abraded rocks. Because such “as is” analyses may be variably contaminated with the ubiquitous basaltic soil and dust observed at Meridiani Planum, it is important to evaluate the effect of such contamination on a given APXS analysis. As shown on Figure 3.6, for “as-is” analyses there is a clear trend from the mixing array between siliciclastic and chemical components defined by the abraded rock analyses toward basaltic soils. Some basaltic soils are further modified by enrichment in hematite from eroded Burns formation outcrop, as demonstrated by Yen et al. (2005). Based on bulk chemistry alone, Ruiz Garcia compositions appear relatively unaffected by basaltic soil contamination. Interpretation of APXS data (Figure 3.6) is consistent with the

absence of observed soil or dust components on the outcrop (Figure 3.5). Accordingly, we suggest that the Ruiz Garcia analysis faithfully records the composition of the rock, unaffected by soil or dust contamination.

### **3.6 Diagenetic Considerations**

Despite the relative enrichment of siliciclastic-component in Santa Maria mudstones, the Ruiz Garcia analysis indicates that this lithology is still sulfate-rich (Ruiz Garcia  $\text{SO}_3 = 17.5 \text{ wt}\%$ ). This is significant because sulfate sediments are chemically labile, easily recrystallized, and grain sizes are often significantly increased beyond their original primary grain size as a result of diagenesis (McLennan et al., 2005). This increase in grain size is the product of Ostwald ripening of crystals, where recrystallization results in grain-size enlargement to thermodynamically more stable geometries (Lifshitz and Slyozov, 1961). Thus, the grain sizes ( $< \sim 100 \mu\text{m}$ ) observed in the unique rock surfaces of Santa Maria ejecta blocks are likely larger than the original, pre-diagenetic grain sizes of their precursor materials. In addition, the complete lack of physical stratification, so ubiquitous throughout the rest of the Burns formation and even in other facies at Santa Maria crater, argue that the grain size of these anomalous ejecta block materials is homogeneous and could indeed be significantly finer than  $\sim 100 \mu\text{m}$ . Sulfate mobility is an issue for all Meridiani rocks, and recrystallization is observed at Endurance, Erebus and Victoria craters (Grotzinger et al., 2005; Metz et al., 2009; Edgar et al., 2012). However, recrystallized rocks at these other locations still preserve primary stratification (Figure 3.7), and nodules are not observed. The massive, fine-grained, nodular blocks at Santa Maria crater are exceptional, and another hypothesis is warranted.

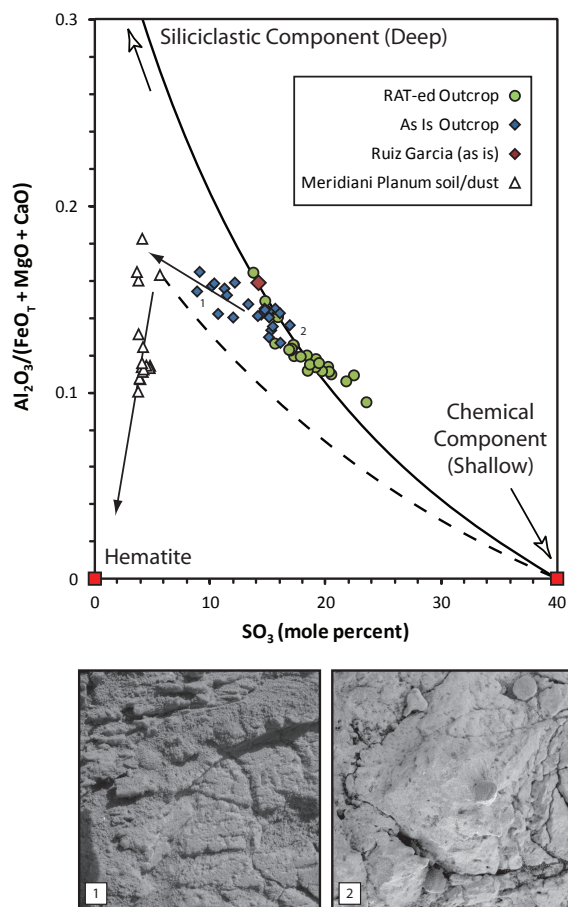


**Figure 3.6:** Molar  $\text{Al}_2\text{O}_3/(\text{FeO}_T + \text{MgO} + \text{CaO})$  versus  $\text{SO}_3$  (mole %) for Burns formation APXS analyses acquired between Sol 1 and 700 (Gellert and Rieder, 2006). Green circles are analyses acquired after abrasion of rock surfaces with the RAT, blue diamonds are analyses acquired on “as-is” outcrop (i.e., not abraded or brushed clean with the RAT). The red diamond is the as-is analysis on the target Ruiz Garcia acquired on Sol 2521. White squares are analyses of undisturbed soils and dust at the *Opportunity* landing site collected over Sols 1-700. The solid line is a mixing array reproduced from Squyres et al. (2006b) and tracks the varying proportions of siliciclastic and chemical components in abraded Burns formation samples. The dashed line is a mixing array between the chemical component of outcrop (Squyres et al., 2006b) and Martian dust, as represented by the analysis Hilltop\_Wilson (Yen et al., 2005), collected on Sol 123. Lines with small arrowheads track increasing levels of “contamination” of as-is outcrop analyses with basaltic soil, and the enrichment of some of those soils with hematite derived from eroded Burns formation outcrop. The numbers 1 and 2 correspond to the inset MI images of the most  $\text{SO}_3$ -poor and  $\text{SO}_3$ -rich as is APXS analyses: “Pohutu” and “Russett”, respectively. These images were collected on Sol 311 and 381, respectively, and show that the apparent trend away from the mixing array is consistent with variations in soil cover content. Each MI image is 3 cm wide.

We believe that these multiple lines of multispectral and textural evidence support the hypothesis that the unique, massive, fine-grained facies of Santa Maria ejecta blocks could have started out as a mudstone and has since been modified through diagenesis. An important component of this hypothesis is that these sediments could not have started out as the sandstones of the Burns formation, typically with medium to coarse grain sizes (see, for example, Grotzinger et al., 2005; 2006; Edgar et al., 2012); rather, they appear to represent a different initial grain size that was significantly finer.

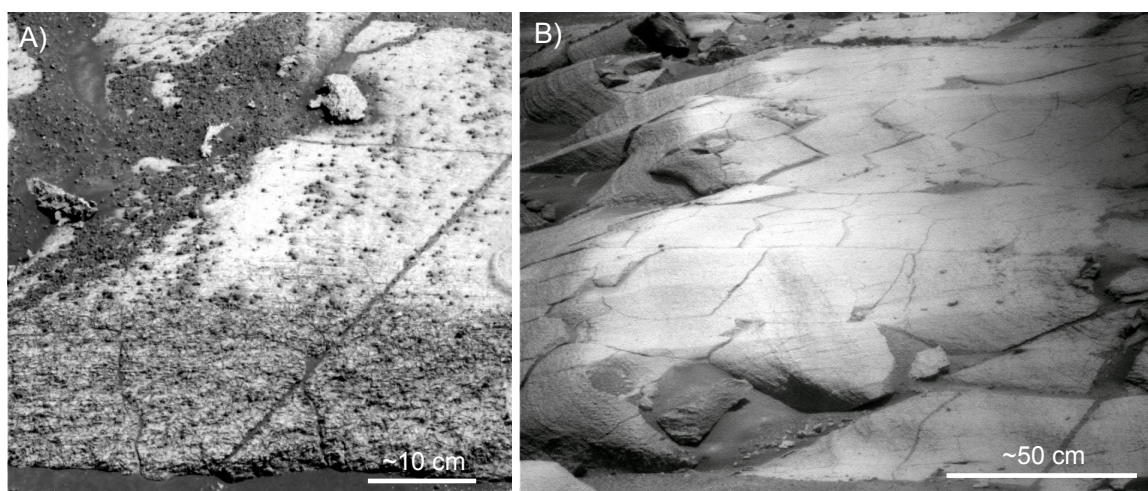


**Figure 3.7:** Recrystallization in the Burns formation seen at Endurance crater and Victoria crater. A) The Whatanga contact at Endurance crater is interpreted to have formed in the capillary fringe of the water table (Grotzinger et al. 2005). The dark-toned zone is heavily recrystallized, but palimpsest fine lamination is still visible. Image acquired on Sol 312, using Pancam's 753 nm filter. B) The light-toned Smith unit at Victoria crater is heavily recrystallized, but images taken at low solar incidence angles reveal fine lamination (Edgar et al. 2012). Image acquired on Sol 1351, using Pancam's 753 nm filter.

### 3.7 Interpretation of Nodular Texture

Ruiz Garcia and other fine-grained blocks have a nodular appearance, which we infer to result from differential cementation during diagenesis. Their ellipsoidal to irregular shapes strongly contrasts with the concretions that are present in other outcrops of the

Burns formation, which generally have strictly spherical shapes (McLennan et al., 2005; Edgar et al., 2012). Ruiz Garcia and other fine-grained rocks lack any visible porosity, in contrast to other Burns facies, and appear very well cemented.

Observations of coarser-grained, well-laminated sandstones in the Santa Maria region suggest that these also underwent differential cementation, as they uncommonly also have a nodular appearance (Figure 3.8). However, the coarser-grained facies retain original textures such as lamination. Formation of nodules is characteristic of chemical sediments and it is not uncommon to see fine-grained sediments with primary stratification undergo transformation to a more massive but mottled texture due to differential early cementation (Mohamad and Tucker 1976; Moller and Kvingan 1988; Lee and Kim 1992). Ruiz Garcia displays mottled textures that are very similar to nodular mudstones on Earth (Jenkyns 1974; Kennedy and Garrison 1975; Moller and Kvingan 1988). For example, in the Neoproterozoic Buah Formation of Oman one can trace cm-scale stratification laterally and vertically into zones of mottling with massive texture (Figure 3.9). The scale and fabric of this terrestrial analog (carbonate) is very similar to the fine-grained martian sediments (likely sulfate).

The formation of nodules can be explained by differential cementation related to early diagenesis. This requires interstitial pore fluids that are oversaturated with respect to the phases that precipitate the interstitial cements that form the nodules. Differential cementation results from heterogeneous nucleation, and differential weathering of the more resistant nodules (better cemented, harder rock) produces the modern surface topography of



**Figure 3.8:** The coarser-grained, well-laminated sandstone facies also exhibits a nodular appearance (arrow), due to differential cementation. However, the coarser-grained facies retains its original laminated texture. This image was acquired on Sol 2456, using Pancam's 753 nm filter.

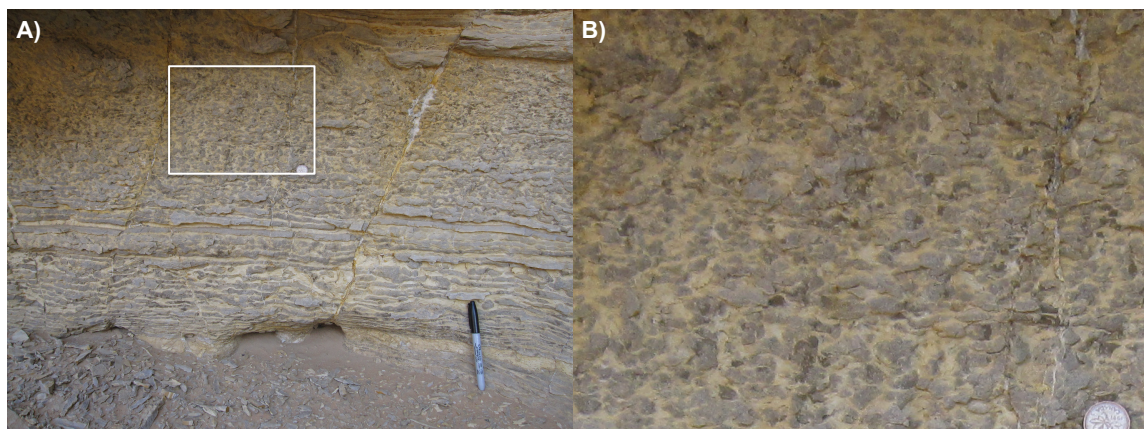


**Figure 3.9:** Diagenetic modification to a massive but mottled texture is common in fine-grained chemical (carbonate) sediments on Earth. This example from the Neoproterozoic Buah Formation of Oman shows a finely laminated texture (base of outcrop in image A) breaking up into nodules (image B). Image B exhibits a massive, fine-grained texture similar to target Ruiz Garcia.

the rock featuring its characteristic roughness that reflects the presence of the nodules (*cf.* Noble and Howells 1974; Kennedy and Garrison 1975, Moller and Kvingan 1988).

Unfortunately, the stratigraphic context of our hypothesized nodular mudstone facies at Santa Maria is poorly constrained. Pancam images of the crater walls indicate that the nodular, mottled texture is present in only the lower portion of the crater, but impact brecciation inhibits direct inference of stratigraphic position. The proposed mudstones are not observed in stratigraphic context, but we can still infer that they come from a lower stratigraphic level than the sandstones because preferential cementation to form nodules appears to have only affected the lower portion of the observed stratigraphy at Santa Maria crater (Figure 3.10).

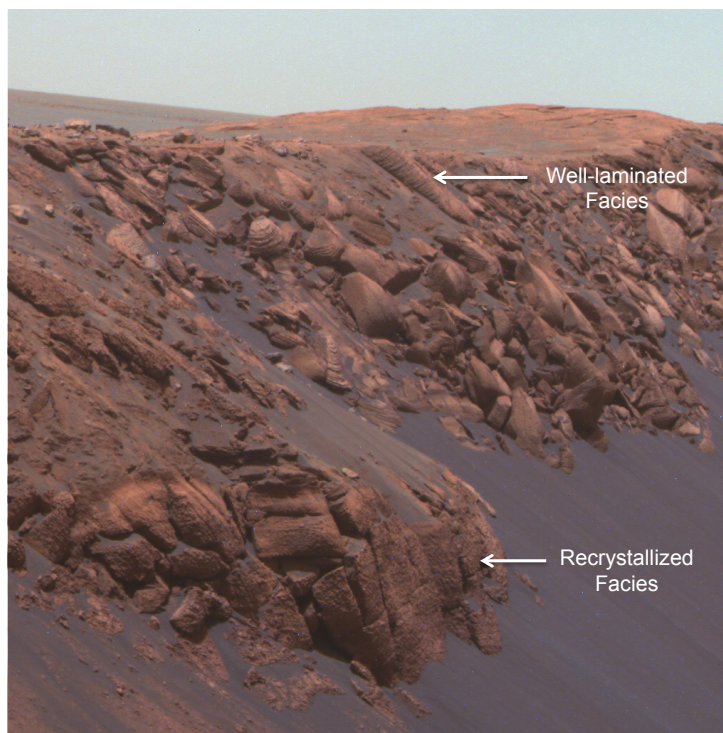


**Figure 3.10:** Stratigraphy exposed in the southern wall of Santa Maria crater. The lower portion of the stratigraphic section appears to be recrystallized, while the upper portion of the stratigraphy is well-laminated. Pancam false color image acquired on Sol 2454 using filters L257 (753, 535, 432 nm).

### 3.8 Identifying and Interpreting Mudstones on Mars

On Earth, fine-grained sedimentary rocks (grain size  $<62.5 \mu\text{m}$ ) are the most abundant sedimentary rock type (Potter, Maynard and Pryor, 1980). Mudstones occur in a variety of environments including marine environments, transitional environments such as deltas, rivers and estuaries, and nonmarine environments including lakes, floodplains, loess, and other eolian deposits (Potter, Maynard and Pryor, 1980). Fine-grained extrabasinal sediments – derived far from the site of deposition – are the record of extreme hydraulic segregation resulting from transport in currents of water or air. They accumulate in both local and terminal sediment sinks, and are most abundant at the distal end of sediment transport pathways. Fine-grained intrabasinal sediment of chemical origin, however, is produced at or near the site of deposition and their grain size reflects nucleation and growth kinetics rather than hydraulic processing (Bathurst, 1975).

Observations of the fine-grained facies at Santa Maria crater are very limited, so it is difficult to determine the environment in which they were deposited. Regional context provided by other outcrops of the Burns formation suggests it is unlikely that they were deposited in a marine environment. This is due principally to the absence of facies indicative of marine processes and, rather, the preponderance of evidence supportive of eolian processes (see, for example, Grotzinger et al. 2005 for further discussion).

Of the non-marine environments, we see no evidence for larger scale fluvial deposits in the Burns formation, such as channel deposits, coarse lags, or fining-upward sequences, which might support a hypothesis involving settling of fines on flood plains. Volcanic ash is a possible explanation for the fine-grained material, but we see no specific evidence of volcanism in the vicinity of Santa Maria crater besides the ubiquitous basaltic

sand that is found across all of Meridiani. Fine-grained material created during impact cratering is also a possible explanation. Fallout of suspended fine sediments from either the atmosphere (which may include pyroclastic or impact-generated fines) or from the water column of a lake may be the two most likely environments that would account for the fine grained, nodular rocks at Santa Maria crater.

Large accumulations of wind-blown dust and silt – sediments  $< 0.62 \mu\text{m}$  in grain size – are known as loess, and their cemented rock equivalents loessite (Smalley and Leach 1978; Johnson 1989; Chan 1999; Soreghan et al. 2002). On Earth, loess deposition is most commonly associated with Quaternary glaciation and wind reworking of glacial deposits (Edwards 1979). Smalley and Krinsley (1979) suggest that there are likely loess deposits on Mars. Loess deposition is proposed as a hypothesis for some of the young, widespread mantling deposits on Mars (Malin and Edgett 2000), including those within the Medusae Fossae Formation (Greeley and Guest, 1987; Scott and Tanaka 1986; Head and Kreslavsky 2004), in Arabia Terra (Fassett and Head 2007; Mangold et al. 2009; Lewis et al., 2008), Tharsis Montes (Bridges et al. 2010), and within the uppermost strata of the Gale crater mound (Anderson and Bell, 2010; Thomson et al., 2011). Recognition of the importance of these potential loess or dust deposits, which sometimes exhibit evidence for induration and form weakly cemented rock has led to the term “duststones” (Bridges and Muhs 2012). These duststones likely have global stratigraphic importance and may reflect the long-term decrease of impact-generated fines to be reworked by the wind and transported to sites of regional deposition (*e.g.*, Bridges and Muhs, 2012; Grotzinger and Milliken, 2012). Impacts, explosive volcanism and mechanical breakdown of material through saltation

provide alternatives to glaciation as mechanisms to produce abundant fine-grained sediment.

Large dust storms are common phenomena on Mars (Haberle 1986, Martin and Zurek 1993; McKim 1996). We can only estimate their magnitude in the geologic past, and the potential for rare, large storms to carry large volumes of sediment. It is possible that fine-grained facies at Santa Maria crater were formed during the fallout following dust storms that occurred at the time the Burns formation was being deposited. Although *Opportunity* did not observe what lies stratigraphically beneath the fines at Santa Maria crater, we can infer that it was likely eolian sandstone, because we see outcrops of eolian sandstones on the plains between Santa Maria crater and Endeavour crater at successively lower elevations. Fines deposited during global dust storms would have draped and mantled pre-existing topography. When wind velocities later increased (the coarser cross-bedded deposits of the Burns formation suggest persistent high wind velocities), much of the dust would have been removed, but perhaps some fraction remained in place to create the observed deposit. This potential “duststone” deposit would have mostly been preserved in an interdune depression as a lens of massive fine-grained material interfingering with eolian sandstones.

It is important to note that the APXS composition data for Ruiz Garcia are not consistent with the composition of modern martian dust (based on the analysis of Hilltop\_Wilson (Yen et al., 2005), collected on Sol 123). However, it is possible that the composition of ancient martian dust was different. For example, the dust may have had a larger tephra component, or a larger component of fines generated from impact processes,

resulting in a composition that falls on the siliciclastic to chemical mixing array rather than the mixing array between dust and the chemical component (Figure 3.6).

Alternatively, we consider a possible lacustrine origin for the fine-grained material. Lakes are sinks for both water and sediment (Leeder 1999). They form when runoff or river flow is interrupted, usually in a depression, or when groundwater emerges within interdune depressions or other playa lake settings. Lakes lack high current velocities, which provides a simple hydraulic setting in which fines can settle from suspension, making this an attractive interpretation for the Santa Maria fines. Previous work shows that interdune depressions would have been common on the ancient Meridiani plains (Grotzinger, 2005; Edgar et al., 2012). There are many types of lakes, ranging from large, deep, permanent freshwater lakes, to shallow, ephemeral, saline lakes, and they can be distinguished on the basis of facies associations and suites of sedimentary structures. We see no evidence in Meridiani for large, deep, permanent lake facies such as turbidites and varves, or associated adjacent fluvial facies that would have supplied a lacustrine setting with sediment, such as channels, alluvial fans, or deltas. Given the eolian environment that characterizes the Burns formation, this type of lake would have been unlikely. However, mudstones are found in terrestrial eolian environments in ephemeral saline lakes (Hanley and Steidtmann 1973; Mounney and Thompson 2002). Ephemeral saline lakes leave deposits of interstratified evaporites and extrabasinal clastic sediments, produced by cycles of storm runoff followed by evaporite precipitation (Leeder 1999). Chemically purer, more massive mudstones form when groundwater emerges, evaporates, and leaves its salts as mud-sized sediment particles. Lacustrine mudstones in eolian environments may additionally contain structures such as desiccation cracks, or coarser evaporite crystal

growth structures. Whereas possible desiccation cracks were observed in sandstones at Erebus crater (Grotzinger et al., 2006; Metz et al. 2009), we do not see these features in the proposed mudstones at Santa Maria crater. Instead, the fine-grained facies appears homogenous, with very low porosity, consistent with a pervasively cemented interdune chemical sediment, produced by in situ evaporation of emergent groundwater.

A key attribute of the Ruiz Garcia fine-grained facies is its nodular texture, and absence of visible pores, vugs, or crystal molds. On Earth, such a texture can indicate significant early diagenesis involving heterogenous lithification as discussed above. In addition to early lithification, the development of nodular textures may also be enhanced by differential compaction of less well-cemented components of the rock around the nodules during shallow burial (Wolf and Chilingarian 1976; Potter 1980). In the case of evaporites, nodules may reflect diagenetic phase changes from primary to secondary mineral assemblages, such as during the conversion of gypsum to anhydrite (Murray 1964). Either scenario could have occurred during diagenesis of lacustrine sediments. However, the absence of vugs, larger evaporite crystals, or crystal pseudomorphs suggests the sediment was precipitated as fine mud and experienced only enough diagenesis and recrystallization to form nodules, similar to the example of nodular carbonate mudstones (Figure 3.9). This would suggest precipitation from the water column, very rapidly and with many nucleation points to form abundant small crystals. The absence of bottom growth crystals, with an upward growth direction, would rule out persistence of the water body for a period of time long enough to form these crystals. In summary, we believe that the evidence from observations of the anomalous ejecta blocks at Santa Maria crater fits a simple model for a transient evaporitic lake that precipitated fine-grained sediments that were shallowly buried

and recrystallized to form nodular mudstones. Compared to Eagle and Endurance craters, this implies a body of standing water, as opposed to just flowing water; however, it need not have been long lived.

### **3.9 Significance of Duststones and Mudstones on Mars**

Although we are unable to distinguish potential duststones from lacustrine mudstones at Santa Maria crater due to limited data, the occurrence of this fine-grained facies still has important implications. Regardless of their origin, this is a new occurrence of such fine material at Meridiani Planum. It has been proposed that dust may comprise a much greater portion of the global stratigraphic record on Mars compared to Earth (Bridges and Muhs 2012; Grotzinger and Milliken 2012). Thus, if their origin is dust-related, the fine-grained material at Santa Maria crater may shed light on preservation mechanisms and how dust is incorporated in the stratigraphic record, and would provide another expression of persistently dry conditions that may have existed for much of the geologic history of Meridiani Planum.

Alternatively, if the fine-grained rocks represent lacustrine mudstones, this would support the inference that the Burns formation may record intermittently wet conditions (Squyres et al., 2004b), possibly involving interdune lacustrine environments (Grotzinger et al., 2005). This is especially important because it strengthens the conceptual model that invokes sulfate-rich, but “dirty” (i.e. silicate containing) playa lakes as a potential source of the Burns formation eolian sulfate sandstones. The sulfate-rich eolian sandstones that overlie the fine-grained sediments would signal a return to dry conditions at ancient Meridiani. Diagenetic alteration during shallow burial of the fine-grained sediments

created the nodular textures, and all sulfate sediments experienced the chemical interactions that resulted in ubiquitous precipitation of hematite concretions that overprint both nodular fine-grained sediments as well as coarser sandstones.

Finally, it is worth noting the special significance of the lacustrine hypothesis. Given that lakes of any type have high potential to preserve organic compounds, the Ruiz Garcia fine-grained sediments could represent not only a former potentially habitable environment, but one that also could have trapped and preserved organic matter if it had been present (*cf.* Farmer and DesMarais, 1999; Summons et al., 2011). The distinctive nodular texture represents a nice example of the different ways that diagenesis – so critical to preservation – may be expressed. Recognition of diverse facies or diagenetic textures does not in its own right guarantee success in exploring for organics (assuming organic compounds were present), but rather defines a basis by which exploration can proceed systematically, with emphasis on those rocks which may have undergone early lithification before organic compounds could have been degraded. Future missions, like the exploration of Gale crater by the Mars Science Laboratory rover *Curiosity*, might benefit from such an exploration approach.

*Chapter 4*

## LOW REGIME BEDFORMS IN PYROCLASTIC SURGE DEPOSITS, HUNT'S HOLE, NEW MEXICO

**Abstract**

Pyroclastic surges are dilute flows of gas and rock fragments, typically generated by the interaction of magma and water in phreatomagmatic eruptions. Due to the hazardous nature of these eruptions, very little is known about sediment transport during these events. However, the cross-stratified deposits that they leave behind provide a potentially important history of the flow conditions because all sedimentary bedforms directly record interactions between the flow and transported sediment particles. The goals of this study are to use geometric relationships within surge deposits to better understand bedform kinematics and gain insight into the flow dynamics of pyroclastic surges.

Two prime examples of pyroclastic surge deposits are exposed in Hunt's Hole and Kilbourne Hole in southern New Mexico. These Pleistocene volcanic craters expose up to 13 m of pyroclastic surge deposits, dominated by decimeter-to-meter-scale bedforms. The corrugated pattern of erosion around the rim of Hunt's Hole provides three-dimensional exposures at the scale of the bedforms, which enables observations of bedform geometries. We identify several distinct facies, and measure bedform characteristics in the cross-stratified facies. Previous studies at other locations have identified "chute and pool structures" and potential antidunes in pyroclastic surge deposits, indicating high Froude number flow conditions. However, all bedforms observed at Hunt's Hole are consistent with downstream migration of bedforms, under lower flow regime conditions.

This study brings a relatively new approach to bedform reconstructions, through the use of Terrestrial Laser Scanning (TLS) to study cross-stratification at Hunt's Hole. TLS technology is based on Light Detection and Ranging (LiDAR). The large grain size variations present in pyroclastic surge deposits make them an ideal target for TLS, because the intensity of the returned laser varies with target properties such as grain size, packing, and composition, thereby making individual beds visible in LiDAR data. LiDAR intensity values may serve as a proxy for grain size. Digital outcrop models are produced with millimeter-to-centimeter-scale resolution. In addition to LiDAR, we apply consumer-level software to create nearly accurate three-dimensional models from digital photography. The combination of these methods allows for visualization and mapping of geological surfaces in three dimensions, which in turn can be used for bedform reconstruction. We then make estimates of hydrodynamic conditions to approximate a range of flow depths and depositional velocities for the bedforms observed at Hunt's Hole, and make predictions for pyroclastic surges on Mars.

#### **4.1 Introduction**

Pyroclastic surges are dilute flows of gas and rock fragments, in which clasts are supported by turbulence of the fluid phase rather than collisional momentum transfer (Branney and Kokelaar, 2002). Pyroclastic surges are formed in phreatomagmatic eruptions, pyroclastic flows, and pyroclastic falls (Cas and Wright 1987). Pyroclastic surges formed by phreatomagmatic eruptions are considered to be cold and wet compared to those formed in pyroclastic flows and falls, which are relatively hot and dry. Phreatomagmatic eruptions can occur in a variety of environments, with any type of

magma. The diversity of phreatomagmatic environments and eruption styles testifies to the availability of near surface water on Earth (Brand 2008), which has application to Mars in the search for aqueous processes (Squyres et al. 2007). Here we focus on phreatomagmatic eruptions in which magma mixes with groundwater in the shallow subsurface, resulting in pyroclastic surges that produce cross-stratified deposits. These eruptions are very hazardous and nearly impossible to observe, but the deposits that they leave behind provide important records of flow conditions. Cross-stratification records the migration of bedforms, which in turn provide evidence for flow properties such as depth and velocity.

Bedforms in phreatomagmatic surge deposits were first described in detail in the 1970s. Schmincke et al. (1973) described possible chute and pool structures in the Laacher See area, and suggested that these sedimentary structures represent a hydraulic jump. Generally, they are regarded as antidunes (Fisher and Waters 1970; Waters and Fisher 1971; Crowe and Fisher 1973; Hoffer 1976; Wohletz and Sheridan 1979; Gencalioglu-Kuscu et al. 2007), evidenced by low dip angles of laminae, stoss side laminae that dip more steeply than lee side laminae, and crestlines that appear to move upstream, indicative of upper flow regime. A handful of studies suggest that bedforms in surge deposits represent low-regime conditions (Stuart and Brenner 1979; Sohn and Chough 1989; Lajoie et al. 1992). On rare occasions, bedforms that show evidence for both upstream and downstream migration directions have been noted (Cole 1991). Additional studies have made quantitative measurements of dune wavelengths, amplitudes, stoss and lee side angles, and grain size distributions in pyroclastic deposits (Walker 1971; Waters and Fisher 1971; Sheridan and Updike 1975; Walker 1984). More recently, experimental and

modeling work has been used to better understand flow dynamics in a variety of pyroclastic density currents (Wohletz and Sheridan 1983; Giordano and Dobran 1994; Scheu et al. 2008; Dufek et al. 2009). However, despite several decades of analysis, we still have a very limited understanding of bedform kinematics in this type of depositional environment, and how bedforms can be used to infer flow conditions. Understanding bedform kinematics is limited by the inability to observe bedform formation and migration in base surge flows, so we must rely on the deposits they leave behind. The properties of bedforms preserved in rock outcrops have been described, but bedforms have not been reproduced experimentally (in flume experiments using intermediate densities for example). Furthermore, most outcrops reveal only two-dimensional exposures of the bedforms, providing only one viewing geometry from which to reconstruct bedform kinematics.

The principal goal of this study is to use three-dimensional geometric relationships to better understand bedform kinematics and gain insight into the flow dynamics of pyroclastic surges. We do this through field work and a relatively new technique of Terrestrial Laser Scanning. In this chapter we present field observations of pyroclastic surge facies, focusing on the reconstruction and analysis of cross-bedded facies. This is used to reconstruct flow dynamics and compare to other pyroclastic surge localities, and discuss criteria for recognizing these deposits on Mars.

## **4.2 Geologic Context**

Two prime examples of pyroclastic surge deposits are exposed in Hunt's Hole and Kilbourne Hole, located about 20 miles southwest of Las Cruces, in southern New Mexico,

USA (Figure 4.1). An additional crater, known as Potrillo Maar, straddles the international border with Mexico to the south (Reeves and DeHon 1965). Collectively these features are known as the Afton craters. The Afton craters are Pleistocene volcanic craters formed during phreatomagmatic eruptions (this type of crater is also called a “maar”). Maars range in size from 60 to 8,000 m (Tilling 1985) and typically fill with water to form relatively shallow crater lakes. A small depression, named Phillip’s Hole, lies to the east of Hunt’s Hole, and may represent a buried maar (DeHon 1965).

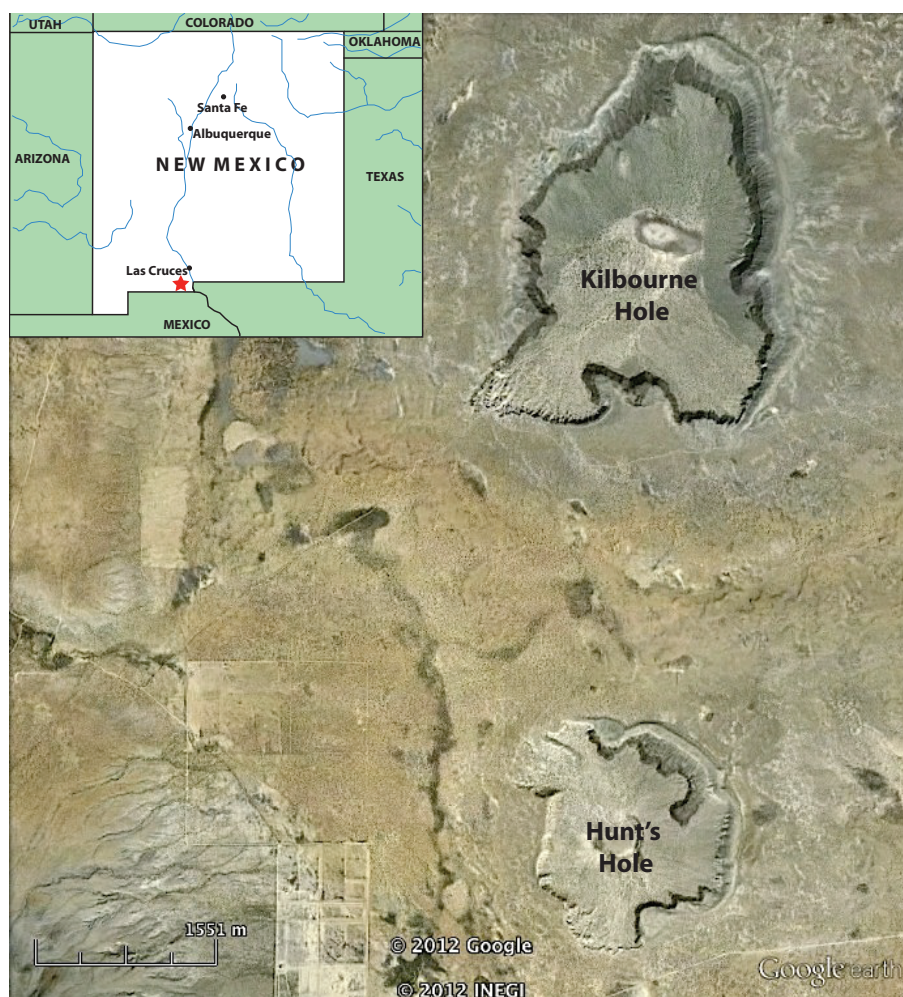


**Figure 4.1:** Field study area in southern New Mexico. Satellite image (available 11/26/2011) of Kilbourne Hole and Hunt’s Hole. Light-toned tuff rings are particularly visible on the eastern sides of the craters.

The Afton craters lie in the Mesilla Basin in the southern part of the Rio Grande rift, along the Fitzgerald-Robledo fault system (Hoffer 1976, Padovani and Reid 1989). Extension in this part of the Rio Grande rift began around 32 m.a. (Padovani and Reid 1989; McMillan 2004). As the Mesilla Basin subsided it filled with sediment eroded from the rift-flank highlands, and playa lake deposits. These basin fill deposits are known as the Santa Fe Group, and are estimated to be 457 to 762 m thick (Hawley 1984; Hawley and Lozinsky 1992). The youngest unit of the Santa Fe Group is the Camp Rice Formation, consisting of basin floor sediment and fluvial gravels, which are exposed in Hunt's Hole and Kilbourne Hole. Petrographic studies of the Santa Fe Group in the vicinity of Kilbourne Hole and Hunts Hole indicate that the underlying lithology is dominantly composed of monocrystalline quartz, plagioclase feldspar, and volcanic lithic fragments, with minor amounts of potassium feldspar and polycrystalline quartz (Hawley and Lozinsky 1992). The maars erupted through the Santa Fe Group and through thin basalt flows known as the Afton Basalt (Seager 1987). The Afton basalt has yielded K-Ar radiometric dates from 0.5 m.y. to about 0.1 m.y. (Seager et al. 1984; Hoffer, 1976; Hawley and Kottowski, 1969). Estimates of soil development (Gile 1987) suggest that the basalt is approximately 0.1 m.y. old. Surge deposits lie directly on the basalt, or where the basalt is absent, they rest on sediments of the Santa Fe Group (Camp Rice Formation) (Hoffer 1976).

Kilbourne hole is a roughly elliptical crater, approximately 3.4 km long and 2.4 km wide. Hunt's Hole is more circular with a diameter of approximately 1.7 km (2.0 km at its maximum width). The craters expose ~2 to 13 m of pyroclastic stratigraphy, dominated by decimeter-to-meter scale dunes (Figure 4.2). At Hunt's Hole, the geomorphic pattern

around the rim of the crater provides three-dimensional exposures at the scale of the bedforms, which allows for observations of bedform geometries. The most easily accessible outcrops and best exposures lie on the southern rim of the crater. Here, the contact between the pyroclastic surge deposits and the underlying Camp Rice Formation is effectively horizontal (very minor topographic variations are noted).

At both Kilbourne Hole and Hunt's Hole, the surge deposits show reworking into overlying eolian dune deposits. Eolian deposits are thick on the eastern rims of the craters, and enhance the modern day rim topography.



**Figure 4.2:** Outcrops at Hunt's Hole are dominated by decimeter-to-meter scale climbing dunes. Transport from left to right. The geomorphic pattern around the rim of the crater enables observations of bedform geometries in 3D. Note the large trough cross-bedding in flow perpendicular cuts, and high angles of climb in flow parallel cuts. Arrow points to basal contact with a paleosol of the Santa Fe Group.

### 4.3 Methods

To characterize the field site we measured stratigraphic sections, delineated facies, mapped the architecture of cross-stratified facies and reconstructed bedform geometries, mapped paleoflow directions, and collected samples for grain size analysis. We also employed a relatively new mapping technique using Terrestrial Laser Scanning (TLS), also known as LiDAR (Light Detection and Ranging), to study cross-stratification.

#### 4.3.1 Data Collection

LiDAR data was collected with an Optech ILRIS-3D imaging system. The ranging system uses a 1,500 nm wavelength laser, which bounces off the remote target and returns to the detector. The two-way travel time is divided in half and multiplied by the speed of light to calculate the distance to the target,  $Z$ .  $X$  and  $Y$  spatial positions are calculated from the position of the laser when it leaves the instrument. The Optech ILRIS-3D imaging system used in this study is capable of collecting 2,500 points per second. Each point records accurate  $X$ ,  $Y$ ,  $Z$  and intensity values. The intensity of the returned beam depends on many factors, including target properties (which may include grain size, composition and target reflectance (Kaasalainen et al. 2011)). While further calibration is required to understand these specific effects (Kaasalainen et al. 2009), individual beds, laminae, and likely even individual grains can be resolved at Hunt's Hole using LiDAR.

We collected LiDAR data from 8 locations around the southern rim of Hunt's Hole. Locations were scanned from multiple positions to account for 3D exposures and obstructions. These scans were then used to produce digital outcrop models with millimeter-to-centimeter-scale resolution (Bellian et al. 2005).

Grain size samples were processed using a Gilson sieve shaker. Samples were passed through a series of sieves corresponding to the following grain sizes in millimeters: >4, 4-2, 2-1, 1-0.5, 0.5-0.25, 0.25-1/8, 1/8-1/16, <1/16, and the sieve shaker was run for 15 minutes per sample.

#### *4.3.2 Data Processing*

LiDAR data were processed using LidarViewer version 2.5, a point cloud visualization tool developed by the Keck Center for Active Visualization in the Earth Sciences (KeckCAVES) and the Department of Geology at the University of California, Davis (Kreylos et al. 2008). LidarViewer provides an opportunity to view point cloud data without subsampling or reducing the data. The program also allows the user to extract individual points, fit planes to selected points, determine distances, and measure angles. These features were used for processing and analyzing LiDAR data from Hunt's Hole.

Additionally, commercial photogrammetry software was used to create 3D models from digital photography. 123D Catch (previously known as Project Photofly) is a cloud computing application developed by Autodesk Labs to create models of objects or space. Images taken from a series of locations surrounding a target (spaced approximately every 10°) are stitched together using photogrammetry to produce a 3D model. The quality of the model depends on the quality and spacing of the images. 3D models of rock outcrops at Hunt's Hole were produced with accuracies of approximately 1 to 3 cm. Resolution was verified by placing blocks of known dimensions and spacing within the target areas. The combination of these methods enables visualization and mapping of geologic surfaces in 3D.

#### 4.4 Pyroclastic Facies

Field observations of cross-stratified tuff reveal paleoflow directions radiating outward from the center of the crater, consistent with those measured by Hoffer and Hoffer (1998). Hunt's Hole exposes surge deposits that are ~2 to 13 m thick, with thicker exposures on the eastern rim (on the eastern rim, the basal contact dips ~10° into the crater, suggesting a greater topographic control on the deposition of pyroclastic material). We identify several distinct facies and measure bedform characteristics in the cross-stratified facies. Facies consist of a massive gray basal unit, cross-stratified tuff, planar-bedded tuff, lapilli-rich tuff, volcanic bombs, and capping unit, described below.

Grain size samples were also collected predominantly in the cross-stratified facies, in a vertical section through several sets of cross-beds (Figure 4.3). Due to the poorly lithified nature of the deposit, material could be acquired easily from selected regions using a spatula. While it was difficult to sample a single lamina, we collected material along several laminae of consistent grain sizes. The results indicate that the dominant grain size is fine to medium sand, though some samples show bimodal distributions. The bimodality could reflect the mixing of populations derived from volcanic sources in addition to the underlying Camp Rice Formation (Figure 4.4).

##### Massive Gray Basal Unit

*Description:* This unit consists of planar-laminated silt- to fine sand-sized sediment, and has a uniform thickness of 5 to 6 cm (regardless of the thickness of the full deposit). The unit contains a 1 mm lamina of dark basaltic medium-sized sand in the middle of the unit. The basal unit typically fractures along the dark sand laminae (Figure 4.5A). This

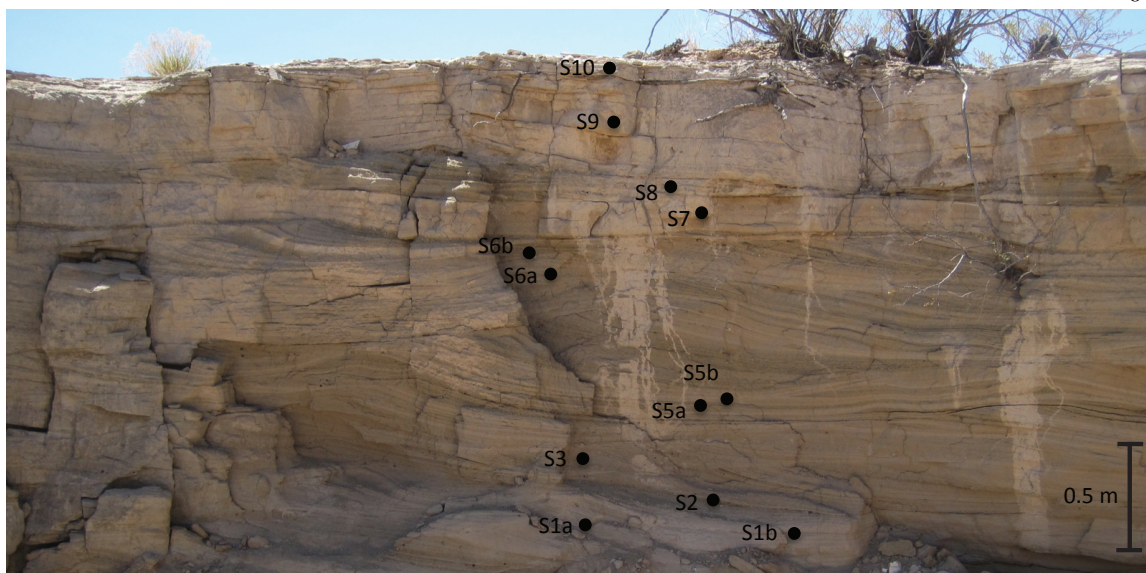


**Figure 4.3:** Rock outcrop at Hunt's Hole showing locations of grain size sampling. Several sets of dune cross-bedding are visible, indicating a paleoflow direction from left to right. Sample S7 was collected from an ash bed of approximately uniform thickness, mantling the underlying bedforms.

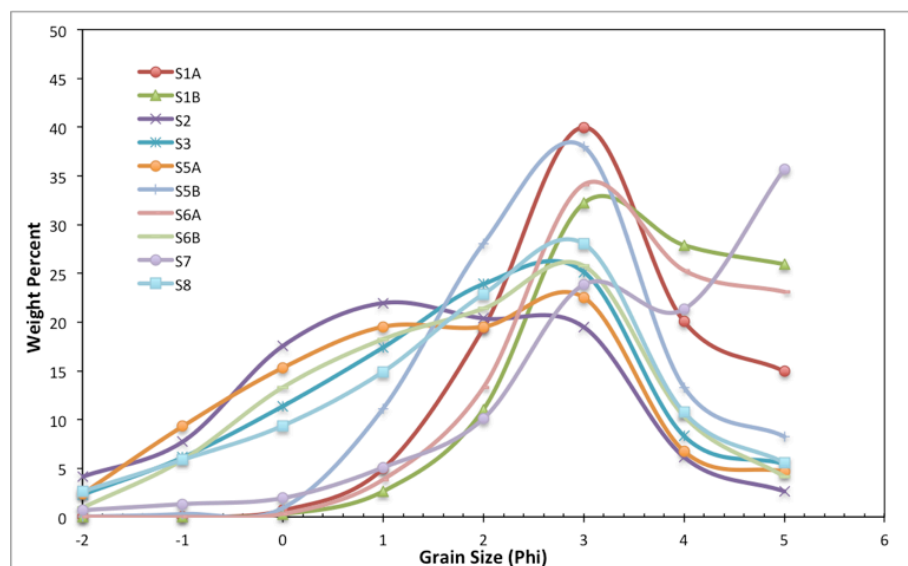


**Figure 4.4:** Grain size distributions corresponding to locations in Figure 4.3. The mean grain size is fine-to-medium grained sand, but several samples (S2, S5A, S7) show bimodal distributions.

facies lies stratigraphically on top of the paleosol at the top of the Camp Rice Formation, and is present in every observed outcrop at the contact between the surge deposit and the paleosol.

*Interpretation:* At Hunt's Hole, Hoffer (1976) describes this as "fine-grained even bedded air-fall layers underlying cross-bedded base surge deposits." However, at other locations, Sparks (1976) interprets similar facies as separating the flow unit from the ground surface, forming as a result of interaction of the flow with its boundary. The presence of planar lamination suggests this was a tractional stratified basal layer, rather than an air-fall deposit (though Branney and Kokelaar (2002) suggest that both cases are plausible depending on the behavior of the leading edge of the density current).

#### *Cross-Stratified Tuff*

*Description:* This facies is composed of fine-to-medium-grained, poorly to moderately-well sorted sand. Coarser beds composed of coarse-grained to pebble-sized grains also are present. The finer-grained portions of this facies are well laminated, whereas the coarser sections are more crudely stratified. Sometimes a fining upward trend is observed. This facies is characterized by trough cross-bedding (Figure 4.5B), often with stoss-side and bedform crest preservation; in these latter cases bedforms are ~2 m in wavelength on average and ~50 cm in amplitude (measured as the full thickness from the base to the crest of the bedform). Bedforms characteristically show evidence of climbing with gentle to moderate to steep angles of climb upsection in the outcrop; maximum climbing angles approach 50°. The dunes show migration in the down-current direction, flowing approximately radially outward from the center of the crater.

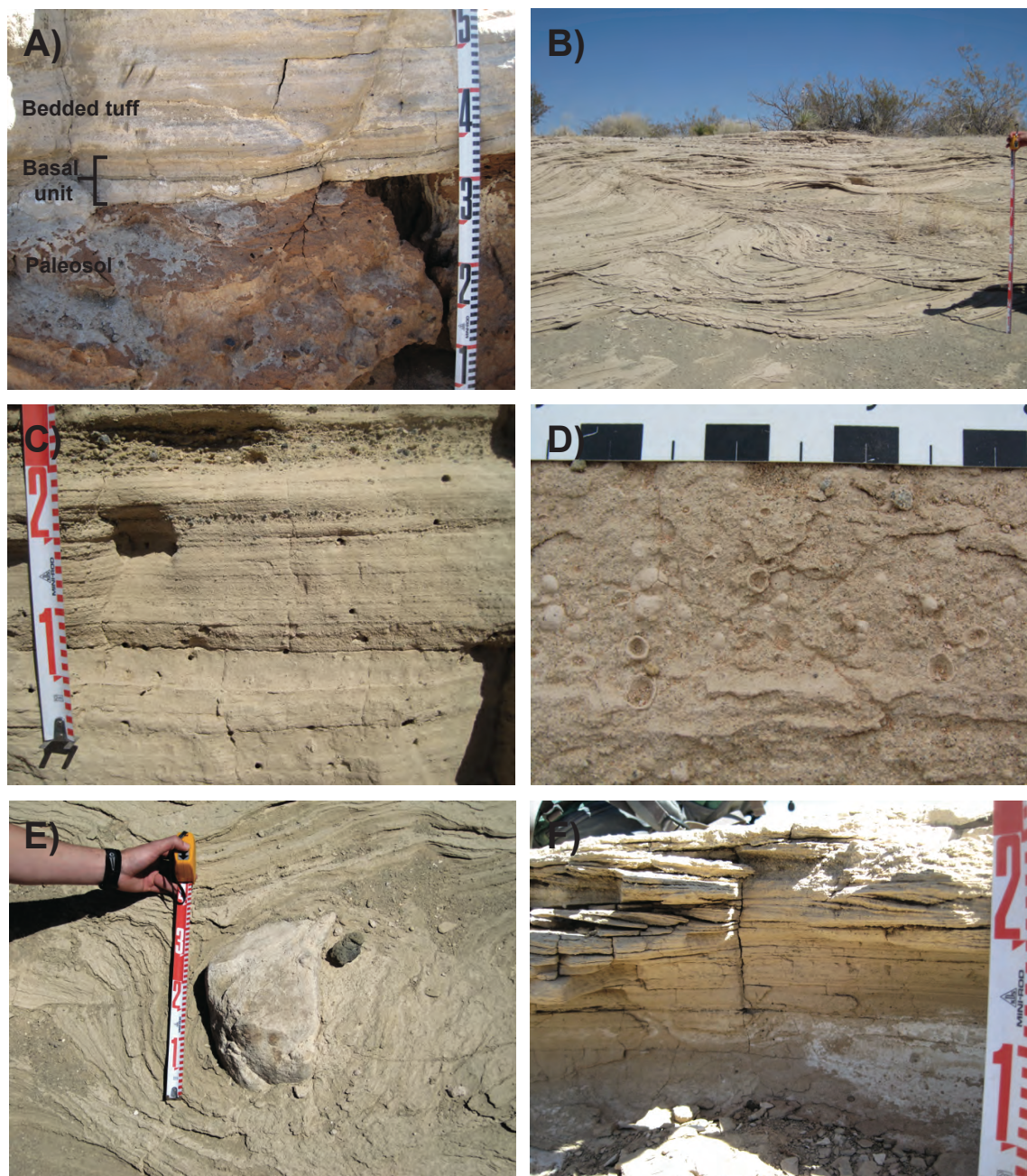


**Figure 4.5:** Facies identified in several measured sections at Hunt's Hole. See descriptions in text. A) Basal unit resting on red paleosol of the Camp Rice Formation. B) Large-scale trough cross-bedding. Paleoflow direction was approximately away from viewer. C) Planar bedding. Note the discontinuous trains of coarse material. D) Accretionary lapilli tuff. E) Bomb of sedimentary origin. F) Capping unit. Note the presence of small ripple-like bedforms, sometimes containing coarse sand. Paleoflow direction from left to right.

Cross-stratification is clearly visible in LiDAR scans (Figure 4.6), and the intensity of the return is correlated with grain size. Finer grain sizes produce higher intensities, while coarser material results in lower intensities (Figure 4.7). Although there are many factors that influence the intensity of the return, grain size appears to play a large role for this particular target material. The data suggest that LiDAR intensity distributions may serve as a proxy for grain size, which could be a very useful remote sensing tool.

*Interpretation:* Climbing dunes are common in pyroclastic surge deposits (Fisher and Waters, 1970; Crowe and Fisher, 1973; Stuart and Brenner 1979; Walker, 1984, Sohn and Chough, 1989). Trough cross-bedding indicates the migration of bedforms with sinuous crestlines. Details of the cross-bedding geometry and bedform reconstructions are discussed below, but these observations of bedforms at Hunt's Hole are consistent with low flow regime conditions.

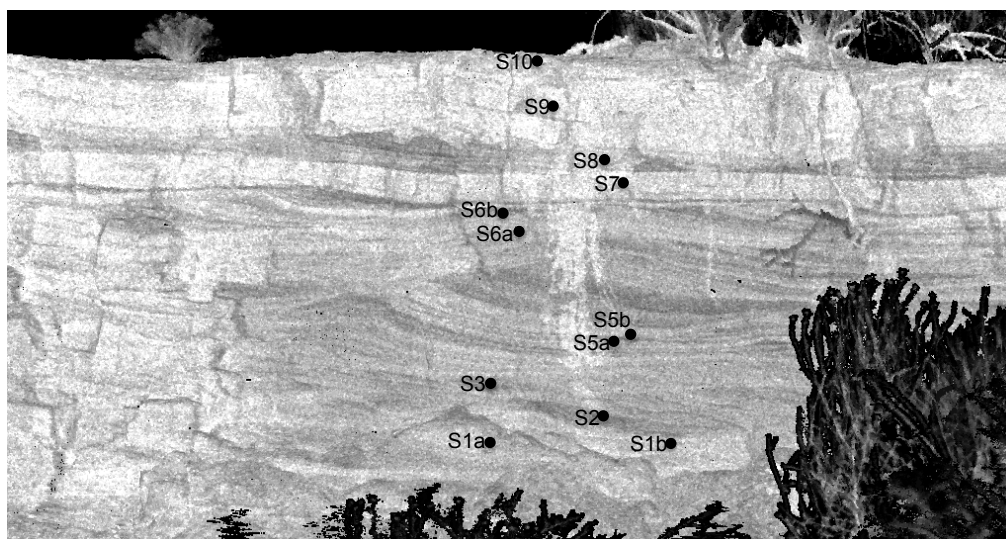


**Figure 4.6:** LiDAR scan corresponding to outcrop location in Figure 4.3 (taken at a further distance from the outcrop so a small shrub obscures part of the image). Cross-bedding is clearly visible in LiDAR data. Grain size sampling locations are plotted for comparison. Intensities reported in Figure 4.7.

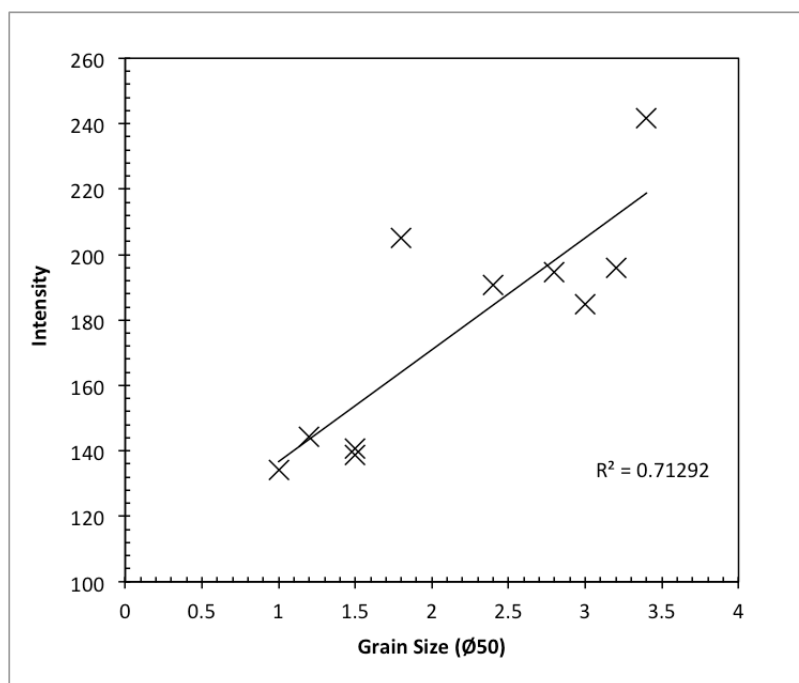


**Figure 4.7:** LiDAR intensity values versus grain size for each sampling site (grain size reported as fiftieth percentile,  $D_{50}$ ). Higher intensities generally correspond to finer grain sizes. Intensity scale ranges from 0 (black) to 255 (white).

### Planar-Bedded Tuff

*Description:* This facies consists of planar-bedded silt and very fine sand, supporting sparse coarse grains that range in size from very coarse sand to granules and pebbles. Sorting is poor. In general this facies is poorly bedded, though finer grained beds can be well stratified. This facies can be 20 cm to >3 m thick (Figure 4.5C).

*Interpretation:* This facies occasionally shows thickening and thinning over undulations, and is suggestive of traction transport. Grain size variations may result from segregation within the flow, or from some ballistic input. Discontinuous trains of coarse grains may be explained by rapid fall-out from suspension with subsequent traction transport (Sohn and Chough 1989).

### Lapilli-Rich Tuff

*Description:* Massive deposits of densely packed accretionary lapilli characterize this facies. Facies thickness ranges from 3 to 15 cm (Figure 4.5D). Lapillus diameters range in size from 2 to 6 mm, though most accretionary lapilli are around 5 to 6 mm. Some occurrences of this facies show broken and squashed lapilli in a matrix of silt-sized grains. The uppermost lapilli-rich tuff often contains root structures and burrows.

*Interpretation:* This facies likely represents air fall deposits of fine ash and accretionary lapilli. Accretionary lapilli represent the cooling and condensing of steam and water droplets to form concentric layers of moist ash around a central nucleus. Broken and squashed lapilli suggest that these grains were picked up and transported by the flow after falling.

### Volcanic Bombs

*Description:* Isolated large clasts are occasionally found within the other facies (Figure 4.5E). Most blocks occur within the cross-stratified tuff (probably because this is the most common lithology of the rock outcrops). They range in size from 2 to 10 cm and deform the underlying laminae. Bomb sags are often filled with coarse sediment, overlain by planar to cross-stratified tuff. Both basaltic and sedimentary bombs are present, often in the same locality. No distinct trends in the size or composition of bombs were observed upsection.

*Interpretation:* These clasts are interpreted as volcanic blocks that were ejected into the air during the eruption. Sedimentary bombs are well-cemented conglomerates inferred to be channel deposits from the underlying Camp Rice Formation. Basaltic bombs are inferred to come from the Afton Basalt.

### Capping Unit

*Description:* The top of the surge deposit is typically covered by a ~15 to 20 cm thick deposit of fine sand and silt, in depositional contact with the stratigraphically highest lapilli-rich tuff. These strata can be very well-laminated. Sparse, crudely stratified beds composed of coarse sand also are present. The upper 5 cm often contain sets of small-scale cross-bedding (~2 cm bedsets), with a low angle of climb, interpreted as ripples (but with grain sizes up to coarse sand) (Figure 4.5F).

*Interpretation:* This unit likely represents the final waning of the flow. Ripples and lower plane bed stratification indicate low flow regime conditions.

## **4.5 Analysis of Cross-Stratified Facies**

Facies similar to those described above have been identified and described by other authors in association with pyroclastic eruptions (*cf.* Branney and Kokelaar 2002). Here we focus on the reconstruction of bedform kinematics in the cross-stratified tuff, with implications for flow dynamics.

First, we recognize two scales of bedforms. The majority of the outcrop is composed of decimeter-to-meter scale climbing dunes. Dune bedforms range in height (measured from base to crest in outcrop exposures) from 25 to 80 cm, and in wavelength (crest to crest) from 190 to 460 cm. Following the methods of Crowe and Fisher (1973), dune heights are measured as the vertical distance between the crest and the base rather than the amplitude of individual laminae, because individual laminae usually cannot be traced from crest to trough. We also note the presence of smaller scale superimposed bedforms with decimeter scale wavelengths and amplitudes of ~5 cm (Figure 4.8). These

superimposed bedforms appear to migrate downcurrent or obliquely, relative to the larger dune stratification. In both scales of bedforms, submillimeter to subcentimeter-scale stratification is defined by sharp changes in grain size and density.

The grain size of the cross-stratified tuff is typically fine-to-medium-grained sand, but coarser beds (coarse-grained sand up to pebble-sized material) are present. As a whole, the grain size sorting varies from moderately to poorly sorted. Individual laminae have relatively uniform grain sizes, but grain size varies greatly from lamina to lamina. For example, one or two fine-grained laminae might be overlain by a lamina of coarse sand or even granules, that in turn is overlain by a lamina composed of fine sand. Notably, the character of the bedforms does not seem to correlate with grain size, and bedforms build



**Figure 4.8:** Small dunes superimposed on larger trough cross-bedded dunes. Small dunes indicate migration from right to left, while the larger dune stratification indicates transport into the page and to the left.

and evolve with whatever grain size is available. Furthermore, despite the occurrence of some laminae that have good sorting, fines are invariably co-deposited with coarse material.

Next we consider the geometry of cross-bedding. Outcrops on the southern rim of Hunt's Hole enable observations of bedforms in cross sections parallel to flow, transverse to flow, as well as in plan view. In flow-transverse cross-sections the occurrence of trough cross-bedding demonstrates that these bedforms are "three dimensional" indicating that they have crestlines with sinuous traces. Three-dimensional bedforms differ from two-dimensional bedforms in that they do not have straight crestlines, constant crest and trough elevations, or identical across-crest profiles at all locations along the crestline. Three-dimensional bedforms may have sinuous crestlines, sinuous troughs or across-crest profiles that vary along the crestline (*cf.* Rubin 1987). These variations result in cross-bedding in which the strike of cross-beds varies within a set (Rubin 1987), as seen at Hunt's Hole.

In flow parallel cross-sections, bedforms tend to build up from fairly planar surfaces, and terminate in erosional bounding surfaces generated by the migration of subsequent bedforms, or by draping and leveling of topography by airfall deposits (like the lapilli-rich airfall tuff). Measured in flow-parallel sections, stoss slope angles range from  $4^{\circ}$  to  $16^{\circ}$ , and lee slope angles from  $2^{\circ}$  to  $20^{\circ}$ . Other authors have made a case for antidunes based on stoss side laminae that dip more steeply than lee side laminae (*cf.* Fisher and Waters 1970). At Hunt's Hole, angles of lee-side laminae are generally higher than angles of stoss-side laminae (Figure 4.9), consistent with downstream migration.

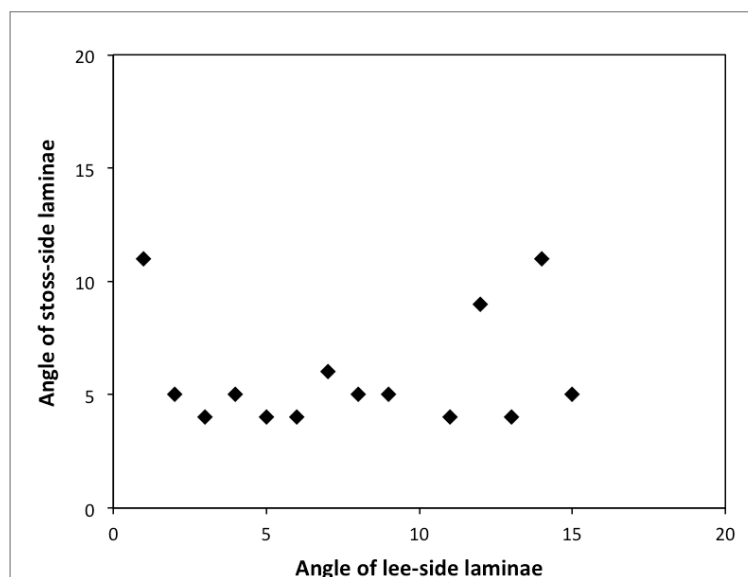


**Figure 4.9:** Angles of stoss and lee side laminae measured at Hunt's Hole. Lee-side laminae are generally steeper than stoss-side laminae.

It is interesting to note that angles of lee slopes are typically below the angle of repose. In modern eolian environments, dune foresets formed by avalanching dip at  $30^{\circ}$  to  $35^{\circ}$  in dry sand and up to  $42^{\circ}$  in moist cohesive sand (Bigarella et al. 1969; McKee and Bigarella, 1972), and in fluvial environments dune foresets are typically near the angle of repose (Kostaschuk, 2000; Carling et al 2000; Guy et al. 1966). Yet foresets formed by grainfall and ripple migration are necessarily below the angle of repose (Kocurek and Dott 1981). At Hunt's Hole, the abundance of lee slopes less than the angle of repose may suggest that grains were not deposited as much by avalanching as by other mechanisms, such as sediment falling out of suspension.

One distinguishing feature is that the bedforms have very high angles of climb (approaching  $50^{\circ}$ ). Tracing the angles of climb through the development of a bedform reveals that angles are initially high, then remain fairly constant as the bedform migrates

downstream without increasing in height, and then climb steeply (Figure 4.10). Variations in climb angle (steepening, flattening, steepening) are seen in other bedforms, including those that are overlain by another set of bedforms. This may reflect changes in rates of migration, or changes in sediment supply, which may be related to pulses in the flow.

In some places erosion of the capping unit has produced plan view exposures of the bedforms. Plan view exposures of large climbing dunes show “rib and furrow” stratification, again supporting the interpretation of the bedforms as having two directions of crestline sinuosity.

Cross-bedding geometry can then be used to reconstruct the morphology and behavior of bedforms. Large-scale trough cross-bedding at Hunt’s Hole was produced by the migration of three-dimensional transverse bedforms. Trough cross-bedding is created by the migration of depressions in dune troughs – the leading edge of the depression scours a trough-shaped bounding surface and the trailing edge deposits cross-beds (Rubin 1987). Plan view observations are also consistent with sinuous transverse bedforms, resulting in concave stratification in the down current direction. Near the top of the section, stratification becomes more planar, indicative of 2D and planar laminae. This is confirmed by LiDAR data. Using the plane-fitting tool in LidarViewer, we selected points along bedding surfaces and tried to fit them to a plane. The results indicate that bedforms that are lower in the stratigraphy are three-dimensional (evidenced by poor planar fits), but transition upwards into 2D and planar laminae (well fit by a plane). This is consistent with a decelerating flow, transitioning from 3D dunes to 2D and planar bedding (Southard and Boguchwal 1990).

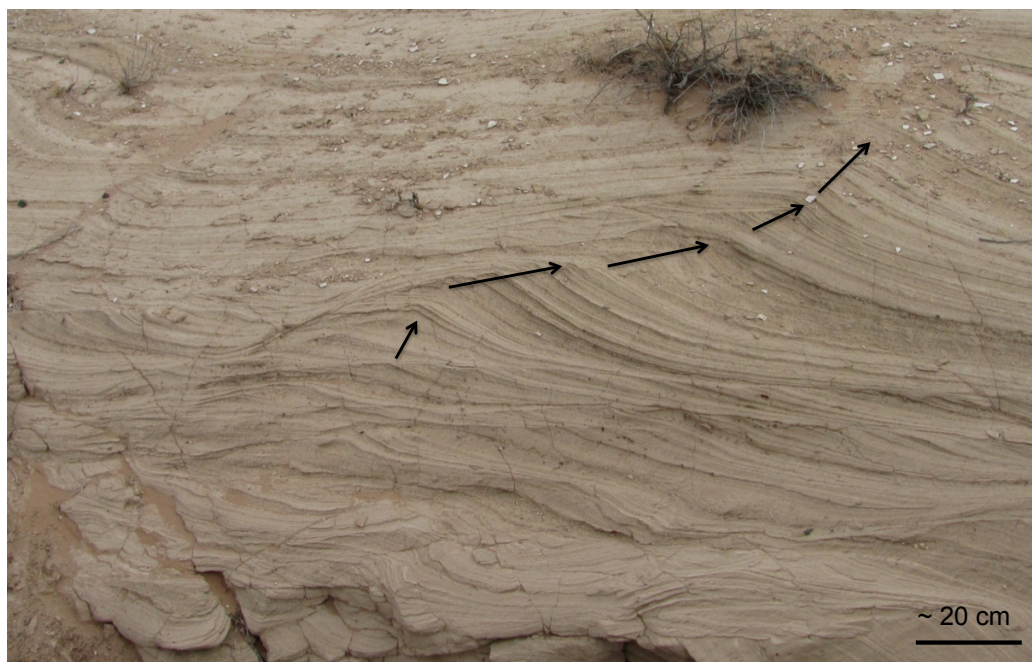


**Figure 4.10:** Climbing dune with variable angles of climb, indicated by arrows. Image is taken looking down on a sloped outcrop; angles represent apparent dips. Paleoflow direction approximately from left to right.

Unlike other depositional environments in which sets of cross-stratification characteristically record only a fraction of the original dune height (e.g. fluvial, Paola and Borgman 1991; eolian, Mountney et al. 1999), here the scale of the bedforms may not have been much greater than the preserved height of the dune stratification, because in some places entire bedforms are preserved (as evidenced by stoss-side accretion and even crest preservation). Stoss-side preservation (and draping of dune topography by lapilli tuff, for example) is indicative of high rates of aggradation relative to the rate of migration. This is also evidenced by the high angles of climb.

Bedforms also show evidence for merging – occasionally an up current bedform overtakes a down current bedform, resulting in a truncation surface (separating two dunes) that passes into a foreset (of one combined dune) in the down current direction. Bedforms

consistently migrate in the downstream direction (with the exception of a few superimposed bedforms that migrate obliquely).

The picture that emerges is one of meter-scale climbing dunes with sinuous crestlines migrating in the down current direction. Smaller, decimeter-scale bedforms were superimposed on the larger bedforms. High rates of deposition, resulting in high angles of climb, may be attributed to large fluxes of sediment entering the flow (replenishing the flow), perhaps as pulses. Considered as a whole, the deposit records decreasing flow velocities. In vertical succession, this results in bedforms that pass upwards from truncation to draping (Figure 4.11), decreasing bulk grain size, more abundant lapilli, and the appearance of small ripple-like bedforms. Figure 4.12 is a schematic diagram showing these trends in flow-parallel and flow-perpendicular cross-sections.



**Figure 4.11:** Vertical succession through a flow-parallel outcrop face. Truncated sets of bedforms pass upwards into draping and planar laminae. Paleoflow direction from left to right. Thick lines indicate major bounding surfaces.

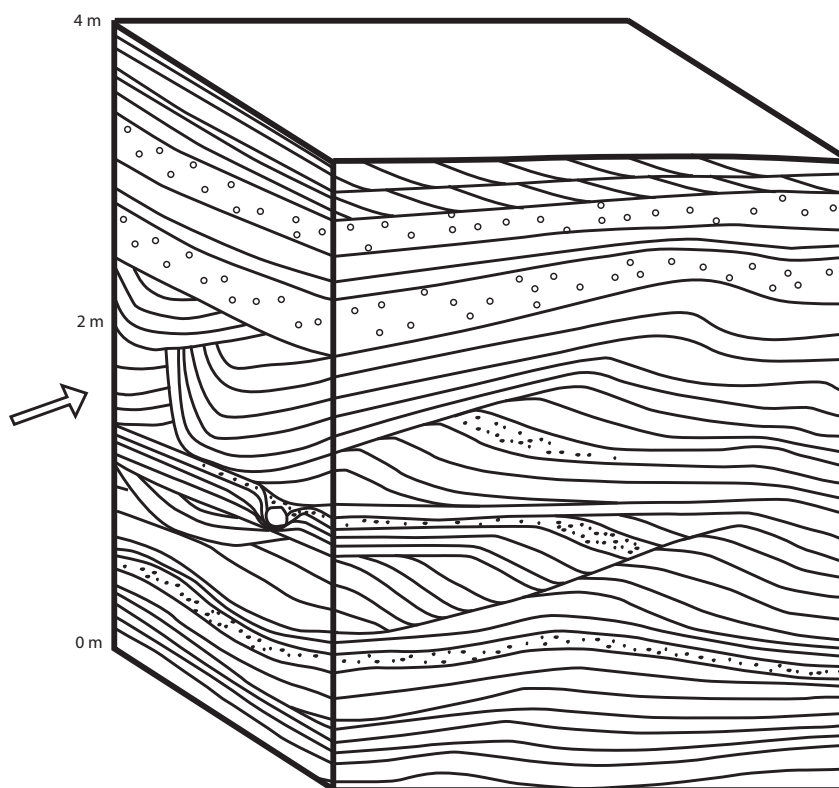


**Figure 4.12:** Schematic block diagram of a typical dune sequence on the southern rim of Hunt's Hole. Thicker stratigraphic sections are found on the eastern rim of the crater, but do not provide good 3D exposures for viewing bedforms. In this schematic block diagram (arrow indicates flow direction into the page and to the right), the flow perpendicular cross-section reveals trough cross-bedding. The flow parallel cross-section shows evidence for large climbing dunes. In vertical succession, grain size tends to decrease (lenses of coarse material become less common), bedforms pass from truncated sets to draping, accretionary lapilli become more abundant (represented by open circles), and small ripple-like bedforms appear at the top of the section.

#### 4.6 Flow Dynamic Reconstruction

The formation of bedforms in pyroclastic surge deposits cannot be observed in nature, and bedforms in surge-like flows have not yet been reproduced in the laboratory, so there are many uncertainties regarding the properties of the flow. However, from observations of grain size, bedform geometries and inferred bedform kinematics, we

believe that we can make reasonable estimates of the flow depths capable of producing the dunes, and the corresponding flow velocities. These estimates are based on the flow strength (or intensity of sediment transport) and the Froude number.

The flow strength can be represented by the dimensionless Shield's number:

$$\tau_* = \frac{\tau_b}{(\rho_s - \rho_f)gD} \quad (1)$$

where  $\tau_*$  is the dimensionless Shields parameter,  $\tau_b$  is the shear stress at the bed,  $\rho_s$  is the density of the sediment,  $\rho_f$  is the density of the fluid,  $g$  is the acceleration due to gravity, and  $D$  is the mean particle diameter. For  $\tau_*$  greater than 1, sediment is deposited as planar-laminated beds in the upper flow regime. Dunes are found when  $0.03 < \tau_* < 1$ . Although we do not see evidence for upper flow regime conditions at Hunt's Hole, other authors have described possible antidunes and upper plane bed in other pyroclastic surge localities. All of our observations are consistent with low flow regime conditions, but for the following calculations we assume that the bedforms were likely near the transition from dunes to upper plane bed, and so we assume that  $\tau_* \sim 1$ .  $\tau_b$  can be written as:

$$\tau_b = \rho_f C_f u^2 \quad (2)$$

where  $C_f$  is the friction coefficient, which incorporates bed friction and friction entrained from the surrounding atmosphere, with typical values around  $10^{-3}$  to  $10^{-2}$  (Parker et al. 1987), and  $u$  is the mean flow velocity. Density flows can also be described by the densimetric Froude number ( $Fr_d$ ) (the ratio of inertial to gravitational forces). When  $Fr_d$  is greater than 1, the flow velocity exceeds the wave velocity and the flow is said to be supercritical, or upper flow regime. When  $Fr_d$  is less than 1, the flow is subcritical

(tranquil) and lower flow regime. At  $Fr_d = 1$ , the flow is critical. We assume that the front of a pyroclastic surge can be represented by  $Fr = 1$  (the front of a dense surge moving through air can be thought of as a hydraulic jump from supercritical to subcritical conditions). The densimetric Froude number ( $Fr_d$ ) can be written as:

$$Fr_d^2 = \frac{u^2}{\left(\frac{\rho_f - \rho_a}{\rho_f}\right)gh} \quad (3)$$

Where  $u$  is the mean flow velocity,  $\rho_a$  is the density of ambient fluid (in this case air), and  $h$  is the flow depth. Rearranging equations (1) and (2), and solving for the flow depth:

$$h = \frac{\tau_* D}{Fr_d^2 C_f} \left(\frac{\rho_s - \rho_f}{\rho_f}\right) \left(\frac{\rho_f - \rho_a}{\rho_f}\right) \quad (4)$$

We assume  $\tau_* \sim 1$  based on the presence of dunes, and  $Fr_d \sim 1$  for a pyroclastic surge. Values for  $D$  come from grain size analysis, which reveals that the dominant grain size is fine to medium sand, so  $D \sim 1.25$  to  $2 \times 10^{-4}$  m. We estimate  $\rho_s$  as  $2700 \text{ kg/m}^3$  (a compromise between the density of quartz and feldspar of  $\sim 2.55$  to  $2.76 \text{ kg/m}^3$  and the density of basalt  $2800 \text{ kg/m}^3$ ), and  $\rho_a = 1.2 \text{ kg/m}^3$  (the density of air at  $20^\circ\text{C}$ ). By definition  $\rho_f$  is:

$$\begin{aligned} \rho_f &= (1 - C)\rho_g + C\rho_s \\ &= \rho_g + C(\rho_s - \rho_g) \\ \rho_s &\gg \rho_g \\ \rho_f &\approx \rho_g + C\rho_s \end{aligned}$$

where  $C$  is the concentration of sediment and  $\rho_g$  is the density of gas. We estimate that the majority of the gas is water vapor, formed when magma came in contact with ground

water, creating a steam explosion. At the boiling point of water (100°C), the gas (water vapor) would have a density of 0.946 kg/m<sup>3</sup>. The upper bound for the concentration of sediment in a turbulent fluid with traction transport is  $C \approx 0.1$  (but may be as low as 0.03) (*cf.* Valentine and Fisher 2000; Dade and Huppert). With these values, we find that the density of the fluid is:

$$\rho_{fmax} \approx 270 \text{ kg/m}^3$$

$$\rho_{fmin} \approx 27 \text{ kg/m}^3$$

These values of  $\rho_f$  can be used in equation (3) to solve for flow depth.

$$h_{max} = 18.92 \text{ m}$$

$$h_{min} = 0.11 \text{ m}$$

The minimum value for  $h$  seems unlikely given the height of the dunes that we measured, but we will briefly consider it here. Based on the range of values for  $h$ , we can solve for the depositional velocity:

$$u = Fr_d \left( gh \left( \frac{\rho_f}{\rho_f - \rho_a} \right) \right)^{\frac{1}{2}} \quad (5)$$

$$u_{max} = 14 \text{ m/s}$$

$$u_{min} = 1 \text{ m/s}$$

This range of velocities is on the very low end of the range predicted by other methods, which estimate velocities on the order of ~14 to 111 m/s (Sparks 1976); 20 to 110 m/s (Brand 2008); 12.5 m/s (Belousov and Belousova, 2001).

These depths and velocities likely correspond to just the basal portion of the flow.

Pyroclastic surges are thought to be density stratified as a consequence of their multiphase, turbulent nature (Valentine and Fisher 2000; Branney and Kokelaar 2002). The deposits left by pyroclastic surges record how the processes and conditions around a current's basal flow boundary varied with time (but they do not record the vertical structure of the current) (Branney and Kokelaar 2002).

#### **4.7 Comparison with Other Phreatomagmatic Surge Deposits**

Other authors have reported wavelengths and wave heights of bedforms in pyroclastic surge deposits, and used them for a comparison of relative flow strength. Figure 4.13 shows a comparison of bedform characteristics for the deposits at Hunt's Hole (this study), Ubehebe Crater (Crowe and Fisher 1973, tables 2 and 3), Taal volcano in the Philippines (Waters and Fisher 1971, table 1), Roccamonfina volcano, Italy (Cole 1991), Laacher See, Germany (Schmincke et al. 1973, data approximated from figure 15), Cora Maar, Turkey (Gencalioglu-Kuscu et al. 2007, data approximated from figure 9), and Linosa volcano, Italy (Lajoie et al. 1992). Bedforms show increasing wave heights with increasing wavelength. Bedform measurements at Hunt's Hole, Ubehebe crater, Cora Maar and the two longest wavelength data points from Taal were collected at approximately the same distance from the vent (0.7 to 1.0 km). At approximately the same distance, Hunt's Hole dunes show greater wavelengths and wave heights than those at Ubehebe crater. Using wavelength and wave height as a measure of flow strength (*cf.* Crowe and Fisher 1973), this suggests that the dunes at Hunt's Hole were formed in a flow of greater strength than those at Ubehebe crater. The Hunt's Hole dunes overlap in size

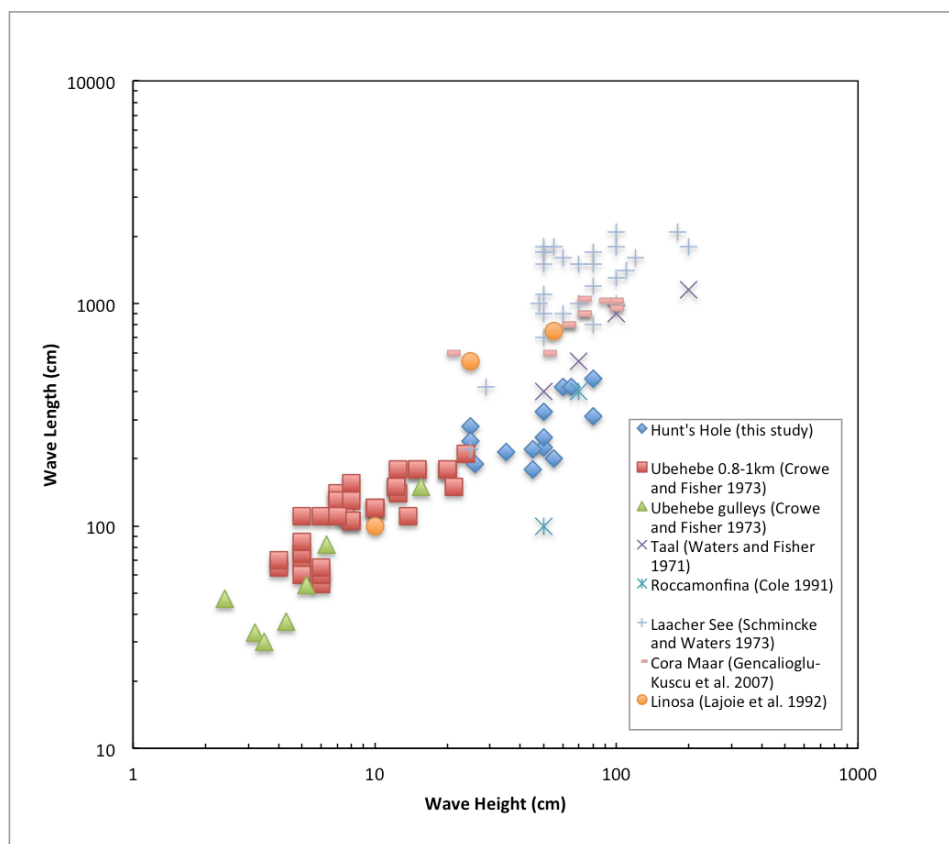


**Figure 4.13:** Wavelength and waveheight of bedforms measured in pyroclastic surge deposits. Waveheight increases with increasing wavelength. See text for discussion.

with the more distal dunes at Taal volcano (collected at 1.5 and 2.0 km from the vent), suggesting that the eruption at Taal produced a flow of greater strength than the eruption at Hunt's Hole (such that the distal deposits at Taal are comparable to the more proximal deposits at Hunt's Hole).

However, despite these inferred differences in flow strength, bedforms at Ubehebe crater, Taal volcano and Cora Maar have been interpreted as antidunes, suggesting upper flow regime conditions (Crowe and Fisher 1973; Schmincke et al. 1973), while we interpret the Hunt's Hole bedforms as low-flow regime. Cole (1991) also suggests that bedforms at Roccamonfina show evidence for both progressive (migrating downstream) and regressive

(migrating upstream) behavior, with some features identified as chute and pool structures, similar to those identified by Schmincke et al. (1973) in the Laacher See. Hunt's Hole and Linosa Volcano (Lajoie et al 1992) are the only locations at which upper flow regime deposits have not been identified. This suggests that either 1) Hunt's Hole represents a class of unique pyroclastic surge deposits, or 2) bedform geometries at other localities may have been misinterpreted. Without studying the other locations we cannot comment on their interpretation, but we raise a cautionary note. Figure 4.14 shows two examples from Hunt's Hole that could potentially be misinterpreted as a chute and pool and an antidune. However, further inspection of cross-bedding geometry, using the surrounding context from 3D exposures, reveals that the potential chute and pool structure (Figure 4.14A) is simply an oblique cut through the trough of a large sinuous bedform, and the potential antidunes (Figure 4.14B) represent an oblique cut through sinuous crested bedforms with shifting crestlines (but the crestlines are not moving upstream).

#### **4.8 Identification on Mars**

It is important to consider the possibility that pyroclastic surge deposits may someday be encountered in outcrops on Mars. At the landing site for the Mars Exploration Rover (MER) *Opportunity* at Meridiani Planum, eolian deposits with some reworking by subaqueous processes was recognized as the dominant process of deposition (Squyres et al. 2004b; Grotzinger et al. 2005; Grotzinger et al. 2006; McLennan and Grotzinger, 2008). However, this was challenged by the alternative possibility of formation by impact or volcanic-induced surges (Knauth et al. 2005; McCollom and Hynek 2005). Further

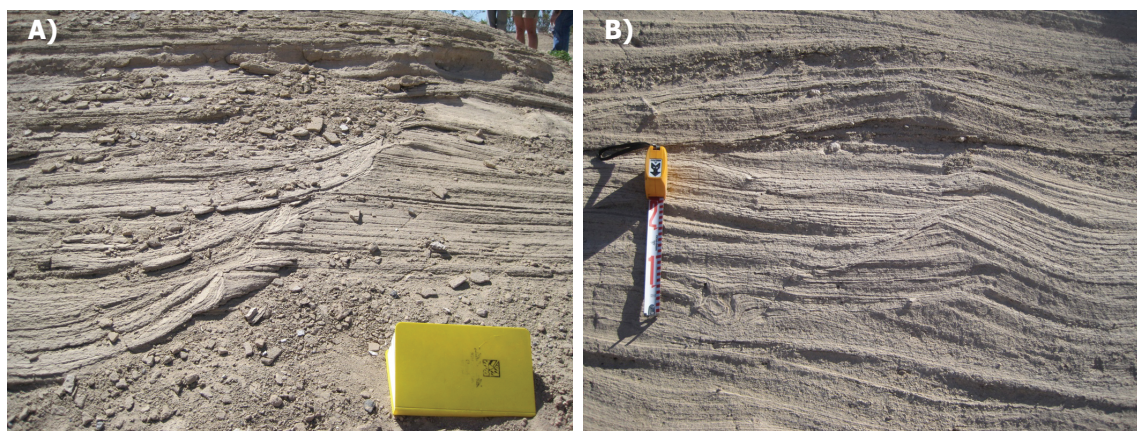


**Figure 4.14:** Bedform geometries at Hunt's Hole that could be misinterpreted as chute and pool structures or potential antidunes. A) A feature showing resemblance to the chute and pool structure described by Schmincke et al. (1973) is actually an oblique cut through the trough of a bedform. Paleoflow direction was into the page and to the right. B) Possible antidune geometry created by shifting crestlines in an outcrop face oblique to flow.

exploration has shown compelling support for the dominantly eolian origin of these deposits (Metz et al. 2009; Hayes et al. 2011; Edgar et al. in press; Fralick et al. 2012). At

the other MER landing site at Gusev Crater, evidence points to pyroclastic deposition followed by possible eolian reworking (Squyres et al. 2007). These cases illustrate that when geologic context is limited, or volcanic indicators such as bombs or lapilli are absent, it may be difficult to distinguish bedforms in pyroclastic surge deposits from those in eolian or fluvial deposits. This suggests a need to establish better criteria for the identification of pyroclastic surge deposits in extraterrestrial strata where full geologic context may be incompletely understood due to the intrinsic limitations of planetary exploration.

Even on Earth it is difficult to distinguish pyroclastic surges from fluvial deposits. Other authors have noted the difficulties (Burt et al. 2008), and described possible ways to

distinguish these deposits (*cf.* Valentine and Fisher 2000; Smith and Katzman 1991).

Even with limited geologic context (as would be the case on Mars), and in the absence of clear volcanic features such as bomb sags and lapilli, pyroclastic surge deposits can be distinguished from eolian and fluvial deposits based on unique properties of bedform geometries and styles of stratification. Here, we summarize the criteria (Table 1) and add criteria specifically related to cross-bedded deposits. Important differences include the preservation of stoss slopes and dune crests, the angle of climb, and the angles of stoss and lee slopes.

- Preservation of crests and stoss sides – Rock outcrops of bedforms in eolian and fluvial deposits typically show sets of cross-bedding, consisting of only lee-side laminae (foresets). In these environments, the rates of migration far exceed the rates of accumulation, and only a fraction of the bedforms are preserved. However, in pyroclastic surge deposits, under decelerating flow conditions, the rate of accumulation is comparable to the rate of migration. This results in stoss side preservation, and in some cases, entire bedforms are preserved. Cohesion of wet ash may also lead to stoss side preservation.
- Angles of stoss and lee slopes – While stoss slopes are comparable to those in modern eolian and fluvial environments, bedforms in pyroclastic surges typically have lee slopes that are less steep than those in eolian and fluvial dunes (Crowe and Fisher 1973; Sheridan and Updike 1975; Smith and Katzman 1991; this study).
- Angles of climb – Another way to identify pyroclastic surge deposits is the presence of dunes with very high angles of climb. In terrestrial deposits, ripples

**Table 4.1.** Characteristics of cross-bedded pyroclastic, eolian, and fluvial deposits.

	<b>Pyroclastic Surge</b>	<b>Eolian</b>	<b>Fluvial</b>
<b>Grain Size and Sorting</b>	For cross-bedded deposits: moderately to poorly sorted, some fines codeposited with coarse material.	Very well sorted, fine to medium sand. Rare exceptions to generally fine grain size are granule ripples but these are also well sorted.	Moderately to well sorted. Range of grain sizes depending on proximity to source region.
<b>Preservation of Dune Crests and Stoss Sides</b>	Common	Very rare, typically only preserve very small fraction of bedform height as foresets.	Rare, typically only preserve small fraction of bedform height as foresets.
<b>Angle of Climb</b>	Supercritical	Subcritical	Subcritical
<b>Angles of Stoss Slopes*</b>	4° to 16° (this study) 0° to 18° (Crowe and Fisher 1973) 10° (Sheridan and Updike 1975)	5° to 10° (Livingstone and Warren 1996) 4° to 11° (Hesp and Hastings, 1998)	A few degrees to 10° to 18°, rarely up to 26° (Carling et al 2000)
<b>Angles of Lee Slopes*</b>	2° to 20° (this study) 3° to 19° (Crowe and Fisher 1973) 10° (Sheridan and Updike 1975)	Up to 30 to 35° in dry sand, up to 42° in moist cohesive sand for dune foresets formed by avalanching (Bigarella et al. 1969; McKee and Bigarella, 1972)	Up to 32 to 37° (Kostaschuk 2000) ~30° to 33° (Carling et al 2000); Typically near the angle of repose for flume experiments (e.g. Guy et al. 1966; Williams, 1967)
<b>Transport Direction</b>	Unidirectional, radially away from point source	Unidirectional or bidirectional, may show seasonal reversals	Unidirectional
<b>Geologic Context</b>	Volcanoes, rifts, craters	Interdune playa and/or sandsheet deposits	Channel deposits, coarse lags, flood plain deposits
<b>Environmentally Diagnostic Associated Structures</b>	Accretionary lapilli, volcanic bombs	Pinstripe lamination associated migrating wind ripples. Reverse-graded laminae.	Mud drapes, mudcracks. Cm-scale ripples, trough - beds. Strong hydrodynamic sorting (decreasing grain size over long transport distance)

\*Angles of stoss and lee slopes are reported for modern dunes in eolian and fluvial environments. However, it is not possible to measure modern dunes in pyroclastic surges, so dune slopes in pyroclastic surges are measured from cross-sections in surge deposits.

may exhibit very high angles of climb, but supercritical angles are almost never seen in dunes. Subcritical angles of climb result in truncation and preservation of only a fraction of original bedform heights. The rapidly decelerating nature of pyroclastic surges produces very high accumulation rates, and allows dunes to climb at critical to supercritical angles, which results in nearly complete bedform preservation.

Yet there may be a few key differences between pyroclastic surges on Earth and Mars. Other authors have discussed the identification of pyroclastic surges on Mars, particularly in the context of Meridiani Planum (Knauth et al. 2005; McCollom and Hynek 2005; Squyres et al. 2006a; McLennan and Grotzinger 2008; Burt et al 2008; Fralick et al. in press). The main differences result from the decreased gravity on Mars. As shown in the hydrodynamic considerations above, the expression for flow depth (equation 4) does not depend on gravity, but the expression for depositional velocity (equation 5) does. For the same flow depth and particle size on Mars, decreased gravity would result in depositional velocities that are roughly half the speed (ranging from 0.6 to 8.5 m/s). Decreased gravity also has an effect on bedform stability fields. As Grotzinger et al. (2005) have shown, the transition between bedform stability fields (for example, from dunes to upper plane bed) occurs at a lower velocity on Mars compared to Earth, or for a constant velocity and flow depth, the transition occurs at a larger grain size. This is important because it means that upper flow regime bedforms, like antidunes and upper plane bed, should occur at lower velocities on Mars.

The ability to distinguish bedforms in pyroclastic surge deposits from those in eolian and fluvial environments is critical to understanding past habitability on Mars. The

criteria discussed here will aid in their correct identification. It is possible that we will one day explore pyroclastic surge deposits on Mars, and investigations will rely on detailed sedimentological work to understand the eruption history and flow conditions. Measurements of bedform geometries, flow directions, and grain size will enable calculations of flow depth and velocity. As outlined above, there are several key differences due to reduced gravity on Mars. While we make a case for low flow regime bedforms at Hunt's Hole, the shift in bedform stability fields for Mars suggests that antidunes and upper plane bed may be easier to achieve in pyroclastic surges on Mars.

#### **4.9 Conclusions**

The corrugated pattern of erosion around the rim of Hunt's Hole provides a unique opportunity to study bedforms in pyroclastic surge deposits. Detailed sedimentological analysis, combined with a relatively new technique of TLS, enables the reconstruction of bedform morphologies and behavior, and provides insight into the flow dynamics of pyroclastic surges.

Hunt's Hole records the migration of three-dimensional transverse bedforms, with very high angles of climb. The deposit at Hunt's Hole likely represents a single eruptive event, with possible pulses in the flow. Observations in vertical succession are all consistent with a temporally decelerating flow, with very high rates of accumulation relative to rates of migration. Contrary to other interpretations of bedforms in pyroclastic surge deposits, all observations at Hunt's Hole indicate low flow regime conditions, with no evidence of upstream migration of bedforms.

Hydrodynamic considerations based on bedforms and grain sizes provide a range of flow depths and velocities for dunes in pyroclastic surge deposits. These estimates are lower than previous estimates of flow velocities. Although the amplitude and wavelengths of bedforms at Hunt's Hole suggest that they were formed in a flow of greater strength than those at Ubehebe crater, our estimates of flow velocities are on the lower end of the anticipated range of pyroclastic surge velocities. Field work at additional locations may elucidate whether Hunt's Hole is a unique lower-velocity, low flow regime location, or if estimates of flow depths and velocities should be refined. Future work including flume experiments to generate bedforms in intermediate densities may shed light on the unique dynamics of these bedforms.

We also provide a summary of criteria for identification of surge deposits, with particular emphasis on their identification on Mars. Even with limited geologic context and an absence of clear volcanic indicators such as bomb sags and lapilli, pyroclastic surge deposits can be distinguished from eolian and fluvial deposits based on unique properties of bedform geometries. However, surge deposits on Mars will differ from those on Earth in several ways due to the effects of decreased gravity.

This work serves to better characterize bedforms in pyroclastic surge deposits at Hunt's Hole, introduces a relatively new remote sensing technique, and provides criteria for the identification of these deposits on Mars.

## RECOGNITION AND SIGNIFICANCE OF STRATAL GEOMETRIES AND UNCONFORMITIES IN MARTIAN LAYERED DEPOSITS

**Abstract**

The deposition and erosion of sedimentary rocks on Mars is controlled by similar water- and wind-moderated processes as those on Earth, and its stratigraphic record can be analyzed through analogous methods. We demonstrate that chronostratigraphic tools, developed for interpreting terrestrial seismic data, can be applied to images of rock outcrops on Mars. This study uses data from the High Resolution Imaging Science Experiment (HiRISE), in combination with Digital Elevation Models (DEMs) and software for chronostratigraphic analysis to quantify the spatial and temporal characteristics of Martian layered deposits. Initial application of this method focuses on the North Polar Layered Deposits (NPLDs) due to their complex stratal geometries, relative lack of surface disturbances, and inferred tie to climate variations. Chronostratigraphic analysis of the NPLD reveals multiple depositional sequences with modeled time increments that are distinct from previous studies. This technique also provides insight regarding the depositional and erosional history of the NPLD margin, through the migration of spiral troughs. Chronostratigraphic analysis indicates that migration occurs as fluctuating depositional events, which may be tied to longer-term climate variations. Application of this method to other layered deposits reveals that one particular location – Galle crater – may represent an ancient polar layered deposit, and that ice may still be present beneath the surface.

## 5.1 Introduction

Stratified rocks on Mars record environmental processes governing both their deposition (Grotzinger et al. 2005; Grotzinger and Milliken, 2012) and subsequent alteration (McLennan et al. 2005; Clark et al, 2005; McLennan and Grotzinger, 2008). In certain cases, the stratigraphic record may be viewed as a “carrier signal” in which other proxies of environmental change are embedded. On Mars, stratigraphic sections possibly record changes such as varying amounts of groundwater or surface precipitation, chemical and mineralogic differences, changes in the relative abundance of suspended dust and volcanic tephra, lake level rise and fall, and other proxies of environmental history of climate change. The diverse sedimentary record on Mars reveals clues about the history of the planet.

However, this record may have omissions, as represented by unconformities. Unconformities result because sedimentation, by its very nature, is discontinuous (Sadler, 1981), and because a broad range of erosive processes may act to remove the record. The geometric patterns of both strata and their associated unconformities can provide important criteria for recognizing certain depositional processes. The acquisition of chronostratigraphic data, derived from geometric relationships, can be used to understand the relative spatial positions of deposition and non-deposition through time. These patterns can be used to predict sedimentary facies as well as internal stratigraphic architecture and continuities of deposits within sedimentary basins.

On Earth, chronostratigraphic techniques are used for stratigraphic correlations, and to understand the location and timing of deposition as well as erosional and non-depositional events. This is particularly useful in the field of hydrocarbon exploration. As

discussed below, chronostratigraphy is used in seismic reflection interpretations, and for basin analysis for source rock, hydrocarbon migration, and trap identification (De Bruin et al. 2007; Monsen et al. 2007; Qayyum et al. 2012). Chronostratigraphy is used to make system tracts interpretations to infer the quality of source, seal and reservoir rocks (De Groot et al. 2006; Brouwer et al. 2008). While the motivation stems from hydrocarbon exploration, the technique reveals information about past surface processes. In addition, the technique will also help in the exploration for organic carbon in sedimentary rocks on Mars.

This study investigates variations in stratal geometries, and their inferred associated unconformities, to better constrain past surface processes and past climate conditions on Mars.

## **5.2 Unconformities, Stratal Geometries, and the Partitioning of Time in the Stratigraphic Record**

The analysis of unconformities and stratal geometries is in its infancy on Mars but it is a common technique used on Earth to identify past environments and processes, especially where data are lacking regarding absolute measurements of time (Vail et al. 1977; Christie-Blick and Driscoll, 1995). This branch of earth science, known as “sequence stratigraphy,” deals with relative temporal relations and ages of stratigraphic successions. The concept was first developed by Blackwelder (1909), who recognized the “missing time” (chronologic hiatus) represented by unconformities in the rock record, and the difficulty in representing both time and space in two dimensions. The idea was further developed by Wheeler (1958), who realized the need to include significant events like

erosion and non-deposition in cross-section, but that these are reduced to zero in cross-sections where the y-axis is thickness. Wheeler (1958) introduced the concept of time-stratigraphic units, which incorporate not only the tangible preserved record, but also non-material parts of the total space-time “volume” represented by non-deposition, and the negative parts of the stratigraphic record representing erosion. These concepts are illustrated in Figure 5.1, known as a chronostratigraphic section or “Wheeler diagram.”

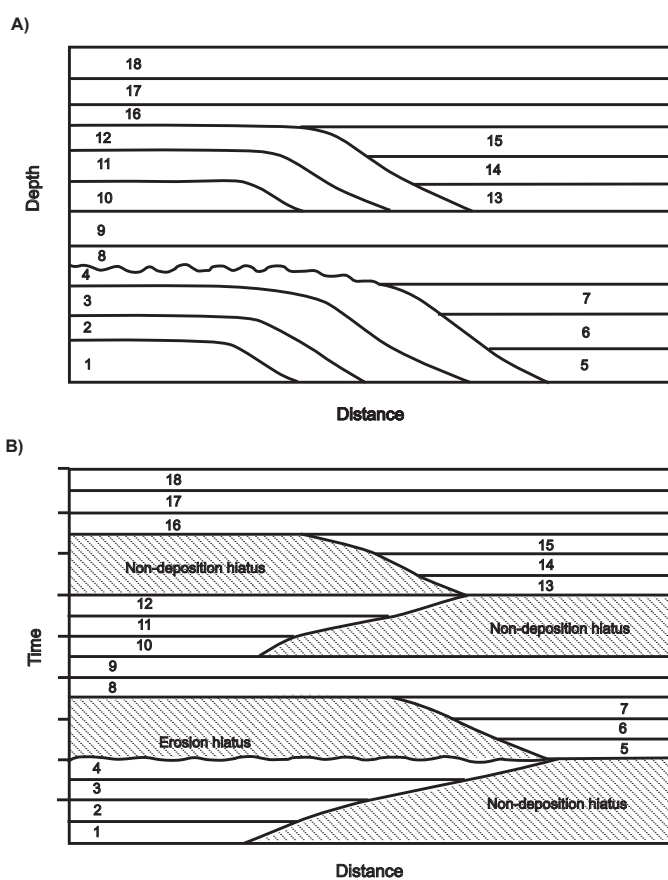


**Figure 5.1:** Construction of a chronostratigraphic diagram. A) Schematic cross-section, showing episodes of progradation, erosion, infilling of topography, and draping. B) Stratigraphic relations in (A) are re-plotted in the time domain, known as a Wheeler diagram. Each layer is given equal geologic time. Hiatuses are illustrated where strata are missing.

Sequence stratigraphy became a mature and valuable scientific discipline with the development of seismic-reflection profiling of buried strata in the 1960s and 1970s. This technology uses the acoustic properties derived from seismic reflections to interpret physical changes in the subsurface represented by bedding surfaces and unconformities with velocity-density contrasts (Vail et al. 1977). It can be thought of as a remote sensing tool, similar to imaging strata from Mars orbit. Seismic data, like orbital imagery, provide a glimpse of structural and stratigraphic relationships, from which inferences about the regional geology can be made. Since all material above an unconformity is younger than the material below it, seismic sections record time-stratigraphic patterns. These seismic reflection patterns indicate the geometry and relative magnitudes of unconformities, allowing for remote inferences of depositional processes.

At the core of sequence stratigraphy is its basic unit of analysis - the depositional sequence: a relatively conformable succession of genetically related strata (Mitchum et al. 1977). Sequence boundaries are identified by the geometry of their bounding terminations, termed onlap, downlap, toplap, and truncation (Vail et al. 1977). Depositional sequences have chronostratigraphic significance in that they were deposited during a time interval limited by the sequence boundaries (although the age of strata within a sequence may vary from place to place).

Sequence stratigraphy is critically important to earth scientists who use the geometry of successions of strata and their associated unconformities to identify important environments, such as those in which organic matter might be concentrated. For example, Dobrin (1977) illustrates the use of seismic reflection patterns to reconstruct depositional

histories and deduce depositional environments. Processes such as delta formation, transgression and regression of sea level, and tilting of strata produce identifiable patterns in seismic sections. Dobrin (1977) uses sequence stratigraphy to identify areas that are most promising for hydrocarbon accumulation, based on the geometric relationships of strata. Other authors demonstrate the frequent use of sequence stratigraphy in predicting the location of hydrocarbon reservoirs (Morton and Galloway 1991), predicting systematic variations in basin fill (Gawthorpe et al. 1994), interpreting structural influences (Ambrose et al. 2009) and building chronostratigraphic frameworks (Qayyum et al. 2012).

We aim to apply the principles of sequence stratigraphy to Mars to identify similarly important environments, including potential traps for organic material. While we do not have seismic data to probe the subsurface of Mars, we can study sedimentary sequences in cross-section where they are exposed in the sloping walls of valleys and impact craters. And in a manner similar to seismic stratigraphy, we can identify sequence boundaries and stratal geometries through image processing – identifying boundaries based on changes in lithology and composition as revealed by changes in color, brightness, erosional resistance (topography) and small-scale textures.

### **5.3 Methods for Chronostratigraphic Analysis**

Chronostratigraphic analysis is made possible through the use of a seismic interpretation platform known as Sismage (Keskes et al. 2004), developed at Total S.A. Sismage contains a suite of algorithms known as Geotime, designed to extract chronostratigraphic information from seismic data. However, rather than analyzing seismic sections we apply this tool to images of stratified deposits on Mars.

First, we identify targets in high-resolution orbital imagery. We use orbital images obtained by the High Resolution Imaging Science Experiment (HiRISE) onboard the Mars Reconnaissance Orbiter to identify sedimentary outcrops on Mars with complex stratal geometries. HiRISE is capable of acquiring images at a resolution of  $\sim 26$  cm/pixel (McEwen et al. 2007). HiRISE images are approximately 6 km wide, and at least 10 km long, which allows extensive stratigraphic sequences to be captured in a single image, resolving features down to  $\sim 1$  m in thickness. Initially, science targets were selected on the basis of complex stratal geometries, to test the application of Geotime. A great amount of work has been done to classify layered deposits on Mars (Grotzinger and Milliken, 2012; Griffes et al. 2010; Stack et al. in prep), many of which are flat-lying. Chronostratigraphic analysis of imagery works best when truncation surfaces and textural variations are recognizable. This enables stratigraphic sections to be subdivided into sequences, defined by bounding unconformities.

After targets are identified, the images are transformed into vertical cross-sections. Cross-sections can be obtained where stratigraphy is exposed in the walls of impact craters, channel systems, and crevasses in ice caps. Digital Elevation Models (DEMs), derived from HiRISE stereo image pairs, can be used to correct for true stratigraphic thicknesses. HiRISE DEMs are used whenever possible, but the coverage is limited. In some locations (discussed below), topography derived from the Mars Orbiter Laser Altimeter (MOLA) can be used to fit a slope, though the resolution is not always appropriate for the features of interest. To produce vertical cross-sections, visible images are draped on DEMs. Using the 3D visualization tool in Sismage®, the DEM is corrected to a vertical view, and a new

image is captured – essentially projecting the apparent view onto a vertical plane. This image is then orthorectified and used for Geotime analysis.

After transformation of orbital images into vertical cross-sections, several filtering steps may be required. Unlike seismic sections, which contain relatively smooth reflections, images of the martian surface may contain a variety of features that obscure bedding. It is important to remove surface “noise” such as slope-streaks and shadows. In some cases it may be necessary to enhance the continuity along bedding (generally in the horizontal direction). Individual beds are treated as timelines, so their continuity is critical.

Images are then processed through Geotime. Geotime is based on the concept of tracing of seismic reflectors – or changes in albedo, in HiRISE images – and integrating the time value of these surfaces where they converge (Figure 5.2A). These accumulation values are taken as proxies for the relative duration of hiatus at any point. Distinct geometries revealed by mapping convergence provide the basis for delineating sequences (Figure 5.2B). Next, the relative age and duration of the sequences, and the magnitude of their bounding unconformities is assessed by assigning ages based on the convergence density; this results in a Wheeler diagram in which time rather than rock thickness is on the y-axis (Figure 5.2C). Manual editing may be required depending on the quality of the Wheeler diagram output, to ensure that stratigraphic sequences are grouped or split correctly.

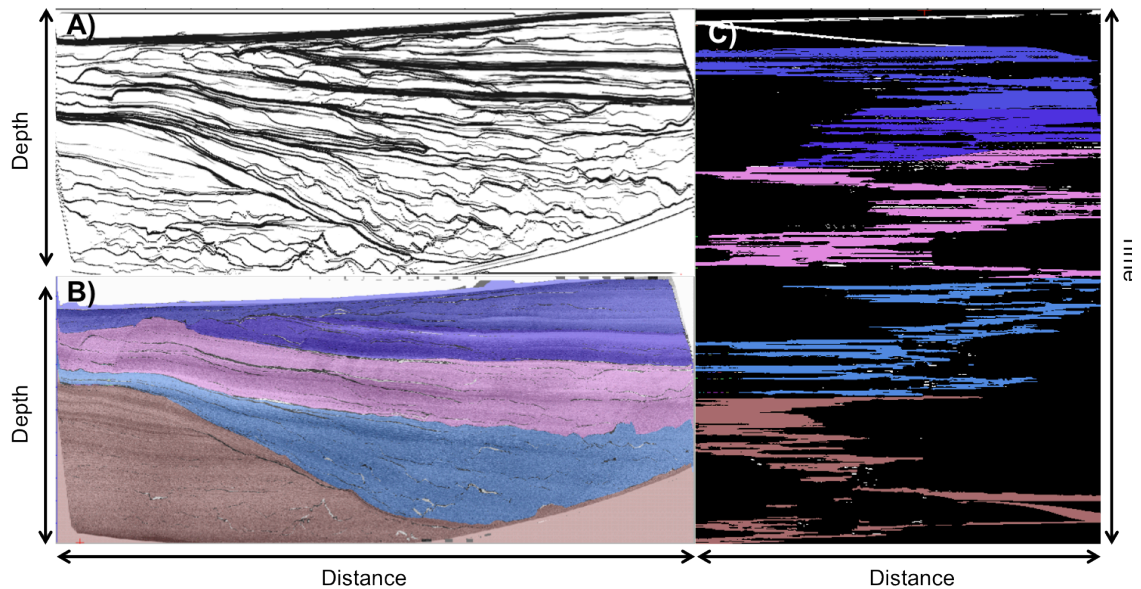


**Figure 5.2:** Geotime work-flow based on HiRISE image PSP\_009337\_2600 of the Martian North Polar Layered Deposits. A) Accumulation diagram showing convergence of layers. Thick black lines are layer boundaries. Thin black lines are artifacts of surface disturbances. B) Sequences identified and superimposed on (A). C) Corresponding Wheeler diagram. Black areas represent regions of erosion or non-deposition. Colored areas correspond to sequences in (B). This package shows evidence for erosion, infilling of topography, progradation, and draping.

We cannot measure absolute time on Mars, so we instead calculate relative time by assuming that each layer represents the same amount of time. The same approach is applied to seismic data where no well control or biostratigraphy is present. In the absence of absolute age constraints, this is an inherent assumption in all chronostratigraphic studies, and implies equal accumulation rates for all strata. As long as the same vertical stretch is applied to all images, the relative modeled time can still be used for comparison across multiple sites.

This work-flow allows us to test hypotheses for the processes controlling deposition and erosion. Chronostratigraphic data (Wheeler diagrams), derived from geometric

relationships, can be used to understand the relative spatial positions of deposition and non-deposition through time. This provides insight into the dynamics of sedimentary accumulation, which is essential for prediction of sedimentary facies.

#### **5.4 North Polar Layered Deposits**

While these methods can be applied to many stratified deposits, the focus of this study is the NPLD due to their complex stratal geometries, relative lack of surface disturbances (such as impact craters and slope streaks that obscure strata), and inferred tie to climatic variations. The NPLD is a ~3 km thick deposit consisting of sediment and ice in varying proportions, forming the bulk of the plateau of Planum Boreum, the northern plain of Mars (Figure 5.3). The layered appearance is attributed to different fractions of dust and ice (Cutts and Lewis, 1982; Thomas et al. 1992), producing variations in albedo.

Unconformities in the NPLD are common (Tanaka, 2005; Byrne, 2009), though their formation is not well understood. Potential formation mechanisms include retreat and advance of the PLD margin, erosion and later unconformable deposition, changes in mass balance patterns, and even tectonic disturbance of the stratigraphy (Fishbaugh 2008). The NPLD have been regarded as a “Rosetta Stone” for reading the record of recent climate change on Mars, but much is unknown about their physical characteristics, age, and the processes controlling deposition and erosion.

Previous studies have focused on albedo variations in the NPLD as a record of climate change. Laskar et al. (2002) used images from the Mars Orbiter Camera (MOC) to analyze brightness versus depth. They found a dominant signal in brightness around

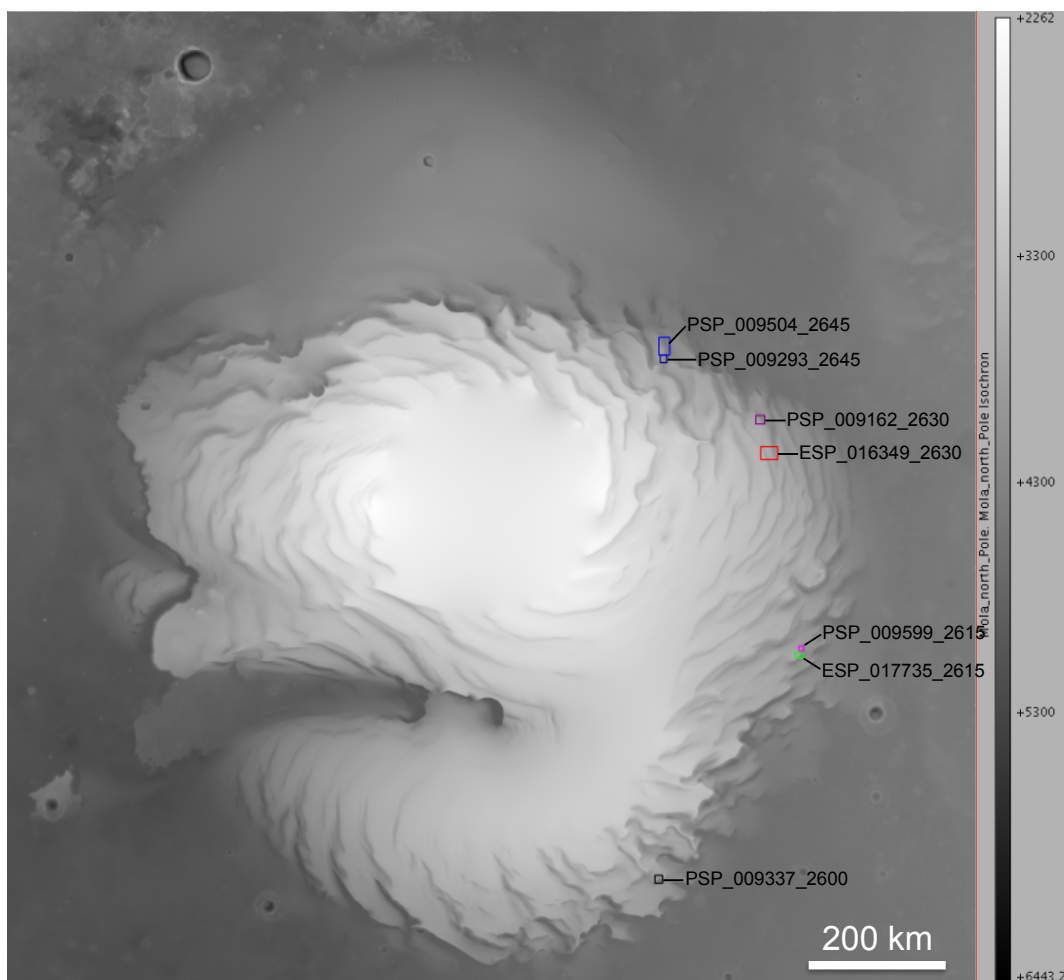


**Figure 5.3:** MOLA topography of the NPLD showing HiRISE footprints of target locations. Targets are located near the margin of the NPLD, exposed in spiral troughs.

~26 m, which they attributed to a 51 kyr insolation cycle. Milkovitch and Head (2005) also performed a spectral analysis of vertical sections, and found a repetitive signal ~30 m thick in the upper part of the deposit. Milkovitch and Head (2005) also suggest that this might correspond to the 51 kyr insolation cycle. However, when deeper (lower elevation/older) sections were analyzed, the spectral signatures vary in thickness (Milkovitch and Head, 2005), or differ little from those that stochastic processes would generate (Perron and Huybers, 2009).

The stratigraphic sections used in spectral analyses are all flat-lying, and it was assumed that the sections were complete records of the NPLD. However, these analyses do not account for the missing time represented by periods of non-deposition and/or erosion. It is clear that non-deposition and erosion are part of the history of the NPLD, because many unconformities have been recognized. Unconformities were first recognized from Viking data (Howard et al. 1982), and more unconformities have been identified in higher resolution datasets. Tanaka (2005) used MOC images to map the distribution of unconformities and found that unconformities are concentrated at the periphery of the NPLD and in regions where different troughs and scarps cross-cut each other. Fortezzo and Tanaka (2010) used Mars Reconnaissance Orbiter (MRO) Context Camera (CTX) images (~6 m/pixel) to identify 308 unconformities. Fortezzo and Tanaka (2010) report a mean latitude of 81.7°N, with lengths ranging from ~650 m to ~114 km, at elevations from -5010 m to -2609 m.

In this study, we focus on images that contain unconformities, because the truncations provide a way to assess time.

### **5.5 Chronostratigraphic Analysis of the NPLD**

This initial study shows that Sismage and Geotime can be applied to images of rock outcrops in addition to seismic data, which greatly expands the possible applications of this tool for chronostratigraphic analysis. We have established a work-flow for image analysis, though the degree of image processing and filtering is unique to each image. Filtering images improves the quality of the convergence model and ultimately the quality and accuracy of the Geotime output. Additionally, we find that although HiRISE DEMs have

limited coverage, MOLA topography can be used to fit a slope, which enables the analysis of many more locations.

Initial results show that the Geotime output for Mars outcrops resembles terrestrial examples (*cf.* Keskes et al. 2004, De Bruin et al. 2007; Qayyum et al. 2012). This suggests that the patterns of deposition and erosion on Mars may be controlled by similar processes as those on Earth.

We analyzed 7 NPLD locations (Table 5.1). Visual inspection of HiRISE imagery reveals stratal relationships such as onlap, downlap, toplap, erosional truncation, and concordance (Figure 5.4). These translate into Wheeler diagrams with discrete depositional sequences, often containing patterns of progradation, retrogradation, infilling of topography and draping. While not uniform, deposition does appear to be relatively constant. The locus of deposition shifts back and forth through time, but is not completely cut off. For each increment in time there is some point in space where accumulation occurs (Figure 5.5).

Geotime results indicate that each of the selected NPLD locations contains 4 to 6 depositional sequences. The average modeled time of the sequences (measured as the distance from the first occurrence to the last occurrence of a particular sequence in a Wheeler diagram) ranges from 116 to 155 pixels, where each pixel represents a unit of time.

The importance of these modeled time values is that they potentially highlight a timescale of deposition that is different than previously recognized, and this timescale accounts for “missing time” represented by erosion or non-deposition. The key assumption

**Table 5.1:** NPLD targets identified in HiRISE imagery, with corresponding Geotime results.

NPLD image number	Latitude (o)	Longitude (o)	# Geotime sequences	Average modeled time for sequences	Ratio of deposit to space time volume
ESP_016349_2630	83	99.2	5	142	0.53
ESP_017735_2615	81.4	63.3	5	128.8	0.43
PSP_009162_2630	83	106.2	6	116	0.52
PSP_009293_2645	84.5	128.6	5	125.4	0.42
PSP_009337_2600	79.8	24.1	4	155.75	0.27
PSP_009504_2645	84.3	130.9	5	151.8	0.32
PSP_009599_2615	81.5	64.4	4	150.75	0.31

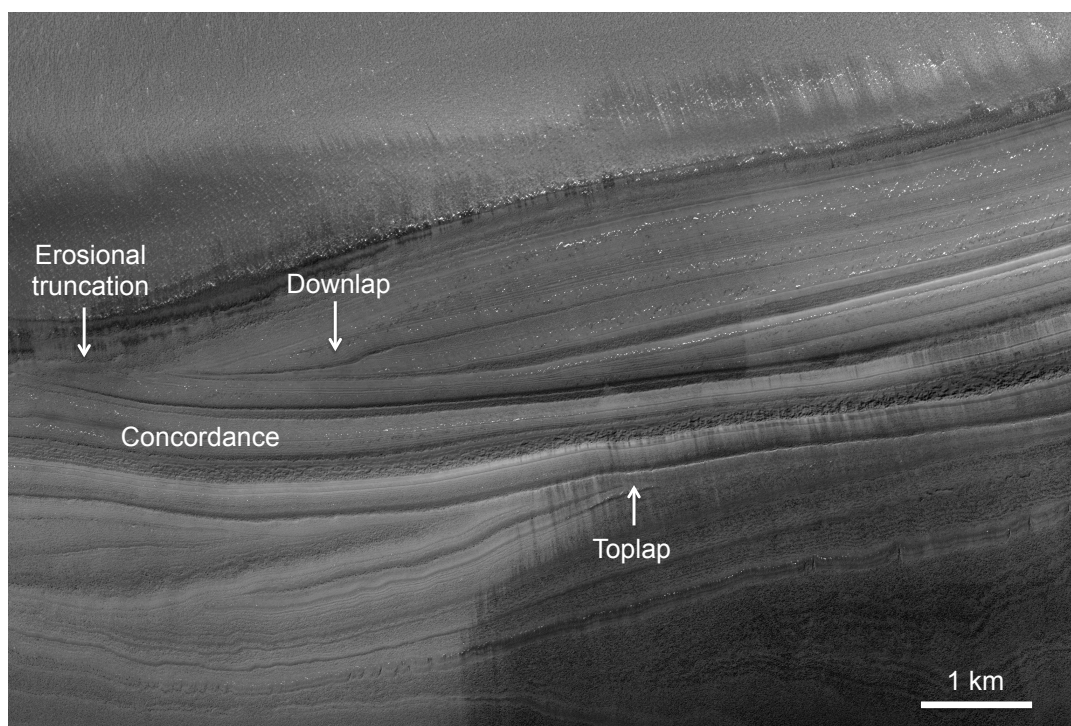


**Figure 5.4:** Stratal geometries identified in HiRISE image PSP\_009293\_2645. Depositional sequences are identified by stratal relationships including toplap, downlap, concordance and erosional truncation.

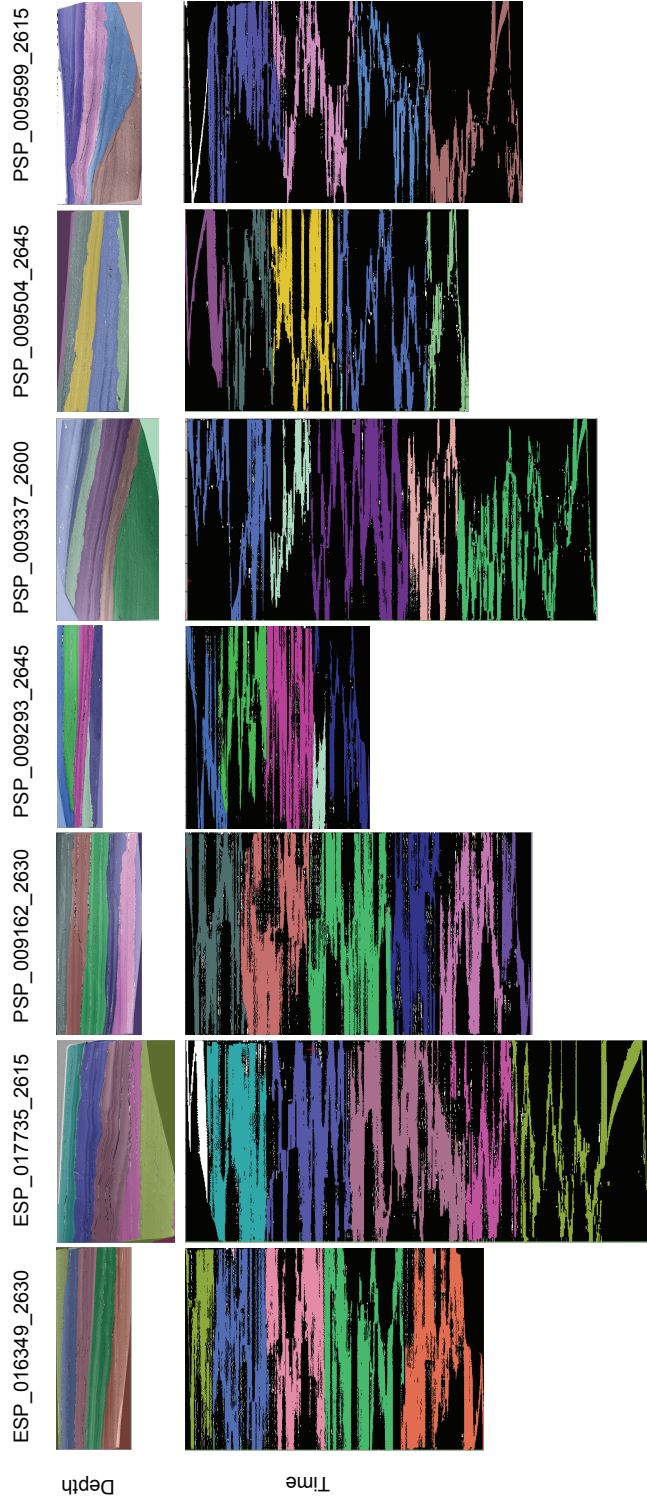


**Figure 5.5:** Compilation of Geotime results for the NPLD. Sequences are identified and mapped on images (top row), with corresponding Wheeler diagrams (bottom row). Colors are randomly assigned to deposits at each location, and do not correlate across the different images. All images are 5x vertically exaggerated. The images and Wheeler diagrams vary in height based on the thickness of exposed stratigraphy. Note the shifting locus of deposition, but lack of large hiatuses in the NPLD record.

involved in this assessment is that the beds are given equal accumulation rates. We propose that this may be a more complete record of the NPLD history, and future work relating to climate signals and cyclicity would benefit from this kind of analysis.

We also evaluate the total space-time area by calculating the ratio of deposition (represented by colored sequences) to the total space-time area (the dimensions of the Wheeler diagram). For the NPLD sites, these ratios range from 0.27 to 0.53. The deposition ratios indicate that for a given space-time volume, the deposit that is preserved represents only about a quarter to a half of the possible volume (if deposition was uniform and continuous, the ratio would be 1). This kind of chronostratigraphic analysis may serve as a new way to assess mass balance patterns in the NPLD, as well as to classify layered deposits on Mars and make comparisons between different depositional environments.

This technique may help test formation mechanisms for unconformities in the NPLD. Proposed mechanisms include retreat and advance of the PLD margin, erosion and unconformable deposition, changes in mass balance patterns, and tectonic disturbance (Fishbaugh et al. 2008). None of the sites that were analyzed in this study show evidence for faulting. Faulting would produce offset layers of equal thickness, rather than erosional truncation and stratal terminations as discussed above (and shown in Figure 5.4). Unconformities that result from differing mass balance patterns are expressed as wide-scale unconformable deposition, and can only be identified through PLD-wide mapping (Fishbaugh and Hvidberg 2006). Wide-scale PLD unconformities resulting from mass balance differences are outside the scope of this study, which focuses on the abundant angular unconformities seen in individual HiRISE images. Retreat and advance of the

NPLD margin is a likely candidate for formation of the angular unconformities, since all of the sites selected in this study lie on the margin of the polar cap. These unconformities result from erosion and unconformable deposition, though the exact mechanism is still unknown.

The sites selected in this study are generally exposed on the south-facing walls of spiral troughs. Previous studies, using Viking and Mariner imagery, noted the exposure of layers on equator-facing (northern) slopes and the absence of exposed layers on pole-facing (southern) slopes (Howard, 1978; Cutts 1973; Soderblom et al. 1973). Howard (1978) suggested that this was due to erosion on the northern slope and deposition on the southern slope, leading to northward migration of spiral troughs. Squyres (1979) and Howard et al. (1982) propose that this migration is the result of preferential erosion of equator-facing slopes due to solar ablation, followed by transport of eroded material to pole-facing slopes via katabatic winds. Smith and Holt (2010) use radar data to study the large-scale structure of the NPLD and suggest that trough migration is dominated by wind transport and atmospheric deposition.

If ice and sediment are transported by katabatic winds, most of the exposed layers in this study represent flow transverse cross-sections, according to overall wind patterns from wind streak mapping Howard (2000). However, one site lies on the western slope of a bisected trough, providing a cross-section that is potentially flow-parallel relative to the katabatic wind and inferred migration direction. While Smith and Holt (2012) provide a simple model of trough migration exhibiting constant northward progress, using sequence stratigraphic analysis we find that migration was a more complex process. In HiRISE

image PSP\_009293\_2645 (Figure 5.6), migration occurred northward, followed by infilling of topography. This was followed by a thick package of ice and sediment that drapes the underlying sequences. Then deposition proceeded northward, followed by another draping episode (Figure 5.6). Chronostratigraphic techniques to trace the locus of deposition may provide a record of spiral trough migration and advance and retreat of the polar cap margin. The hypothesis that spiral troughs migrate as the result of katabatic winds is further supported by THEMIS VIS images, which capture laminar flow down south-facing slopes, followed by hydraulic jumps and flow thickening on north-facing slopes (Smith and Holt 2010, 2012). The majority of images that capture these events occur between solar longitude ( $L_s$ ) 76 and 98, suggesting that the poleward migration of troughs occurs during late spring and early summer (Smith and Holt 2012). Preliminary results using chronostratigraphic analysis also suggest that northward migration was not continuous, but rather occurs as fluctuating depositional events, which manifest themselves as genetically related sequences observed in Wheeler diagrams.

## **5.6 Application to Other Regions on Mars**

In a survey of HiRISE imagery of other layered deposits, one particular location showed striking resemblance to the NPLDs. Galle crater (51°S 31°W) is a 231 km in diameter impact crater located on the eastern rim of Argyre Planitia. These topographic features expose layered deposits, particularly in the southern part of the crater. The geologic history of Galle crater is poorly constrained, but it contains a variety of morphological features, including layered deposits, fluvial channels breaching the crater rim, dunes, glacial features and gullies (Reiss et al. 2006). The lowermost layered deposits

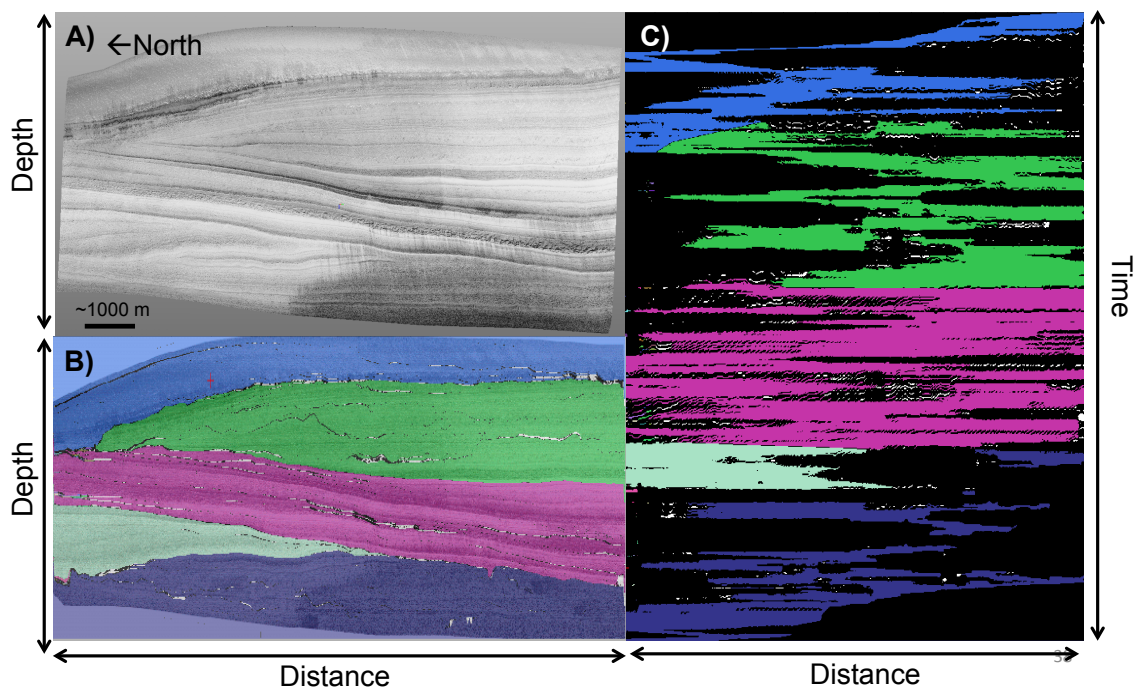


**Figure 5.6:** Stratigraphy exposed in the wall of a spiral trough, providing a cross-section that is parallel to the inferred migration direction. North is to the left. A) HiRISE image PSP\_009293\_2645, draped on MOLA topography and 5x vertically exaggerated. B) Sequences are identified based on convergence densities, and mapped on (A). C) Wheeler diagram, showing evidence of northward migration, infilling of topography and draping, followed by renewed northward migration and draping. Tracing the locus of deposition may provide insight into the migration patterns of spiral troughs and processes acting on the NPLD margin.

show evidence for complex stratal geometries, and multiple sequences are exposed in an interior crater mound. Reiss et al. (2006) propose a possible lacustrine origin for the layered deposits, based on valley networks that breach the crater rim, and “unconformable contacts” which may result from alternating phases of deposition and erosion. Alternatively, Ansan and Mangold (2003) suggest that it may be an ancient polar layered

deposit, based on its inferred young age, easily eroded material, and geologic context in a region in which ice may be stable near the surface.

HiRISE imagery reveals many similarities between the lower layered deposits at Galle crater and the layers comprising the NPLD (Figure 5.7). Both sites contain multiple truncation surfaces bounding depositional sequences. The sequences can be traced for several kilometers, and terminate in angular unconformities at low to high angles. Individual layers are identified based on albedo differences, and the layers are of similar scale and morphology. At both Galle crater and the NPLD, angular unconformities are common at the base of the sections, and are overlain by flat-lying layers that build most of the topographic relief.

Geotime results also indicate that Galle is similar to the NPLD. The Wheeler diagram for Galle crater reveals multiple depositional sequences showing patterns of progradation, retrogradation, and draping (Figure 5.8). Deposition is non-uniform, but continuous through the section. In vertical section, 6 depositional sequences can be identified at Galle crater. The sequences have an average modeled time of 125 pixels, and a deposition to total space-time area ratio of 0.36. These values fall right in the middle of the range for the NPLD.

Based on similar scale, morphology and chronostratigraphic characteristics, the results suggest that Galle crater may represent an ancient polar layered deposit, as proposed by Ansan and Mangold (2003). While Ansan and Mangold limit their analysis to the geologic context, age, and morphology of deposits, the same interpretation may be reached through analysis of stratal geometries. If Galle represents an ancient polar layer deposit,

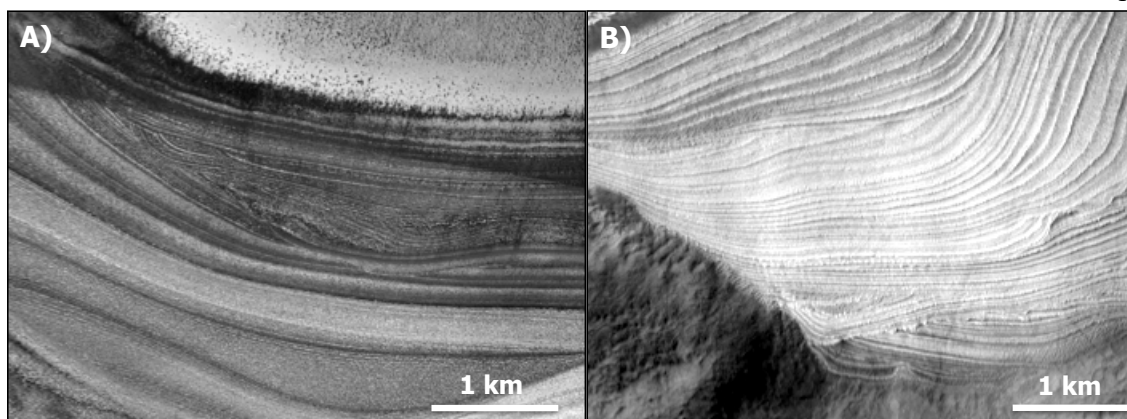


**Figure 5.7:** Comparison of the NPLD (A) and a layered deposit in Galle crater (B). The images contain evidence for multiple angular unconformities, bounding sequences of similar scale and morphology. A) HiRISE image PSP\_010234\_2600. B) HiRISE image PSP\_03855\_1275.

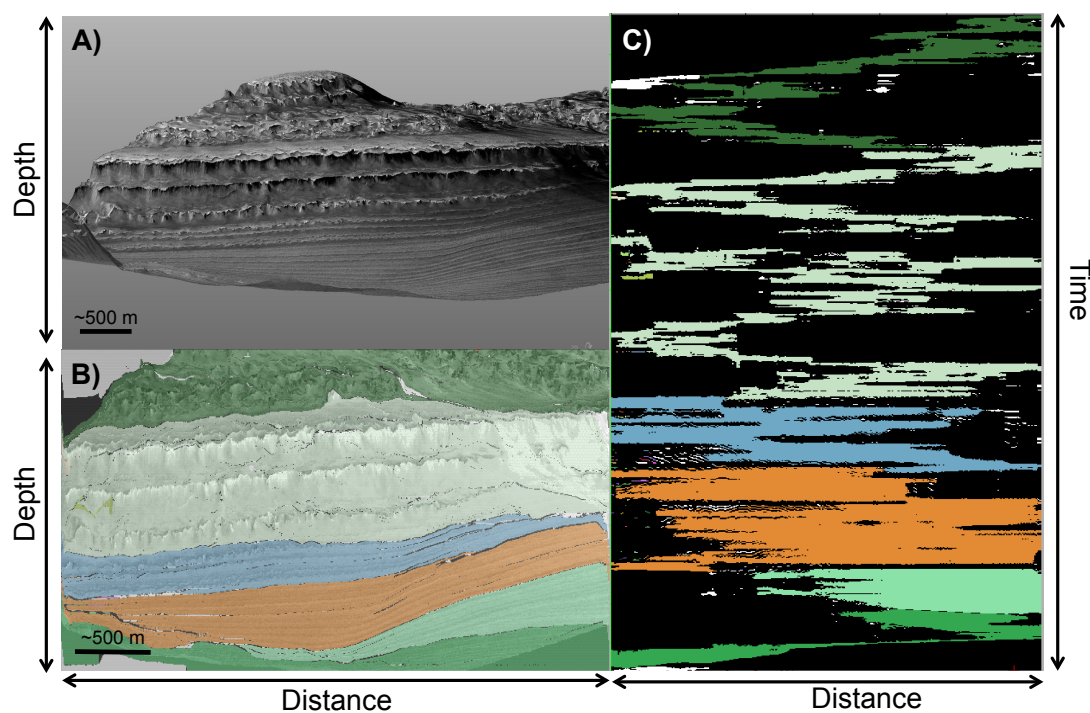


**Figure 5.8:** Geotime results for Galle crater. A) HiRISE DEM of the layered mound in Galle crater, created from stereo images PSP\_010234\_2600 and PSP\_003934\_1275. The view has been orthorectified and 5x vertically exaggerated. B) Sequences identified and mapped on (A). C) Wheeler diagram, containing 6 depositional sequences, with evidence for progradation, retrogradation and draping. The locus of deposition is variable, but there are no large hiatuses.

the multiple truncation surfaces present in the deposit may represent advance or retreat of the ice margin, or migration of topographic irregularities (troughs).

### **5.7 Implications of a Polar Layered Deposit in Galle Crater**

If Galle contains an ancient polar deposit, the fact that the layers are of similar scale to those in the modern polar cap suggests that ice may still be present. The PLDs are thought to be a mix of sediment and ice, with volume fractions of dust ranging from 2 to 10% (Picardi et al. 2005; Plaut et al. 2007). Assuming that Galle crater has a similar composition to the current PLDs, these low concentrations of dust suggest that if all of the ice were to sublime away, the stratigraphy would collapse. Therefore the retention of depositional sequences at the same scale as the modern PLDs may indicate a lack of compaction or sublimation at Galle crater, and points to preservation of ice in a non-polar region. The possible presence of ice in a non-polar region has important implications for habitability, as well as for constraining the global water budget.

Similar to the Earth, variations in orbital parameters are thought to drive climate changes on Mars. While the timescale of variability is similar, the ranges of Mars' variations are significantly greater. Mars' obliquity reaches more than 45° (Laskar et al. 2002). At these times of high obliquity (45°), ice is predicted to persist near the equator (Richardson and Wilson, 2002), which may explain the possible presence of ice in Galle crater. An alternative hypothesis is that the rotation axis shifted due to true polar wander, which could also lead to the presence of polar deposits in some of the modern day mid-latitudes (Schultz and Lutz 1988). Schultz and Lutz (1988) suggest that the terrain between

Argyre and Hellas, including Galle crater, would have been within 45° of a pole over most of geologic time, and therefore should contain evidence of peripheral polar deposits.

The possible presence of ice in Galle crater is further supported by the recognition of many glacial features in the southern mid-latitudes (Kargel and Strom 1992), and recent work that suggests that residual ice may remain buried beneath the surface, particularly east of the Hellas impact basin (Head et al. 2005; Holt et al. 2008). Kargel and Strom (1992) suggest that the northern limit of southern hemisphere glaciation in the vicinity of Argyre was ~40°S (encompassing Galle crater), and Galle crater lies in the same latitude belt as the proposed ice deposits east of Hellas. Although it is not possible to confirm the presence of ice deposits at Galle crater based on orbital imagery, we believe that its similarities to the NPLD, and comparable latitude to other proposed ice deposits make it a good candidate for an ancient polar layered deposit. However, surface elemental mapping via gamma-ray spectroscopy does not reveal a strong water signature at Galle crater (Boynton et al. 2007), so it is inferred that the ice must be buried. Yet the stratification is still visible, which suggests that if ice is present, it must exist just below the surface, perhaps buried under a thin coating of dust. Theoretical predictions imply that dust can insulate buried ice on Mars (Skorov et al. 2001). A thin coating of dust, combined with the topographic expression of the layered deposits may explain the stratified appearance but lack of elemental signature of buried ice at Galle crater.

It is also interesting to note that this deposit occurs as an interior crater mound. Numerous craters on Mars contain mounds, thought to be the result of substantial fill and partial exhumation. The layers in the Galle crater mound appear to have no relation to the

current form of the mound – layers do not pinch out at the mound margins. This suggests that the processes that formed the mound layers are not related to the current processes acting to remove material from the mound. This has implications for other craters with central mounds, such as Gale crater, the landing site for the upcoming Mars Science Laboratory rover mission.

### **5.8 Summary and Significance**

This study demonstrates that chronostratigraphic techniques can be applied to images of outcropping sedimentary rocks and ice. The Mars NPLD provide an ideal location for initial testing of this method, due to their complex stratal geometries and relative lack of surface disturbances (such as impact craters and slope streaks that obscure primary stratification). Chronostratigraphic analysis of the NPLD reveals depositional sequences with modeled time increments that are potentially distinct from previous studies of albedo variations. We propose that future studies of climate signals and cyclicity in the NPLD would benefit from chronostratigraphic techniques, in order to build a more complete record of NPLD history.

Chronostratigraphic analyses of the NPLD provide insight into the migration of spiral troughs. Through the use of Wheeler diagrams, we suggest that spiral trough migration is not continuous, but rather occurs as fluctuating depositional events. These fluctuations may be tied to longer-term climate variations.

Comparison of the NPLDs to other layered deposits on Mars reveals that Galle crater has very similar physical attributes, both in HiRISE imagery and in Wheeler diagrams. We suggest that Galle crater may represent an ancient polar layered deposit, and

that ice may still be present beneath the surface. Furthermore, we suggest that the processes involved in constructing the mound are different than those currently acting to erode the mound.

The techniques introduced in this study are important not just for understanding polar layered deposits, but as a globally-applicable tool for viewing and interpreting any stratified deposit (on Mars, and on Earth). The results of this study can be used to test models for sediment and ice accumulation, which provide further insight into environmental processes that influence the evolution of life.

## BIBLIOGRAPHY

- Ambrose, W. A., T. F. Hentz, F. Bonnaffé, R. G. Loucks, L. F. Brown, F. P. Wang, and E. C. Potter (2009), Sequence-stratigraphic controls on complex reservoir architecture of highstand fluvial-dominated deltaic and lowstand valley-fill deposits in the Upper Cretaceous (Cenomanian) Woodbine Group, East Texas field: Regional and local perspectives, *AAPG Bulletin*, 93(2), 231-269.
- Amundson, R., S. Ewing, W. Dietrich, B. Sutter, J. Owen, O. Chadwick, K. Nishiizumi, M. Walvoord, and C. McKay (2008), On the in situ aqueous alteration of soils on Mars, *Geochimica Et Cosmochimica Acta*, 72(15), 3845-3864.
- Anderson, R. B., and J. F. Bell III (2010), Geologic mapping and characterization of Gale crater and implications for its potential as a Mars Science Laboratory landing site, *Mars*, 5, 76-128.
- Ansan, V., and N. Mangold (2003), Identification of Past Polar Deposits Among Layered Terrains on Mars: Preliminary Results, paper presented at Third Mars Polar Science Conference, Abstract #8071.
- Arvidson, R., et al. (2003), Physical properties and localization investigations associated with the 2003 Mars Exploration rovers, *Journal of Geophysical Research: Planets*, 108(E12), 2156-2202.
- Arvidson, R. E., et al. (2011), Opportunity Mars Rover mission: Overview and selected results from Purgatory ripple to traverses to Endeavour crater, *J Geophys Res-Planet*, 116.

- Bathurst, R. G. C. (1975), *Carbonate Sediments and Their Diagenesis*, Elsevier Science Ltd.
- Bell, J. F., et al. (2003), Mars Exploration Rover Athena Panoramic Camera (Pancam) investigation, *J Geophys Res-Planet*, 108(E12), -.
- Bell, J. F., J. Joseph, J. N. Sohl-Dickstein, H. M. Arneson, M. J. Johnson, M. T. Lemmon, and D. Savransky (2006), In-flight calibration and performance of the Mars Exploration Rover Panoramic Camera (Pancam) instruments, *J Geophys Res-Planet*, 111(E2), -.
- Bellian, J. A., C. Kerans, and D. C. Jennette (2005), Digital outcrop models: Applications of terrestrial scanning lidar technology in stratigraphic modeling, *J Sediment Res*, 75(2), 166-176.
- Belousov, A., and M. Belousova (2001), Eruptive process, effects and deposits of the 1996 and the ancient basaltic phreatomagmatic eruptions in Karymskoye lake, Kamchatka, Russia, *Volcaniclastic Sedimentation in Lacustrine Settings*, 35-60.
- Bigarella, J. J., R. D. Becker, and G. M. Duarte (1969), Coastal Dune Structures from Paranz (Brazil), *Mar Geol*, 7(1), 5-55.
- Blackwelder, E. (1909), The valuation of unconformities, *J Geol*, 17(3), 289-299.
- Blasius, K. R., J. A. Cutts, J. E. Guest, and H. Masursky (1977), Geology of the Valles Marineris: First analysis of imaging from the Viking 1 Orbiter primary mission, *J Geophys Res*, 82(28), 4067-4091.
- Blatt, H., G. Middleton, and R. Murray (Eds.) (1980), *Origin of Sedimentary Rocks*, Prentice Hill.

- Boynton, W. V., et al. (2007), Concentration of H, Si, Cl, K, Fe, and Th in the low- and mid-latitude regions of Mars, *J Geophys Res-Planet*, 112(E12).
- Brand, B. D. (2008), Mafic phreatomagmatic volcanism and density current dynamics (Doctoral dissertation), 287 pp, Arizona State University.
- Branney, M. J., and B. P. Kokelaar (2002), *Pyroclastic density currents and the sedimentation of ignimbrites*, Geological Society Pub House.
- Bridges, N. T., et al. (2010), Aeolian bedforms, yardangs, and indurated surfaces in the Tharsis Montes as seen by the HiRISE Camera: Evidence for dust aggregates, *Icarus*, 205(1), 165-182.
- Bridges, N. T., and D. R. Muhs (2012), Duststones on Mars: Source, Transport, Deposition, and Erosion, *Sedimentary Geology of Mars, SEPM Special Publication*, 102, 169-182.
- Brouwer, F., G. De Bruin, P. De Groot, and D. Connolly (2008), Interpretation of Seismic Data In The Wheeler Domain: Integration With Well Logs, Regional Geology And Analogs, paper presented at Society of Exploration Geophysicists Annual Meeting, Las Vegas.
- Burt, D. M., L. P. Knauth, K. H. Wohletz, and M. F. Sheridan (2008), Surge deposit misidentification at Spor Mountain, Utah and elsewhere: A cautionary message for Mars, *J Volcanol Geoth Res*, 177(4), 755-759.
- Byrne, S. (2009), The Polar Deposits of Mars, *Annual Review of Earth and Planetary Sciences*, 37, 535-560.

- Carling, P. A., J. J. Williams, E. Golz, and A. D. Kelsey (2000), The morphodynamics of fluvial sand dunes in the River Rhine, near Mainz, Germany. II. Hydrodynamics and sediment transport, *Sedimentology*, 47(1), 253-278.
- Cas, R. A. F., and J. V. Wright (1987), *Volcanic successions, modern and ancient: A geological approach to processes, products, and successions*, Allen & Unwin London.
- Chan, M. A. (1999), Triassic loessite of north-central Utah: Stratigraphy, petrophysical character, and paleoclimate implications, *J Sediment Res*, 69(2), 477-485.
- Christensen, P. R., et al. (2000), Detection of crystalline hematite mineralization on Mars by the Thermal Emission Spectrometer: Evidence for near-surface water, *J Geophys Res-Planet*, 105(E4), 9623-9642.
- Christie-Blick, N., and N. W. Driscoll (1995), Sequence stratigraphy, *Annual Review of Earth and Planetary Sciences*, 23, 451-478.
- Clark, B. C., et al. (2005), Chemistry and mineralogy of outcrops at Meridiani Planum, *Earth and Planetary Science Letters*, 240(1), 73-94.
- Cole, P. D. (1991), Migration Direction of Sand-Wave Structures in Pyroclastic-Surge Deposits - Implications for Depositional Processes, *Geology*, 19(11), 1108-1111.
- Crowe, B. M., and R. V. Fisher (1973), Sedimentary Structures in Base-Surge Deposits with Special Reference to Cross-Bedding, Ubehebe Craters, Death Valley, California, *Geol Soc Am Bull*, 84(2), 663-681.
- Cutts, J. A. (1973), Wind Erosion in Martian Polar Regions, *J Geophys Res*, 78(20), 4211-4221.

- Cutts, J. A., and B. H. Lewis (1982), Models of Climate Cycles Recorded in Martian Polar Layered Deposits, *Icarus*, 50(2-3), 216-244.
- Dade, W. B., and H. E. Huppert (1996), Emplacement of the Taupo ignimbrite by a dilute turbulent flow, *Nature*, 381(6582), 509-512.
- de Bruin, G., N. Hemstra, and A. Pouwel (2007), Stratigraphic surfaces in the depositional and chronostratigraphic (Wheeler-transformed) domain, *The Leading Edge*, 26(7), 883-886.
- de Groot, P., G. de Bruin, and N. Hemstra (2006), How to create and use 3D Wheeler transformed seismic volumes, paper presented at Society of Exploration Geophysicists Annual Meeting, New Orleans.
- DeHon, R. A. (1965), Maare of La Mesa, *New Mexico Geological Society, Sixteenth Field Conference*, 204-209.
- Dobrin, M. B. (1977), Seismic exploration for stratigraphic traps, *Lacustrine Basin Exploration*, 26, 329-351.
- Dufek, J., J. Wexler, and M. Manga (2009), Transport capacity of pyroclastic density currents: Experiments and models of substrate-flow interaction, *J Geophys Res-Sol Ea*, 114.
- Edgar, L. A., J. P. Grotzinger, A. G. Hayes, D. M. Rubin, S. W. Squyres, J. F. Bell III, and K. E. Herkenhoff (2012), Stratigraphic Architecture of Bedrock Reference Section, Victoria Crater, Meridiani Planum, Mars, *Sedimentary Geology of Mars, SEPM Special Publication*, 102, 195-209.
- Edwards, M. B. (1979), Late Precambrian Glacial Loessites from North Norway and Svalbard, *J Sediment Petrol*, 49(1), 84-91.

- Farmer, J. D., and D. J. Des Marais (1999), Exploring for a record of ancient Martian life, *J Geophys Res*, 104(E11), 26977-26995.
- Farrand, W. H., et al. (2007), Visible and near-infrared multispectral analysis of rocks at Meridiani Planum, Mars, by the Mars Exploration Rover Opportunity, *J Geophys Res-Planet*, 112(E6).
- Fassett, C. I., and J. W. Head (2007), Layered mantling deposits in northeast Arabia Terra, Mars: Noachian-Hesperian sedimentation, erosion, and terrain inversion, *J Geophys Res-Planet*, 112(E8).
- Fishbaugh, K. E., and C. S. Hvidberg (2006), Martian north polar layered deposits stratigraphy: Implications for accumulation rates and flow, *J Geophys Res-Planet*, 111(E6).
- Fishbaugh, K. E., et al. (2008), Introduction to the 4th Mars Polar Science and Exploration Conference special issue: Five top questions in Mars polar science, *Icarus*, 196(2), 305-317.
- Fisher, R. V., and A. C. Waters (1970), Base Surge Bed Forms in Maar Volcanoes, *Am J Sci*, 268(2), 157-&.
- Fortezzo, C., and K. Tanaka (2010), Mapping Planum Boreum Unconformities Using Context Camera Mosaics, paper presented at Lunar and Planetary Science XLI, Abstract #2554.
- Fralick, P., J. P. Grotzinger, and L. A. Edgar (2012), Potential Recognition of Accretionary Lapilli in Distal Impact Deposits on Mars: A Facies Analog Provided By the 1.85 Ga Sudbury Impact Deposit, *Sedimentary Geology of Mars, SEPM Special Publication*, 102, 211-227.

- Fryberger, S. G. (1993), A review of aeolian bounding surfaces, with examples from the Permian Minnelusa Formation, USA, *Geological Society Special Publications*, 73, 167-197.
- Fryberger, S. G., and C. J. Schenk (1988), Pin Stripe Lamination - a Distinctive Feature of Modern and Ancient Eolian Sediments, *Sediment Geol*, 55(1-2), 1-15.
- Gawthorpe, R. L., A. J. Fraser, and R. E. L. Collier (1994), Sequence Stratigraphy in Active Extensional Basins - Implications for the Interpretation of Ancient Basin-Fills, *Mar Petrol Geol*, 11(6), 642-658.
- Gellert, R., and R. Rieder (2006), MER APXS Oxide Abundance Archive, NASA Planetary Data System, MER1/MER2-M-APXS-5-OXIDE-SCI-V1.0, edited, MER APXS Oxide Abundance Archive, NASA Planetary Data System, MER1/MER2-M-APXS-5-OXIDE-SCI-V1.0.
- Gellert, R., et al. (2006), Alpha particle X-ray spectrometer (APXS): Results from Gusev crater and calibration report, *J Geophys Res-Planet*, 111(E2).
- Gencalioglu-Kuscu, G., C. Atilla, R. A. F. Cas, and I. Kuscu (2007), Base surge deposits, eruption history, and depositional processes of a wet phreatomagmatic volcano in Central Anatolia (Cora Maar), *J Volcanol Geoth Res*, 159(1-3), 198-209.
- Gile, L. H. (1987), A Pedogenic Chronology for Kilbourne Hole, Southern New-Mexico .2. Time of the Explosions and Soil Events before the Explosions, *Soil Sci Soc Am J*, 51(3), 752-760.
- Giordano, G., and F. Dobran (1994), Computer-Simulations of the Tuscolano-Artemisios 2nd Pyroclastic Flow Unit (Alban Hills, Latium, Italy), *J Volcanol Geoth Res*, 61(1-2), 69-94.

- Glotch, T. D., and P. R. Christensen (2005), Geologic and mineralogic mapping of Aram Chaos: Evidence for a water-rich history, *J Geophys Res-Planet*, 110(E9).
- Gorevan, S. P., et al. (2003), Rock Abrasion Tool: Mars exploration Rover mission, *J Geophys Res-Planet*, 108(E12).
- Grant, J. A., S. A. Wilson, B. A. Cohen, M. P. Golombek, P. E. Geissler, R. J. Sullivan, R. L. Kirk, and T. J. Parker (2008), Degradation of Victoria crater, Mars, *J Geophys Res-Planet*, 113(E11).
- Greeley, R., and J. Guest (1987), Geologic map of the eastern equatorial region of Mars, *Series Map I-1802-B*, United States Geological Survey Miscellaneous Investigations.
- Griffes, J., J. Grotzinger, and R. Milliken (2010), Working Towards a Classification Scheme for Sedimentary Rocks on Mars, paper presented at Lunar and Planetary Science XLI, Abstract #2737.
- Grotzinger, J. P., et al. (2005), Stratigraphy and sedimentology of a dry to wet eolian depositional system, Burns formation, Meridiani Planum, Mars, *Earth and Planetary Science Letters*, 240(1), 11-72.
- Grotzinger, J. P., et al. (2006), Sedimentary textures formed by aqueous processes, Erebus crater, Meridiani Planum, Mars, *Geology*, 34(12), 1085-1088.
- Grotzinger, J. P., and R. Milliken (2012), The Sedimentary Rock Record of Mars: Distribution, Origins, and Global Stratigraphy, *Sedimentary Geology of Mars, SEPM Special Publication*, 102, 1-48.

- Guy, H. P., D. B. Simons, and E. V. Richardson (1966), Sediment transport in alluvial channels: summary of alluvial channel data from flume experiments, 1951-61, *US Geological Survey Professional Paper*.
- Haberle, R. M. (1986), Interannual variability of global dust storms on Mars, *Science*, 234(4775), 459-461.
- Havholm, K. G., and G. Kocurek (1988), A Preliminary-Study of the Dynamics of a Modern Draa, Algodones, Southeastern California, USA, *Sedimentology*, 35(4), 649-669.
- Hawley, J. W. (1984), Hydrogeologic cross sections of the Mesilla bolson area, *Dona Ana county, New Mexico and El Paso County, Texas: New Mexico Bureau of Mines and Mineral Resources Open-File Report*, 190(10).
- Hawley, J. W., and F. E. Kottlowski (1969), Quaternary geology of the south-central New Mexico border region, *New Mexico State Bureau of Mines and Mineral Resources Circular*, 104, 89-115.
- Hawley, J. W., and R. P. Lozinski (1992), Hydrogeologic Framework of the Mesilla Basin in New Mexico and West Texas, *New Mexico Bureau of Mines and Mineral Resources Report*, 323, 47.
- Hayes, A. G., J. P. Grotzinger, L. A. Edgar, S. W. Squyres, W. A. Watters, and J. Sohl-Dickstein (2011), Reconstruction of eolian bed forms and paleocurrents from cross-bedded strata at Victoria Crater, Meridiani Planum, Mars, *J Geophys Res-Planet*, 116.

- Head, J. W., and M. A. Kreslavsky (2004), Medusae Fossae Formation: Ice-rich airborne dust deposited during periods of high obliquity?, in *Lunar and Planetary Science XXXV*, abstract #1635.
- Head, J. W., et al. (2005), Tropical to mid-latitude snow and ice accumulation, flow and glaciation on Mars, *Nature*, 434(7031), 346-351.
- Herkenhoff, K. E., et al. (2003), Athena Microscopic Imager investigation, *J Geophys Res-Planet*, 108(E12).
- Hesp, P. A., and K. Hastings (1998), Width, height and slope relationships and aerodynamic maintenance of barchans, *Geomorphology*, 22(2), 193-204.
- Hoffer, J. M. (1976), Geology of Potrillo basalt field, south-central New Mexico, *Circular 149*, 30.
- Hoffer, J. M., and R. L. Hoffer (1998), Geological Excursions of the El Paso Area: Volume II: Kilbourne-Hunts Holes and Vicinity, New Mexico, El Paso Geological Society, edited.
- Holt, J. W., et al. (2008), Radar Sounding Evidence for Buried Glaciers in the Southern Mid-Latitudes of Mars, *Science*, 322(5905), 1235-1238.
- Howard, A. D. (1978), Origin of Stepped Topography of Martian Poles, *Icarus*, 34(3), 581-599.
- Howard, A. D. (2000), The role of eolian processes in forming surface features of the Martian polar layered deposits, *Icarus*, 144(2), 267-288.
- Howard, A. D., J. A. Cutts, and K. R. Blasius (1982), Stratigraphic Relationships within Martian Polar-Cap Deposits, *Icarus*, 50(2-3), 161-215.

- Hunter, R. E. (1977), Basic Types of Stratification in Small Eolian Dunes, *Sedimentology*, 24(3), 361-387.
- Jaumann, R., et al. (2007), The high-resolution stereo camera (HRSC) experiment on Mars Express: Instrument aspects and experiment conduct from interplanetary cruise through the nominal mission, *Planet Space Sci*, 55(7-8), 928-952.
- Jenkyns, H. C. (1974), Origin of red nodular limestones (Ammonitico Rosso, Knollenkalke) in the Mediterranean Jurassic: a diagenetic model, *Pelagic Sediments: on Land and under the Sea. International Association of Sedimentologists, Special Publications, 1*, 249-271.
- Johnson, S. Y. (1989), Significance of Loessite in the Maroon Formation (Middle Pennsylvanian to Lower Permian), Eagle Basin, Northwest Colorado, *J Sediment Petrol*, 59(5), 782-791.
- Kaasalainen, S., et al. (2009), Radiometric Calibration of LIDAR Intensity With Commercially Available Reference Targets, *IEEE T Geosci Remote*, 47(2), 588-598.
- Kaasalainen, S., A. Jaakkola, M. Kaasalainen, A. Krooks, and A. Kukko (2011), Analysis of Incidence Angle and Distance Effects on Terrestrial Laser Scanner Intensity: Search for Correction Methods, *Remote Sensing*, 3(10), 2207-2221.
- Kargel, J. S., and R. G. Strom (1992), Ancient Glaciation on Mars, *Geology*, 20(1), 3-7.
- Kennedy, W. J., and R. E. Garrison (1975), Morphology and Genesis of Nodular Chalks and Hard-Grounds in Upper Cretaceous of Southern England, *Sedimentology*, 22(3), 311-386.

- Keskes, N., S. Guillon, M. Donias, P. Baylou, and F. Pauget (2004), Method of chronostratigraphic interpretation of a seismic cross section or block, United States.
- Knauth, L. P., D. M. Burt, and K. H. Wohletz (2005), Impact origin of sediments at the opportunity landing site on Mars, *Nature*, 438(7071), 1123-1128.
- Kocurek, G., and R. H. Dott (1981), Distinctions and Uses of Stratification Types in the Interpretation of Eolian Sand, *J Sediment Petrol*, 51(2), 579-595.
- Kostaschuk, R. (2000), A field study of turbulence and sediment dynamics over subaqueous dunes with flow separation, *Sedimentology*, 47(3), 519-531.
- Kreylos, O., G. Bawden, and L. Kellogg (2008), Immersive visualization and analysis of LiDAR data, *Advances in Visual Computing*, 846-855.
- Lajoie, J., G. Lanzafame, P. L. Rossi, and C. A. Tranne (1992), Lateral Facies Variations in Hydromagmatic Pyroclastic Deposits at Linosa, Italy, *J Volcanol Geoth Res*, 54(1-2), 135-143.
- Laskar, J., B. Levrard, and J. F. Mustard (2002), Orbital forcing of the martian polar layered deposits, *Nature*, 419(6905), 375-377.
- Lee, Y. I., and J. C. Kim (1992), Storm-Influenced Siliciclastic and Carbonate Ramp Deposits, the Lower Ordovician Dumugol Formation, South Korea, *Sedimentology*, 39(6), 951-969.
- Leeder, M. R. (2011), *Sedimentology and Sedimentary Basins: From Turbulence to Tectonics*, Wiley-Blackwell.
- Lewis, K. W., O. Aharonson, J. P. Grotzinger, R. L. Kirk, A. S. McEwen, and T. A. Suer (2008), Quasi-periodic bedding in the sedimentary rock record of Mars, *Science*, 322(5907), 1532-1535.

- Lifshitz, I. M., and V. V. Slyozov (1961), The Kinetics of Precipitation from Supersaturated Solid Solutions, *J Phys Chem Solids*, 19(1-2), 35-50.
- Livingstone, I., and A. Warren (1996), *Aeolian Geomorphology: An Introduction*, Addison Wesley Longman Ltd.
- Malin, M. C., et al. (2007), Context Camera Investigation on board the Mars Reconnaissance Orbiter, *J Geophys Res-Planet*, 112(E5).
- Malin, M. C., and K. S. Edgett (2000), Sedimentary rocks of early Mars, *Science*, 290(5498), 1927-1937.
- Malin, M., and K. S. Edgett (2003), Evidence for persistent flow and aqueous sedimentation on early Mars, *Science*, 302, 1931-1934.
- Mangold, N., V. Ansan, P. Masson, and C. Vincendon (2009), Estimate of aeolian dust thickness in Arabia Terra, Mars: Implications of a thick mantle (> 20 m) for hydrogen detection, *Geomorphologie*(1), 23-31.
- Martin, L. J., and R. W. Zurek (1993), An Analysis of the History of Dust Activity on Mars, *J Geophys Res-Planet*, 98(E2), 3221-3246.
- McCollom, T. M., and B. M. Hynek (2005), A volcanic environment for bedrock diagenesis at Meridiani Planum on Mars, *Nature*, 438(7071), 1129-1131.
- McEwen, A. S., et al. (2010), The High Resolution Imaging Science Experiment (HiRISE) during MRO's Primary Science Phase (PSP), *Icarus*, 205(1), 2-37.
- McEwen, A. S., et al. (2007), Mars Reconnaissance Orbiter's High Resolution Imaging Science Experiment (HiRISE), *J Geophys Res-Planet*, 112(E5).

- McKee, E. D. (1966), Structures of dunes at White Sands National Monument, New Mexico (and a comparison with structures of dunes from other selected areas) 1, *Sedimentology*, 7(1), 3-69.
- McKee, E. D., and J. J. Bigarella (1972), Deformational Structures in Brazilian Coastal Dunes, *J Sediment Petrol*, 42(3), 670-681.
- McKim, R. (1996), The dust storms of Mars, *Journal of the British Astronomical Association*, 106, 185-200.
- McLennan, S. M., et al. (2005), Provenance and diagenesis of the evaporite-bearing Burns formation, Meridiani Planum, Mars, *Earth and Planetary Science Letters*, 240, 95-121.
- McLennan, S. M., and J. P. Grotzinger (2008), The Sedimentary Rock Cycle of Mars, in *The Martian Surface-Composition, Mineralogy, and Physical Properties*, edited by J. Bell III, pp. 541-577.
- McMillan, N. J. (2004), Magmatic record of Laramide subduction and the transition to Tertiary extension: Upper Cretaceous through Eocene igneous rocks of New Mexico, in *The Geology of New Mexico: A Geologic History*, edited by G. H. Mack and K. A. Giles, pp. 249-270, New Mexico Geological Society Special Publication 11.
- Metz, J. M., J. P. Grotzinger, D. M. Rubin, K. W. Lewis, S. W. Squyres, and J. F. Bell (2009), Sulfate-Rich Eolian and Wet Interdune Deposits, Erebus Crater, Meridiani Planum, Mars, *J Sediment Res*, 79(5-6), 247-264.

- Milkovich, S. M., and J. W. Head III (2005), North polar cap of Mars: Polar layered deposit characterization and identification of a fundamental climate signal, *J. Geophys. Res.*, 110(E01005), E01005.
- Mitchum, R., P. Vail, and S. Thompson (1977), Seismic stratigraphy and global changes of sea level, part 2: the depositional sequence as a basic unit for stratigraphic analysis, *Lacustrine Basin Exploration*, 26, 53-62.
- Mittlefehldt, D., C. Schröder, R. Gellert, G. Klingelhöfer, B. Jolliff, and R. Morris (2008), Chemostratigraphy and Fe Mineralogy of the Victoria Crater Duck Bay Section: Opportunity APXS and Mössbauer Results, paper presented at Lunar and Planetary Science XXXVIII, Abstract #2404.
- Mohamad, A. H., and E. V. Tucker (1976), Diagenetic History of the Aymestry Limestone Beds (High Gorstian Stage), Ludlow Series, Welsh Borderland, U.K., in *Compaction of Coarse-Grained Sediments*, edited by G. V. Chilingarian and K. H. Wolf, pp. 317-385, Elsevier.
- Moller, N. K., and K. Kvingan (1988), The Genesis of Nodular Limestones in the Ordovician and Silurian of the Oslo Region (Norway), *Sedimentology*, 35(3), 405-420.
- Monsen, E., H. G. Borgos, P. Le Guern, and L. Sonneland (2007), Geological Process Controlled Interpretation Based On 3D Wheeler Diagram Generation, paper presented at Society of Exploration Geophysicists Annual Meeting, San Antonio.
- Morton, R. A., and W. E. Galloway (1991), Depositional, Tectonic and Eustatic Controls on Hydrocarbon Distribution in Divergent Margin Basins - Cenozoic Gulf of Mexico Case-History, *Mar Geol.*, 102(1-4), 239-263.

- Mountney, N., J. Howell, S. Flint, and D. Jerram (1999), Relating eolian bounding-surface geometries to the bed forms that generated them: Etjo Formation, Cretaceous, Namibia, *Geology*, 27(2), 159-162.
- Murray, R. C. (1964), Origin and Diagenesis of Gypsum and Anhydrite, *J Sediment Petrol*, 34(3), 512-523.
- Noble, J. P. A., and K. D. M. Howells (1974), Early Marine Lithification of Nodular Limestones in Silurian of New-Brunswick, *Sedimentology*, 21(4), 597-609.
- Padovani, E., and M. Reid (1989), Field guide to Kilbourne Hole maar, Doña Ana County, New Mexico, *Field Excursions to Volcanic Terranes in the Western United States*, 1, 174-179.
- Paola, C., and L. Borgman (1991), Reconstructing Random Topography from Preserved Stratification, *Sedimentology*, 38(4), 553-565.
- Parker, G., M. Garcia, Y. Fukushima, and W. Yu (1987), Experiments on turbidity currents over an erodible bed, *Journal of Hydraulic Research*, 25(1), 123-147.
- Perron, J. T., and P. Huybers (2009), Is there an orbital signal in the polar layered deposits on Mars?, *Geology*, 37(2), 155-158.
- Picardi, G., et al. (2005), Radar soundings of the subsurface of Mars, *Science*, 310(5756), 1925-1928.
- Plaut, J. J., et al. (2007), Subsurface radar sounding of the south polar layered deposits of Mars, *Science*, 316(5821), 92-95.
- Potter, P. E., J. B. Maynard, and W. A. Pryor (1980), *Sedimentology of Shale: Study Guide and Reference Source*, Springer-Verlag Berlin.

- Qayyum, F., P. De Groot, and N. Hemstra (2012), Using 3D Wheeler diagrams in seismic interpretation – the HorizonCube method, *First Break*, 30, 103-109.
- Reeves, C. C., and R. A. Dehon (1965), Geology of Potrillo Maar New Mexico and Northern Chihuahua Mexico, *Am J Sci*, 263(5), 401-409.
- Reiche, P. (1940), The origin of Kilbourne Hole, New Mexico., *Am J Sci*, 238(3), 212-225.
- Reiss, D., E. Hauber, K. Gwinner, F. Scholten, R. Jaumann, G. di Achille, L. Marinangeli, G. Ori, and G. Neukum (2006), Geologic evolution of the Galle crater, Mars, paper presented at European Planetary Science Congress, Berlin, Germany.
- Rice, M. S., J. F. Bell, E. A. Cloutis, A. Wang, S. W. Ruff, M. A. Craig, D. T. Bailey, J. R. Johnson, P. A. de Souza, and W. H. Farrand (2010), Silica-rich deposits and hydrated minerals at Gusev Crater, Mars: Vis-NIR spectral characterization and regional mapping, *Icarus*, 205(2), 375-395.
- Richardson, M. I., and R. J. Wilson (2002), Investigation of the nature and stability of the Martian seasonal water cycle with a general circulation model, *J Geophys Res-Planet*, 107(E5).
- Rubin, D. M. (1987), *Cross-Bedding, Bedforms, and Paleocurrents*, 187 pp., SEPM, Tulsa, OK.
- Rubin, D. M., and C. Carter (2005), Bedforms 4.0: MATLAB Code for Simulating Bedforms and Cross-Bedding, *US Geological Survey Open-File Report*, 1272, 13.
- Rubin, D. M., and R. E. Hunter (1982), Bedform Climbing in Theory and Nature, *Sedimentology*, 29(1), 121-138.

- Rubin, D. M., and R. E. Hunter (1983), Reconstructing Bedform Assemblages from Compound Crossbedding, in *Developments in Sedimentology*, edited by M. E. Brookfield and T. S. Ahlbrandt, pp. 407-427, Elsevier.
- Sadler, P. M. (1981), Sediment Accumulation Rates and the Completeness of Stratigraphic Sections, *J Geol*, 89(5), 569-584.
- Scheu, B., U. Kueppers, S. Mueller, O. Spieler, and D. B. Dingwell (2008), Experimental volcanology on eruptive products of Unzen volcano, *J Volcanol Geoth Res*, 175(1-2), 110-119.
- Schmincke, H., R. V. Fisher, and A. C. Waters (1973), Antidune and Chute and Pool Structures in Base Surge Deposits of Laacher-See Area, Germany, *Sedimentology*, 20(4), 553-574.
- Schultz, P. H., and A. B. Lutz (1988), Polar Wandering of Mars, *Icarus*, 73(1), 91-141.
- Scott, D. H., and K. L. Tanaka (1986), Geologic map of the western equatorial region of Mars, *Miscellaneous Investigations Series Map I-1802-A*, US Geological Survey.
- Seager, W. (1987), Caldera-like collapse at Kilbourne Hole maar, New Mexico, *New Mexico Geology Science and Service*, 9(4), 69-73.
- Seager, W. R., M. Shafiqullah, J. W. Hawley, and R. F. Marvin (1984), New K-Ar Dates from Basalts and the Evolution of the Southern Rio-Grande Rift, *Geol Soc Am Bull*, 95(1), 87-99.
- Sharp, R. P. (1973), Mars - Fretted and Chaotic Terrains, *J Geophys Res*, 78(20), 4073-4083.

- Sheridan, M. F., and R. G. Updike (1975), Sugarloaf Mountain Tephra - Pleistocene Rhyolitic Deposit of Base-Surge Origin in Northern Arizona, *Geol Soc Am Bull*, 86(4), 571-581.
- Skorov, Y. V., W. J. Markiewicz, A. T. Basilevsky, and H. U. Keller (2001), Stability of water ice under a porous nonvolatile layer: implications to the south polar layered deposits of Mars, *Planet Space Sci*, 49(1), 59-63.
- Smalley, I. J., and D. H. Krinsley (1979), Eolian Sedimentation on Earth and Mars - Some Comparisons, *Icarus*, 40(2), 276-288.
- Smalley, I. J., and J. A. Leach (1978), Origin and Distribution of Loess in Danube Basin and Associated Regions of East-Central Europe - Review, *Sediment Geol*, 21(1), 1-26.
- Smith, D. E., et al. (2001), Mars Orbiter Laser Altimeter: Experiment summary after the first year of global mapping of Mars, *J Geophys Res-Planet*, 106(E10), 23689-23722.
- Smith, G. A., and D. Katzman (1991), Discrimination of Eolian and Pyroclastic-Surge Processes in the Generation of Cross-Bedded Tuffs, Jemez Mountains Volcanic Field, New Mexico, *Geology*, 19(5), 465-468.
- Smith, I. B., and J. W. Holt (2010), Onset and migration of spiral troughs on Mars revealed by orbital radar, *Nature*, 465(7297), 450-453.
- Smith, I. B., and J. W. Holt (2012), The Northern Spiral Troughs of Mars as Cyclic Steps: a Framework for Using Observations of Active Processes to Calculate Migration and Accumulation Rates on the NPLD, paper presented at Third International Planetary Dunes Workshop, Abstract #7047, Flagstaff.

- Smith, D. E., et al. (2001), Mars Orbiter Laser Altimeter: Experiment summary after the first year of global mapping of Mars, *J Geophys Res-Planet*, 106(E10), 23689-23722.
- Soderblom, L., et al. 1973. Mariner-9 Observations of Surface of Mars in North Polar Region. *Journal of Geophysical Research*. 78, 4197-4210.
- Sohn, Y. K., and S. K. Chough (1989), Depositional Processes of the Suwolbong Tuff Ring, Cheju Island (Korea), *Sedimentology*, 36(5), 837-855.
- Soreghan, G. S., R. D. Elmore, and M. T. Lewchuk (2002), Sedimentologic-magnetic record of western Pangean climate in upper Paleozoic loessite (lower Cutler beds, Utah), *Geol Soc Am Bull*, 114(8), 1019-1035.
- Southard, J. B., and L. A. Boguchwal (1990), Bed Configurations in Steady Unidirectional Water Flows .2. Synthesis of Flume Data, *J Sediment Petrol*, 60(5), 658-679.
- Sparks, R. S. J. (1976), Grain-Size Variations in Ignimbrites and Implications for Transport of Pyroclastic Flows, *Sedimentology*, 23(2), 147-188.
- Squyres, S. W. (1979), Evolution of Dust Deposits in the Martian North Polar Region, *Icarus*, 40(2), 244-261.
- Squyres, S. W., et al. (2006a), Bedrock formation at Meridiani Planum, *Nature*, 443(7107), E1-E2.
- Squyres, S. W., et al. (2007), Pyroclastic activity at home plate in Gusev Crater, Mars, *Science*, 316(5825), 738-742.
- Squyres, S. W., et al. (2003), Athena Mars rover science investigation, *Journal of Geophysical Research: Planets*, 108(E12), 2156-2202.

- Squyres, S. W., et al. (2004a), The Opportunity Rover's Athena science investigation at Meridiani Planum, Mars, *Science*, 306(5702), 1698-1703.
- Squyres, S. W., et al. (2006b), Overview of the Opportunity Mars Exploration Rover mission to Meridiani Planum: Eagle crater to Purgatory ripple, *J Geophys Res-Planet*, 111(E12).
- Squyres, S. W., et al. (2004b), In situ evidence for an ancient aqueous environment at Meridiani Planum, Mars, *Science*, 306(5702), 1709-1714.
- Squyres, S. W., et al. (2009), Exploration of Victoria crater by the Mars rover Opportunity, *Science*, 324(5930), 1058-1061.
- Squyres, S. W., et al. (2006), Two Years at Meridiani Planum: Results from the Opportunity Rover, *Science*, 313(5792), 1403-1407.
- Stack, K. M., J. L. Griffes, and J. P. Grotzinger (in prep), The global distribution of layered deposits on Mars from HiRISE imagery.
- Stuart, C., and M. Brener (1979), Low-regime: base surge dunes—an example from Kilbourne and Hunt's Holes, south-central New Mexico, paper presented at Geological Society of America annual meeting, San Diego, CA.
- Summons, R. E., J. P. Amend, D. Bish, R. Buick, G. D. Cody, D. J. Des Marais, G. Dromart, J. L. Eigenbrode, A. H. Knoll, and D. Y. Sumner (2011), Preservation of martian organic and environmental records: final report of the Mars biosignature working group, *Astrobiology*, 11(2), 157-181.
- Tanaka, K. L. (2005), Geology and insolation-driven climatic history of Amazonian north polar materials on Mars, *Nature*, 437(7061), 991-994.

- Thomas, P., S. Squyres, K. Herkenhoff, A. Howard, and B. Murray (1992), Polar deposits of Mars, in *Mars*, edited by H. H. Kieffer, pp. 767-795, University of Arizona Press.
- Thomson, B. J., N. T. Bridges, R. Milliken, A. Baldrige, S. J. Hook, J. K. Crowley, G. M. Marion, C. R. de Souza, A. J. Brown, and C. M. Weitz (2011), Constraints on the origin and evolution of the layered mound in Gale Crater, Mars using Mars Reconnaissance Orbiter data, *Icarus*, 214(2), 413-432.
- Tilling, R. (1985), Volcanoes. USGS General Interest Publication, edited, United States Geological Survey.
- Vail, P., R. Mitchum, and S. Thompson (1977), Seismic stratigraphy and global changes of sea level, part 3: relative changes of sea level from coastal onlap, *Seismic Stratigraphy—Applications to Hydrocarbon Exploration: American Association of Petroleum Geologists, Memoir*, 26, 63-81.
- Valentine, G. A., R.V. Fisher (2000), Pyroclastic Surges and Blasts, in *Encyclopedia of Volcanoes*, edited by H. Sigurdsson and B. Houghton, San Diego.
- Walker, G. P. L. (1971), Grain-Size Characteristics of Pyroclastic Deposits, *J Geol*, 79(6), 696-714.
- Walker, G. P. L. (1984), Characteristics of Dune-Bedded Pyroclastic Surge Bedsets, *J Volcanol Geoth Res*, 20(3-4), 281-296.
- Waters, A. C., and R. V. Fisher (1971), Base Surges and Their Deposits - Capelinhos and Taal Volcanoes, *J Geophys Res*, 76(23), 5596-5614.
- Watters, W., J. Bell, F. Calef, M. Golombek, J. Grant, A. Hayes, R. Li, T. Parker, R. Sullivan, and S. Squyres (2011), Structure and Morphology of Santa Maria Crater,

- Meridiani Planum, Mars, paper presented at Lunar and Planetary Science XLII, abstract #2586.
- Wheeler, H. E. (1958), Time-stratigraphy, *AAPG Bulletin*, 42(5), 1045-1063.
- Williams, G. P. (1967), *Flume Experiments on the Transport of a Coarse Sand*, US Government Printing Office.
- Wilson, I. G. (1971), Desert Sandflow Basins and a Model for Development of Ergs, *Geogr J*, 137(JUN), 180-199.
- Wohletz, K. H., and M. F. Sheridan (1979), A model of pyroclastic surge, *Geological Society of America Special Paper 180*, 177-194.
- Wohletz, K. H., and M. F. Sheridan (1983), Hydrovolcanic Explosions .2. Evolution of Basaltic Tuff Rings and Tuff Cones, *Am J Sci*, 283(5), 385-413.
- Wolf, K. H., and G. V. Chilingarian (1976), Compactional diagenesis of carbonate sediments and rocks, in *Compaction of coarse-grained sediments*, edited by G. V. Chilingarian and K. H. Wolf, pp. 719-768, Elsevier.
- Yen, A. S., et al. (2005), An Integrated View of the Chemistry and Mineralogy of Martian Soils, *Nature*, 436, doi:10.1038/nature03637.